

Molecular dynamics modelling of the mechanics of cells

Citation for published version (APA):

Madhikar, P. (2019). *Molecular dynamics modelling of the mechanics of cells*. [Phd Thesis 1 (Research TU/e / Graduation TU/e), Mathematics and Computer Science]. Technische Universiteit Eindhoven.

Document status and date:

Published: 28/05/2019

Document Version:

Publisher's PDF, also known as Version of Record (includes final page, issue and volume numbers)

Please check the document version of this publication:

- A submitted manuscript is the version of the article upon submission and before peer-review. There can be important differences between the submitted version and the official published version of record. People interested in the research are advised to contact the author for the final version of the publication, or visit the DOI to the publisher's website.
- The final author version and the galley proof are versions of the publication after peer review.
- The final published version features the final layout of the paper including the volume, issue and page numbers.

[Link to publication](#)

General rights

Copyright and moral rights for the publications made accessible in the public portal are retained by the authors and/or other copyright owners and it is a condition of accessing publications that users recognise and abide by the legal requirements associated with these rights.

- Users may download and print one copy of any publication from the public portal for the purpose of private study or research.
- You may not further distribute the material or use it for any profit-making activity or commercial gain
- You may freely distribute the URL identifying the publication in the public portal.

If the publication is distributed under the terms of Article 25fa of the Dutch Copyright Act, indicated by the "Taverne" license above, please follow below link for the End User Agreement:

www.tue.nl/taverne

Take down policy

If you believe that this document breaches copyright please contact us at:

openaccess@tue.nl

providing details and we will investigate your claim.

Molecular Dynamics Modelling of the Mechanics of Cells

Pranav Madhikar

Molecular Dynamics Modelling of the Mechanics of Cells

Pranav Madhikar

Copyright © 2019 by Pranav Madhikar. All Rights Reserved.

CIP-DATA LIBRARY TECHNISCHE UNIVERSITEIT EINDHOVEN

Madhikar, P.

Molecular Dynamics Modelling of the Mechanics of Cells by
Pranav Madhikar.

Eindhoven: Technische Universiteit Eindhoven, 2019. Proefschrift.

Cover design by Pranav Madhikar. Tiling based on the buckyball (also known as truncated icosahedron) graph, a 2D embedding of the C₆₀ fullerene which is a relative of the C₁₈₀ fullerene used in this thesis. Created with the help of the SageMath package. Inspired by M.C. Escher.

A catalogue record is available from the Eindhoven University of Technology Library

ISBN: 978-90-386-4772-2

Keywords: CUDA, GPU, Cell Growth, MD

Printed by Gildeprint.

Molecular Dynamics Modelling of the Mechanics of Cells

PROEFSCHRIFT

ter verkrijging van de graad van doctor aan de Technische Universiteit Eindhoven, op gezag van de rector magnificus prof.dr.ir. F.P.T. Baaijens, voor een commissie aangewezen door het College voor Promoties, in het openbaar te verdedigen op 28 mei 2019 om 16:00 uur.

door

Pranav Madhikar

geboren te Hyderabad, Indië

Dit proefschrift is goedgekeurd door de promotoren en de samenstelling van de promotiecommissie is als volgt:

voorzitter: prof.dr. J.J. Lukkien
1e promotor: prof.dr. M.E.J. Karttunen
co-promotor: dr.Dipl.-Phys. B. Baumeier
externe leden: dr. G. Lattanzi (Università di Trento)
prof.dr. S.-J. Marrink (Rijksuniversiteit Groningen)
prof.dr. J. Westerholm (Åbo Akademi)
lid TU/e: prof.dr. J.M.J den Toonder

Het onderzoek of ontwerp dat in dit proefschrift wordt beschreven is uitgevoerd in overeenstemming met de TU/e Gedragscode Wetenschapsbeoefening.

*Dedicated to my parents,
Dr. Prabhakar Madhikar and Mrs. Rukmini Madhikar;
for their eternal love and encouragement.*

Contents

List of Figures	xi
List of Tables	xv
1 Introduction	1
2 A Brief Overview of Molecular Dynamics	7
2.1 Methodology	8
2.1.1 Calculating MD Trajectories	14
2.1.2 Simulations at Constant Temperature and/or Pressure	15
2.2 Coarse-Grained Molecular Dynamics	16
2.2.1 Solvent Free Models	18
2.2.2 Dissipative Particle Dynamics	20
3 The Cell From a Mechanical Perspective	23
3.1 A Short Introduction to Cell Structure	24
3.2 The Mechanical Cell	26
3.2.1 The Cell Boundary	28
3.2.2 The Cell Interior	30
3.2.3 The Cell Exterior	31
3.3 Cell Growth and Division	32
3.3.1 The role of division plane alignment	35
3.4 Current Models For Simulating Cell Behaviour	38
3.5 Mathematical Models	40

3.5.1	Models of Cell Population Dynamics	40
3.5.2	Continuum Models of Cell Behaviour	42
3.6	Discrete Cell Models	43
3.6.1	The Cellular Potts Model	43
3.6.2	Topological Models	46
3.6.3	Vertex Models	46
3.6.4	Triangulation or Tessellation Based Models	48
3.6.5	The Cellular Discrete Element Model (CeDEM)	49
4	Morphology of Proliferating Cellular Matter in 1D and 2D with CeDEM	53
4.1	Model and methods	56
4.2	Results	58
4.2.1	Quasi-one-dimensional morphology	58
4.2.2	Soft and stiff cells in 2D	60
4.3	Conclusions	66
5	The <i>CellSim3D</i> Model and Simulator	69
5.1	<i>CellSim3D</i> Assumptions	72
5.2	The Force Field and Cell Structure	75
5.2.1	Cell Shape and Topology	75
5.2.2	The Force Field	77
5.2.3	The Integrator	86
5.3	Simulating Cell Division	87
5.3.1	Epithelia in <i>CellSim3D</i>	90
5.4	Simulation Units	92
5.5	The <i>CellSim3D</i> Software Package	95
5.5.1	Implementation	98
5.5.2	Minimum System Requirements:	98
5.5.3	The Simulation Loop	99
5.5.4	Program Summary:	99
5.5.5	Source files	103
5.6	Measuring the Performance of the <i>CellSim3D</i> Simulator	105
5.7	Conclusions	107

6 The Dynamics of Growth and The Cellular Mechanical Environment	109
6.1 Introduction	109
6.2 How is Tissue Growth Studied?	110
6.2.1 Population Trends	112
6.2.2 Mitotic Index	117
6.2.3 System size	120
6.3 Why does growth rate slow down in a purely mechanical system?	121
6.3.1 Density	123
6.3.2 Number of Nearest Neighbours	125
6.4 Effects of Friction on Tissue Growth and Structure	133
6.5 Conclusions	136
7 Summary and Outlook	139
References	149
Appendices	187
A Example Input file to <i>CellSim3D</i>	189
Summary	193
Acknowledgements	197
Curriculum Vitae	201

List of Figures

1.1	Simplified cell migration	3
2.1	Bonded degrees of freedom	11
2.2	Periodic boundary conditions	13
2.3	Example coarse-graining map for a lipid	17
2.4	Top-down and bottom-coarse graining	19
3.1	A prokaryotic cell	25
3.2	A eukaryotic cell	26
3.3	The mechanical cell	27
3.4	Actomyosin network	29
3.5	The cell cycle	33
3.6	Mitosis and cytokinesis	36
3.7	Cross-section of symmetric, and asymmetric cell division.	38
3.8	Results of random and consistent division.	39
3.9	The Cellular Potts Model	44
3.10	The difference between a real epithelium and a topological approximation of it	47
3.11	Cell division in topological and vertex models.	48
3.12	The two dimensional Cellular Discrete Element Model (CeDEM)	51
4.1	Images of real cyanobacteria	55
4.2	Cyanobacteria simulated by CeDEM	59

4.3	The distribution of forces in an epithelium of a mixed system of soft and stiff cells	61
4.4	Qualitative difference in growth at different intermembrane friction coefficients	62
4.5	Distribution of size and force in mixed epithelia	63
4.6	Tumour like tissue configuration, and spatial distributions of cell size and force	64
4.7	Distribution of forces in tumour like tissues at low and high intermembrane friction	66
5.1	The structure of <i>CellSim3D</i> cells.	77
5.2	<i>CellSim3D</i> force field summary	78
5.3	Intracellular forces	79
5.4	The direction of the growth force.	82
5.5	Tetrahedral subdivisions to calculate cell volume.	83
5.6	The Intercellular forces	84
5.7	Intercellular potential	85
5.8	Cell division in <i>CellSim3D</i>	88
5.9	Cell division algorithm	89
5.10	The <i>CellSim3D</i> growth loop	91
5.11	Epithelia in <i>CellSim3D</i>	92
5.12	Determining the average cell division time	94
5.13	<i>CellSim3D</i> flowchart	102
5.14	<i>CellSim3D</i> scaling in time	106
5.15	Measuring the time needed to reach some minimum number of cells	107
6.1	Visualization of <i>CellSim3D</i> simulation runs	111
6.2	Theoretical and experimental growth trends	113
6.3	<i>CellSim3D</i> population trends compared to theory and experiment	116
6.4	Experimental and computational measurements of mitotic index	119
6.5	<i>CellSim3D</i> radius of gyration trends compared to experimental and other computational results	122
6.6	How density changes with growth and simulation time	124
6.7	Older tissues grow mostly at their boundaries	126

6.8 Number of nearest neighbours in epithelia	128
6.9 Number of nearest neighbours in 3D spheroids	130
6.10 Nearest neighbours compared to growth and density	132
6.11 The effect of friction on growth trends	134
6.12 The effect friction on mitotic index	135
6.13 Nearest neighbour distributions over increasing friction co-efficients	136
7.1 An approximation of cell polarity	143

List of Tables

4.1	Two dimensional simulation parameters	58
5.1	The Integrator Used in <i>CellSim3D</i>	87
5.2	Typical values of <i>CellSim3D</i> parameters	96

Chapter 1

Introduction

The cell is the fundamental building block of life as we know it. All living organisms are either single celled, such as bacteria (prokaryotes), or multicellular, like plants and animal cells (eukaryotes). Some may argue that the virus is also a unit of life. Now, a virus is not single cellular, multicellular, or any other kind of cellular, but there is some debate about whether viruses can be considered to be “alive” [1, 2]. We will leave them out of our discussion for the sake of simplicity. All the functions of life as we know it are completely reliant on the ability of cells to live their own lives healthily. This requires that cells be able to: (a) consume energy, (b) reproduce, and (c) regenerate themselves after injury. Since the cells do not exist isolated from everything else, they can react to their environment which may, in turn, affect cell functions. For example, cells may compete for nutrients and that affects their energy consumption and/or reproduction [3, 4], or some illness may change their ability to regenerate [5]. Therefore, it follows, that one should understand how these building blocks, the cells, behave and react to various stimuli to be able to understand life.

Ever since the discovery of cells in the seventeenth century by Robert Hooke and Antoni van Leeuwenhoek [6], scientists have been studying them tirelessly. Most biological functions can be traced to cells of different types carrying out their roles. Different fields of research dedicated to the different parts and functions of the cell have developed over time: cell metabolism, genetics, the study of the different organelles in the cell

and their function, cell communication, and cell growth and reproductive cycle. Systems biologists go a step further and study the connections between these different fields.

In most of these branches of cell biology, the focus is on the *biochemical* parts of cell behaviour. Here researchers have been asking questions such as [7–9]

- What are the chemical reactions involved?
- What are the relationships between the reactions?
- How are all the above related to genetics [10]?
- Can one relate the behaviour of a group of cells to that of a single cell?
- What is the genetic basis of diseases? Of cancer?

Cell biologists have learned a great deal regarding the operation of the internal components of the cell by seeking answers to these questions. The role of mitochondria in energy production and cellular metabolism, how chlorophyll is essential for photosynthesis in plant cells, the conduction of electrical impulses through axons in nerve cells [11, 12] are all examples of knowledge gained through their efforts. The vital behaviour of groups of cells, such as organs, is also a vibrant topic of inquiry [13–15]. Both for scientific curiosity, and to more practical ends such as understanding the mechanisms of disease [16] or decay due to aging [17].

In this thesis, we discuss questions regarding the behaviour of cells as physical objects. After all, cells are objects in the universe: they have mass, they have a friction, they exert forces on their environments. Ample evidence has been found showing cells are also interacting with their environments and each other *mechanically*, not just biochemically [18, 19]. This interplay between mechanical signals and the biology of cells is called *mechanotransduction* [18, 20, 21]. The most intuitive examples of mechanotransduction are in our very own senses. The sense of touch, sound, pressure (baroreception), and the sense of motion (proprioception) all involve certain sensory cells reacting to mechanical stimulus and converting it into biochemical signals. We are able to mechanically excite our surroundings as well with muscle contraction. In muscle contraction

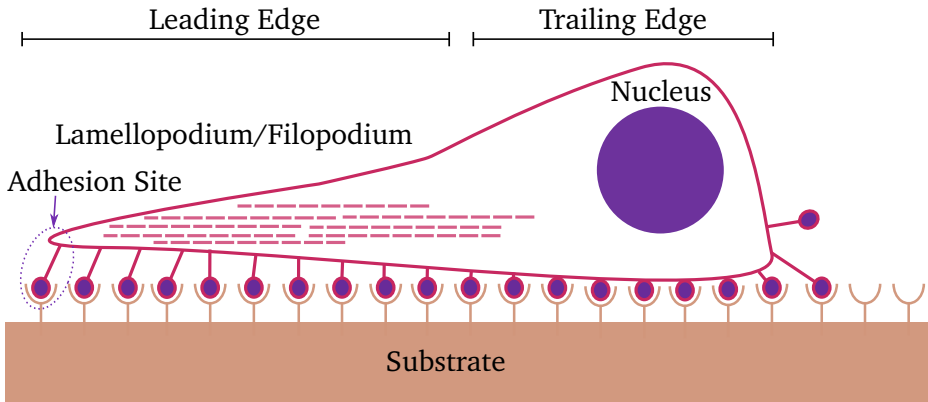


Figure 1.1: A filopodium, which is a bundle of cross-linked fibrous filaments that induces the cell membrane to extend at leading edge and form new binding complexes with the substrate. At the trailing edge, binding with the substrate is reduced. These two effects will cause the cell to move to the left. Since this image shows a cross-section, a lamellopodium is shown in the same manner. The binding sites are the result of interaction between cell adhesion molecules, see Section 3.2.1.

a hormonal and/or electrical signal to the cell triggers a biochemical reaction within muscle cells, which contracts or relaxes them, and in turn results in a mechanical action on the environment.

There are also several less intuitive examples of mechanotransduction including cell migration [22, 23], tissue patterning [24] and responding to mechanical stimulus in general, such as shear stress [25]. To illustrate further, consider amoeboid cell migration as shown in Figure 1.1. Signals within the cell cause release of cell junctions at the trailing edge, the rearrangement of its body towards its target (on the left in the figure), the generation of new cell junctions at the leading edge, and then the contraction of its body. The process involves multiple biochemical signals and subsequent restructuring of the cell's body to create filopodia [26], which are bundles of cross linked fibres that cause the cell membrane to protrude extensively in one direction, and lamellopodia [27] which are larger extensions of the cell along the whole cell. Both filopodia and lamellopodia are depicted as the same structure as Figure 1.1 is a cross-section.

Mechanotransduction plays a profound role in cellular biology. It has been shown that mechanics can affect stem cell differentiation [28–31]

and morphogenesis in general [32–34], the behaviour of cancers [35, 36] and metastasis [37], and a whole host of biological functions such as [21]. Mechanical properties such as texture, stiffness, pressure, shear stress, tension, compression can all play a vital role in every aspect of cell behaviour, and as a consequence, on biology and life.

Many experimental techniques have been devised [21, 38] to study mechanotransduction. The basic goal with those techniques is to correlate the biomechanical response of cells to some chemical or physical stimulus, or vice versa. The many phenomena of mechanotransduction that were listed above have been elucidated with experimental methods. Running these experiments entails tracking the forces acting on the cell membrane, the outer envelope of cells¹, and correlating to some biochemical process. The forces themselves are very small, of the order of 1 to 100 nN [39–41]. However, experiments can only either measure macroscopic properties of tissues, containing millions of cells, or individual cells. It is difficult to link the behaviour of large tissues containing millions of cells to the mechanical properties of individual cells. It is also impossible to control the level of variability, such as e.g. variation in the level of nutrition provided to each cell, in experiments. Theoretical models provide an alternative method to study complex phenomena such as mechanotransduction with greater control on the governing parameters of tissues. In a theoretical model one attempts to mathematically connect fundamental physical facts regarding the cells in question to macroscopic observables pertaining to them. Analytical or numerical solutions to these models combined with experimental results give researchers a more complete understanding of the underlying phenomena. However, it is often impossible to describe the interaction of hundreds of cells mathematically. Therefore, these types of models are forced to either consider a small number of cells, or to approximate the whole tissue as a single object. Computational models allow researchers run *in silico* experiments that connect the fundamental physical parameters of the cells to the macroscopic observables. Additionally, they offer the power to control all the variables involved giving researchers the ability to simulate experimentally inaccessible regimes.

This thesis is centred on one such computational method to study mechanotransduction: *CellSim3D* [42], a 3D top-down coarse-grained

¹Cell membranes are discussed in more detail in Chapter 3

(CG) molecular dynamics (MD) model that aims to be a flexible general purpose method to study cell growth and mechanotransduction in large tissues. MD is a particle based method where the underlying system is approximated by a collection of particles interacting through potentials. Thus, MD allows researchers to track the forces acting on the particles and link them to macroscopic observables by analyzing the trajectories of the particles. Our aim with *CellSim3D* [42] is to give researchers a fast open source cell simulator that can simulate tissue growth with tight control on the mechanical properties of the cells. The simulator source code is available on github: <https://github.com/SoftSimu/CellSim3D>.

Thesis Structure

As was stated above, the *CellSim3D* model is a top-down CG model that is based on MD. For context we give a brief introduction to MD in Chapter 2. Therein we introduce the history of MD, the concept of a force field, and the degrees of freedom in MD which inspire the degrees of freedom in *CellSim3D*. We also explore some CG techniques, out of which we use the Dissipative Particle Dynamics formalism for the *CellSim3D* model.

Next, in Chapter 3 we provide a concise introduction to cell structure from a mechanical perspective. We discuss the notion of the mechanical cell, which we use to drive the development of *CellSim3D* force field. We also discuss some other computational and theoretical models for studying cell behaviour and mechanotransduction.

In Chapter 4, we use one of the models described in Chapter 3 to study the morphologies of cellular materials with the Cellular Discrete Element Model (CeDEM) [43], a model that is similar in spirit to *CellSim3D* but in 2D. The 3D *CellSim3D* model is inspired by the CeDEM.

The details of the *CellSim3D* model and its implementation in software is given in Chapter 5. Therein we discuss details regarding the structure of *CellSim3D* cells, the force field, and details regarding the implementation of the simulator.

In Chapter 6 we use *CellSim3D* to reproduce the growth behaviour of both epithelia² and 3D cellular systems with up to approximately 26 000

²Epithelia are quasi 2D tissues that are ubiquitous in biological systems. The surface of

cells. We then run further simulations to probe the interplay between tissue growth, structure, and intercellular friction.

We summarize the thesis in Chapter 7 and propose some extensions to *CellSim3D*. We describe how it can be extended with terms to simulate the connection between heterogeneity of cell properties and their behaviour, cell migration, and cell differentiation.

human skin is a type of epithelium. See Section 5.3.1 for details

Chapter 2

A Brief Overview of Molecular Dynamics

Molecular dynamics (MD) is a set of algorithms, and tools, that are used for the analysis and study of molecular systems. MD is based on the framework of Newtonian mechanics where each atom is assumed to be a particle that interacts with other atoms (other particles) through a potential that aims to approximate the real interactions between the atoms. The historic roots of MD go back to the late 1950s when it was first used to study phase transitions of hard spheres by Alder and Wainright [44, 45]. It was then shown by Rahman [46] in 1964 that with a careful choice of the potential acting between the particles, the method of Alder and Wainright could be used to study the properties of Argon at 94.4 K. Rahman, along with Stillinger, showed that the method can be extended yet again to study liquid water in 1971 [47]. Water would later prove to be incredibly difficult to study correctly [48, 49], but the fundamental methods described by Rahman and Stillinger still remain applicable. In 1977, McCammon, Gelin, and Karplus demonstrated the first application of MD to study the dynamics of protein folding [50]. At the time the simulations were limited to less than 1000 atoms simulated for a few ps. Thanks to the foundation that the researchers above built, the rapid development of computational power, the increasing variety of high performing software packages [51–55], and the development more efficient algorithms to approximate molecular interactions MD has evolved over the past 50 years to the point where it

is possible to study large systems with 10^5 to 10^6 atoms for hundreds of ns [52, 56–60] or smaller systems with of the order of 10^3 to 10^4 atoms for up to ten μs [59, 61–64]. Even researchers with access to modest computational facilities can simulate 10000 to 100000 atoms for 10 to 100 ns [65]. MD can be applied to a huge variety of systems such as lipids [66–69], proteins [70–74], polymers [75, 76], supramolecular polymers [77, 78], DNA [65, 79, 80], crystals [81–83], and soft matter [76, 84, 85].

As we noted above, the rapid development of computational power has played a huge role in the advancement of MD. However, it would not be possible without the work of the many researchers who implemented and refined the algorithms of MD to make use of the hardware available. Many software packages exist with high performing and flexible MD implementations such as GROMACS [51], LAMMPS [53], NAMD [54], HOOMD-blue [55].

This thesis is about using the algorithms that were developed for MD to study cell behaviour and growth. This is done with the *CellSim3D* [42] (Chapter 5), a 3D Graphics Processor Unit (GPU) accelerated model and software package ¹. The degrees of freedom in *CellSim3D*, and the force field acting upon them, are based on the principles of MD outlined below. This chapter provides a short introduction to the basics of MD theory. Although no MD results are presented in this thesis, this discussion is to provide context for the *CellSim3D* force field (Section 5.2). Readers interested in details about MD are referred to Refs. [65, 86–89]. Details regarding efficient implementations of MD algorithms are available in Refs. [51–55]. A discussion regarding best practices in running MD simulations for soft matter systems is given in Refs. [84], and Refs. [90, 91] discuss how MD can be used to drive experimentation in the life sciences.

2.1 Methodology

The basic principles of MD arise from the definition of a conservative force acting on particle i given by

$$\mathbf{F}_i = -\nabla_{\mathbf{x}_i} U(\mathbf{X}) \quad (2.1)$$

¹Available on github: <https://github.com/SoftSimu/CellSim3D>

where $U(\mathbf{X})$ is a potential that describes the interactions between particle i and the rest of the particles in the system, and $\mathbf{X} \in \mathbb{R}^{3N}$ is a vector describing the configuration of N particles in 3D space. The gradient is taken with respect to the position of particle i . $U(\mathbf{X})$ thus describes the potential energy landscape that the atom i is in. Combining the definition of conservative forces with Newton's second law then produces a second order ordinary differential equation (ODE) given by

$$m_i \ddot{\mathbf{x}}_i = -\nabla_{\mathbf{x}_i} U(\mathbf{X}), \quad (2.2)$$

where m_i is the mass of atom i . The potential energy landscape $U(\mathbf{X})$ contains a classical description of the interactions between the atoms. These arise from the Born-Oppenheimer approximation [92, 93], where we assume that the electronic and nuclear degrees of freedom are separated. Therefore, interactions between atoms can be defined by continuous potentials that only depend on the distance between atoms. Furthermore, the potential is assumed to be purely additive, meaning that the landscape can be described by a sum of terms, each individually describing one type of interaction [72]. Thus, $U(\mathbf{X})$ can be split into two types of interactions

$$U(\mathbf{X}) = U^B(\mathbf{X}) + U^{NB}(\mathbf{X}), \quad (2.3)$$

where U^B approximates bonded interactions, U^{NB} approximates non-bonded interactions. The former describes the interactions between atoms of the same molecule that are bonded to each other via covalent bonds, and the latter describes the interactions between all atoms that are not bonded to each other covalently, but interact through dispersion (van der Waals), repulsion, and/or electrostatic interactions. *Force Fields* describe the precise definition of the potentials, and their parameters for various atoms and molecules. There are multiple published force fields such as CHARMM [94, 95] AMBER [96, 97], GROMOS [98], and OPLS[99, 100].

Bonded potentials are further decomposed into a sum of a potential depending on changes in bond lengths between two atoms, potential depending on the angle between three atoms, and a potential depending on the angle between the two planes defined by four atoms. An example of the decomposition is illustrated as follows. The bonding potential can be

decomposed as

$$U^B(\mathbf{X}) = \sum_{\text{bonds}} U^S(\mathbf{X}) + \sum_{\text{angles}} U^\theta(\mathbf{X}) + \sum_{\text{dihedrals}} U^\varphi(\mathbf{X}) \quad (2.4)$$

in which $U^S(\mathbf{X})$ approximates the interactions occurring between bonded atoms, $U^\theta(\mathbf{X})$ approximates the interactions due to changes in the angle, and $U^\varphi(\mathbf{X})$ the potential due to changes in the dihedral.

Using Figure 2.1 to define the degrees of freedom, one can define the potential of bonded atoms i, j, k, l , to approximate the various bonded terms with

$$U^S(r_{ij}) = \frac{1}{2} k_{ij}^S (r_{ij} - r_{ij}^0)^2 \quad (2.5)$$

$$U^\theta(\theta_{ijk}) = \frac{1}{2} k_{ijk}^\theta (\theta_{ijk} - \theta_{ijk}^0)^2 \quad (2.6)$$

$$U^\varphi(\varphi_{ijkl}^{\text{imp}}) = \frac{1}{2} k_{ijkl}^{\varphi^{\text{imp}}} (\varphi_{ijkl}^{\text{imp}} - \varphi_{ijkl}^{\text{imp},0})^2. \quad (2.7)$$

$$U^\varphi(\varphi_{ijkl}) = k_{ijkl}^\varphi [1 + \cos(n\varphi_{ijkl} - \delta)] \quad (2.8)$$

In the definitions above, k_{ij}^S is the bond force constant for the bond between atoms i and j and $r_{ij} - r_{ij}^0$ is the distance the atoms have moved from their equilibrium bond length r_{ij}^0 . Similarly, for the angles and improper dihedrals k_{ijk}^θ and $k_{ijkl}^{\varphi^{\text{imp}}}$ are the angle and improper dihedral (out of plane angle) force constant respectively, and $(\theta_{ijk} - \theta_{ijk}^0)$, $(\varphi_{ijkl}^{\text{imp}} - \varphi_{ijkl}^{\text{imp},0})$ are the change from equilibrium angle and improper dihedral. Finally, k^φ is the proper dihedrals (torsion angle) force constant, and n is multiplicity of the periodic function defining the proper dihedral potential and δ is its phase-shift.

The non-bonded force field terms contains dispersion interactions due to temporary dipole interactions that can arise between atoms [101]. The repulsion term arises from the repulsive interactions between electron densities when they are close to overlapping. Atoms can also interact with each other electrostatically if they are charged. The repulsion and van der Waals interactions are combined into a single approximation given by the

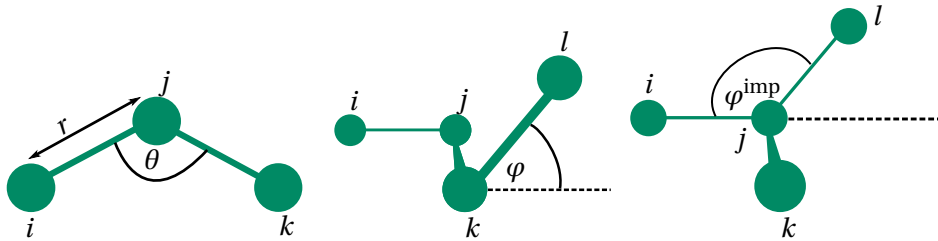


Figure 2.1: Depiction of the different bonded degrees of freedom. Left: the covalent bond potential acts between any two atoms i and j that are considered to be bonded together with distance $r = r_{ij}$ between them, and the angle potential depends on the angle between the three atoms i, j, k where $\theta = \theta_{ijk}$. Centre: The proper dihedral between four atoms i, j, k , and l depending on the angle between the planes defined by i, j, k and j, k, l where $\varphi = \varphi_{ijkl}$. Right: Improper dihedral between four bonded atoms.

Lennard-Jones potential defined as

$$U_{\text{LJ}}(\mathbf{X}) = \sum_{i,j>1} 4\epsilon_{ij} \left[\left(\frac{\sigma_{ij}}{r_{ij}} \right)^{12} - \left(\frac{\sigma_{ij}}{r_{ij}} \right)^6 \right] \quad (2.9)$$

where ϵ_{ij} is the depth of the potential between the two atoms i and j , σ_{ij} is the first zero of the Lennard-Jones potential for i, j , and $r_{ij} = |\mathbf{x}_i - \mathbf{x}_j|$ is the Euclidean distance between them. The two constants ϵ and σ are input parameters to the MD simulation. They are normally fitted to the interatomic interaction of atoms of the same element ϵ_{ii} and σ_{jj} . Mixing rules exist [102] that approximates the Lennard-Jones constants for different elements such as the Lorentz-Berthelot [72] rule where $\sigma_{ij} = \frac{1}{2}(\sigma_{ii} + \sigma_{jj})$ and $\epsilon_{ij} = (\epsilon_{ii}\epsilon_{jj})^{\frac{1}{2}}$.

MD simulation is a computational tool that exists as an intermediary between theoretical and experimental methods. In order to predict the results of experiments, one must be able to simulate bulk systems. However, this is impossible with current computational resources. Even systems of crystallites that contain on the order of 10^6 atoms, open boundary conditions would result in approximately 6% of atoms being on the boundary [87]. This leads to what are known as finite size effects [87, 103–105]. The intuitive solution to this problem is to simulate systems of size comparable to experimental scales. This entails simulating at least moles (10^{23}) of atoms which is impossible with current hardware limitations.

The solution to the finite size problem is to simulate bulk phases with Periodic Boundary Conditions (PBC). Figure 2.2 shows an example of a system of atoms (in red) in 2D surrounded by its periodic images (green) assuming a square box with side length L . The figure shows only a single layer of the periodic images, there are infinite images along each direction. Each particle then interacts with all of the particles in the simulation box, and all of the periodic images in all of the virtual boxes. This has just further complicated the potential as it now contains an infinite sum (recall that we assume potentials to be additive in MD), such that the total potential U_{tot} of the original system becomes [87]

$$U_{\text{tot}} = \frac{1}{2} \sum'_{i,j,\mathbf{n}} U(\mathbf{X} + \mathbf{n}L), \quad (2.10)$$

where $\mathbf{n} \in \mathbb{N}^3$ is a vector describing the coordinate of each box in units of L , the prime over the sum indicates that terms when $i = j$ are ignored when $\mathbf{n} = \mathbf{0}$. The issue of infinite sums is resolved in two ways:

1. Simple truncation and shift of the Lennard-Jones interaction. The shifted and truncated Lennard-Jones potential acting on particle i due to particle j is defined as

$$U_{\text{LJ}}^*(r_{ij}) = \begin{cases} U_{\text{LJ}}(r_{ij}) - U_{\text{LJ}}(r_{ij}^c) & \text{if } r_{ij} \leq r_{ij}^c, \\ 0 & \text{if } r_{ij} > r_{ij}^c, \end{cases} \quad (2.11)$$

where U_{LJ} was defined in Equation 2.9 and r_{ij}^c is the threshold truncation range. The truncation range is often set to $r_{ij}^c = 2.5\sigma_{ij}$ as the Lennard-Jones potential at $r_{ij} = 2.5\sigma_{ij}$ would have decayed to approximately 1/60th of the well depth ϵ_{ij} .

2. Minimum image convention. Atoms at the edge of the simulation boxes would have to interact with virtual particles due to the PBCs, even if the distance between them is greater than r_{ij}^c . Some of these interactions are shown in Figure 2.2.

The minimum image convention is enforced by the following correction to the distance calculation between particles i and j . Let r_{ij}^x be

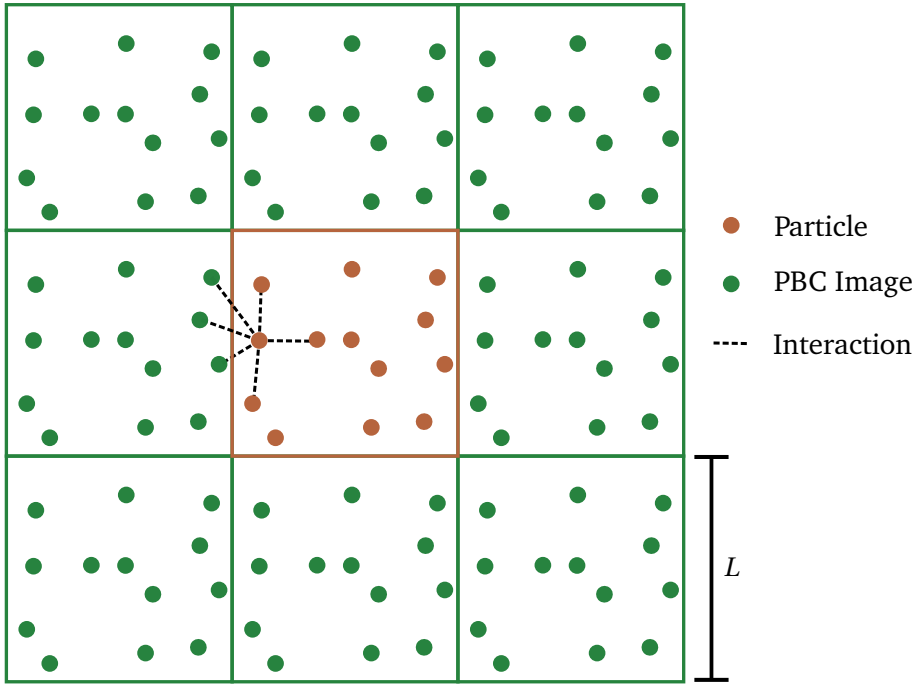


Figure 2.2: Depiction of periodic boundary conditions. The real atoms and molecules are represented by red particles and their periodic images by green particles. L is the box size. The dashed lines shows an example interaction abiding by the minimum image convention. Adapted from Figure 3.2 in [87].

the first component of the vector pointing between the two particles \mathbf{r}_{ij} , it is then corrected such that

$$r_{ij}^x = r_{ij}^x - L \left\lfloor \left(\frac{r_{ij}^x}{L} + 0.5 \right) \right\rfloor \quad (2.12)$$

in which $\lfloor a \rfloor$ returns the greatest integer smaller than a .

The remaining term in the force field is the evaluation of electrostatic interactions between charged atoms. This term is represented by a Coulombic term between two charged particles. However, similar to the Lennard-Jones terms, the electrostatic potential would have to be eval-

ated over an infinite number of boxes [87]:

$$U^{\text{Coul}} = \frac{1}{2} \sum_i q_i \phi(\mathbf{x}_i), \quad (2.13)$$

where we assume that the system is neutral ($\sum_i q_i = 0$), and $\phi(\mathbf{x}_i)$ is the Coulombic potential

$$\sum'_{j, \mathbf{n}} \frac{q_j}{\mathbf{r}_{ij} + \mathbf{n}L}, \quad (2.14)$$

where the prime indicates the sum over all periodic images with coordinate $\mathbf{n} \in \mathbb{N}^3$ with units of L (the box size), except the case when $i = j$ and $\mathbf{n} = \mathbf{0}$. We cannot apply the methods outlined above for the Lennard-Jones interactions here as the electrostatic interaction is a long-ranged one—it does not decay at a rate high enough to be amenable to truncating. This problem is resolved with Ewald sums [106–108]. Ewald sums are out of the scope of this thesis and will not be discussed here. Detailed discussions of Ewald sums are available in Refs. [87, 109–111].

2.1.1 Calculating MD Trajectories

Once a collection of potentials that describe the interactions between the atoms are approximated with the methods described before, the ODE described in Equation 2.2 is solved as an initial value problem for a set of initial conditions given by positions \mathbf{x}_i and momenta $\mathbf{p}_i = m_i \frac{d\mathbf{x}_i}{dt}$. Solving the ODE would lead to a trajectory in phase space (a $6N$ dimensional space spanned by all the positions and momenta) that describes the evolution of the system with the potentials described above. The complexity of the inter-atomic potentials makes solving the ODE analytically impossible, requiring the use of numerical methods to approximate the solution.

The formulation of MD above arose from the definition of the conservative forces, where the system in question is isolated from the environment and without any external influences. This requires that the total energy in the system is conserved [112]. Furthermore, the Newtonian equations of motion in this case are time reversible which requires the use of time reversible integrators. This means that the volume of the trajectory in phase space produced by solving the differential equations must

be incompressible (conserved volume). In other words the system is symplectic.

The details of the theory of symplectic systems and their relationship to MD are out of the scope of this thesis. We only summarize the Verlet integrator, which is a symplectic integrator [112–114], as an example integrator suitable to these systems. The Verlet integrator is defined as

$$\mathbf{x}_i(t + \Delta t) = 2\mathbf{x}_i(t) - \mathbf{x}_i(t - \Delta t) + \frac{\mathbf{F}_i(t)}{m_i} \cdot \Delta t^2 + O(\Delta t^4) \quad (2.15)$$

$$\mathbf{v}_i(t) = \frac{\mathbf{r}_i(t + \Delta t) - \mathbf{r}_i(t - \Delta t)}{2\Delta t} + O(\Delta t^2). \quad (2.16)$$

Discussion of various integrators and their use for different situations in MD are explained in greater detail in Refs. [112, 114, 115].

2.1.2 Simulations at Constant Temperature and/or Pressure

In the formulation above the system that we consider is completely isolated from its environment; it contains a constant number of particles (N), the volume of the box (V) is a constant, and the total energy is conserved. Simulations set up with initial positions of the atoms that can be either oriented randomly in the simulation box or on a regular lattice. A force field is chosen that is appropriate for the underlying system and the system is propagated forward in time with a symplectic integrator to produce a trajectory.

The formulation of MD as a system with only conservative forces leads to simulations of the microcanonical ensemble [87, 116], also known as NVE simulations. One assumes that the underlying system is ergodic, so time averages of any measurements are similar to ensemble averages. It is extremely difficult to run real experiments that are completely isolated from the environment. It is therefore necessary to develop methods that can allow the control of temperature and pressure in the simulations. The formulation of the dynamic equations of motion above can be augmented to create constant temperature (NVT), or constant pressure and temperature (NPT) [87, 117] simulations. The algorithms used to create such simulations are named *thermostats* and *barostats*. Discussions of how they are implemented and the derivation of the equations of motion in their frameworks are described in [81, 82, 87, 118–121].

2.2 Coarse-Grained Molecular Dynamics

The discussion so far has been regarding MD simulations of molecules at the atomic level of description, i.e. each particle in a simulation represents a real atom. MD has been successfully used to make predictions regarding a wide variety of systems of macromolecules, such as the conformational properties of small intrinsically disordered proteins [74] and exploring unknown structures of two charged proteins interacting with each other [122]. This is, however, an incomplete picture. Macromolecules such as proteins can contain many millions of atoms within them, leading to degrees of freedom that can span many orders of magnitude in time. Atomic vibrations occur on the fs time scales [123], whereas changes in the conformations of large macromolecules such as proteins [124] can require anywhere from 1 μ s to 1000 s [123, 125]. Cell growth can occur over minutes, hours, or days [126–128]. So how can one even attempt to simulate cells with MD?

Studying the aforementioned slow dynamics within molecular (and other larger systems) is possible with the coarse-graining (CG) [77, 85, 123, 129–132]. The recent review by Noid *et al.* [117] offers a detailed description of CG methods and their successes in the field of MD for proteins, nucleic acids, and water. We summarize a few details here to provide context for *CellSim3D* [42], a CG model for cell growth and mechanics introduced in Chapter 5 of this thesis.

In the atomically detailed models described by, e.g. the CHARMM [94] force field, each particle represents an atom in each of the molecules in the system. In CG methods particles represent collections of one or more atoms, effectively eliminating the faster degrees of freedom in the system. This, in a way, is similar in spirit to the Born-Oppenheimer approximation [92, 93]. After assuming that electronic degrees of freedom relax fast to create atomistic representations, we also assume small fast atoms in the system relax quickly to create CG representations. The CG description is thus based on the atomistic reference structure from all-atom positions with a mapping M defined as

$$\mathbf{R}_I = M_I(\mathbf{X}) = \sum_i C_{Ii} \mathbf{x}_i \quad (2.17)$$

where \mathbf{R}_I is the position of the I th CG particle, and \mathbf{x}_i is the position of

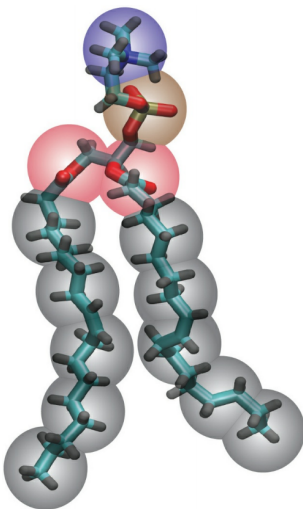


Figure 2.3: Depiction showing the coarse-graining (CG) map for dioleoylphosphatidylcholine (DOPC), a common molecule used to simulate animal cell membranes [134]. Martini CG particles are shown as cyan transparent spheres overlaying the atomistic particles. Taken from Figure 2 in Ref. [134], CC license.

the i th atom in the atomistic description. An example of the MARTINI mapping for lipids [69, 133] is shown in Figure 2.3.

CG is then the process of defining this map. We describe two strategies of defining, and then optimizing the mapping M [117, 129] shown in Figure 2.4. In the bottom-up approach information from the underlying atomistic system is used to optimize the precise properties of the CG map M . The next step is to define the new force fields that act between the CG particles. Once the new particles have been mapped and the force fields between them defined, one can proceed to apply the MD algorithm onto them. Thus, much larger simulations can be run with greater time steps. There are three [85, 129] common ways, often combined with each other, to optimize such bottom-up maps:

1. Energy based as in the MARTINI model for lipids [69], proteins [135], carbohydrates [136], water [137], and supramolecular polymers [77]. Here, the CG particles and force fields are parametrized to reproduce the free energies or energies of the underlying atomistic system.
2. Force matching such as in the model for transmembrane proteins due to Ayton *et al.* [138]. In this method the CG map and force field is optimized such that the sum acting on a CG bead is the sum of the forces of all the atoms within it.

3. Structure based, as in the CG models for complex fluids [139, 140] Wherein the mapping and force field are optimized by ensuring that the average structures (such as the radial distribution function) of the CG representation of the macromolecules are similar to the atomistic representation.

Bottom-up methods offer an attractive method to take known high quality, validated atomistic models and push them to higher time and length scales. Thus, bottom-up methods can be used to make predictions of situations that have no known experimental observations. Nevertheless, they do require that an atomistic description exists to begin with. In contrast, top-down methods do not require the existence of atomistic models to work. They instead use either already known experimentally observed phenomena to, or information from higher models that are themselves more coarse, e.g. classical phase-field models [141]. Top-down models provide an elegant method for simulating non-trivial emergent phenomena that result from physical principles included in the CG model [117, 142]. Examples of top-down methods include the many models for cell behaviour that are described in Section 3.4, and the *Cell-Sim3D* [42] model.

One should note however that in most cases the distinction between which model is a strictly top-down model and which is a strictly bottom-up model becomes blurred as both methods are often used to refine CG models [117, 123] and to gain new insights about the underlying system. A detailed description of both approaches being applied to supramolecular polymers is available in Ref. [78]. The MARTINI model [69, 143] that we mentioned above uses both bottom-up and top-down parametrization techniques.

2.2.1 Solvent Free Models

The solvent is a vital component of most biomolecular systems [117, 123]. While the main macromolecular component is important, the dynamics that it undergoes is a function of its interactions with the solvent surrounding it. Solvent effects are vital in many processes such as the self-assembly of colloidal systems [142, 144], lipid bilayers and vesicles [145], and the stability of supramolecular polymers [78, 146]. Therefore, the choice and

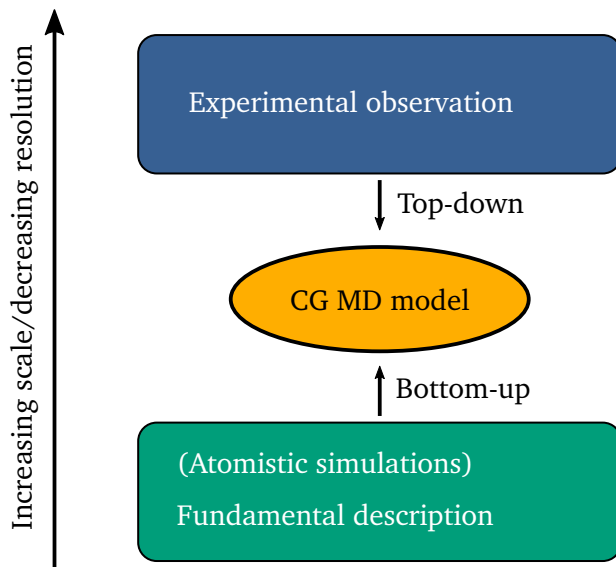


Figure 2.4: Schematic of top-down and bottom down coarse-graining. In the bottom-up approach, information from fundamental first principles is used to create atomistic models, which can then be used build coarse-grained (CG). In the top-down approach, the CG description is optimized to reproduce data and/or structures from experimental observations. Figure Adapted from Figure 2 in [117] with permission from the American Institute of Physics Publishing.

modelling of solvents is a vital aspect of designing high quality MD simulations. However, solvent molecules add significant computational costs to running large scale MD simulations [129]. This cost is eliminated in CG models that adjust the inter-particle potentials to account for interactions with solvent. These models are called implicit solvent[147, 148], or dry, models. Examples of such models include dry MARTINI [68, 143], and the generalized Born model [149]. Implicit solvent simulations can be considerably faster than regular CG models [143, 148] as there are fewer degrees of freedom in the system. However, they can neglect some important features of solvent interactions such as, in the case of polar solvents, hydrogen bond fluctuations during conformational reorientations of the solute. Implicit models are best used for solvents that are interact isotropically with the solute [147, 148]

2.2.2 Dissipative Particle Dynamics

So far, the discussion has been of models that are used to study microscale systems with millions of atoms (or CG particles) system sizes on the order of 100 nm. We now discuss systems in which particles themselves are much larger, on the order of 10nm to 1 μ m, such as in colloidal systems [150–152] or on the order of 10 to 100 μ m as in the case of cells [11, 153]. The hydrodynamics of the solvent system and how it interacts with the mesoscale objects cannot be ignored as the solvent may cause the flow and/or Brownian motion of the system [87, 154] which is not negligible on mesoscale timescales. Mesoscale models can be used [123] to study such systems. Mesoscale models include Dissipative Particle Dynamics (DPD) [155, 156], and the Lattice Boltzmann (LB) [157, 158] model. DPD is one of the most commonly used and simplest models to study mesoscale systems [123]. In this thesis, we use the basic principle of DPD and apply it to cellular systems, though we assume that the membranes do not undergo Brownian motion (details in Chapter 5).

The basic DPD algorithm is similar to MD, the main difference being the addition of a damping and a random noise term. In a DPD system, the force acting on particle i due to interactions with particle j is given by

$$\mathbf{F}_i = \sum_{j \neq i} [\mathbf{F}^C + \mathbf{F}^D(\mathbf{r}_{ij}, \mathbf{v}_{ij}) + \mathbf{F}^R(\mathbf{r}_{ij})], \quad (2.18)$$

\mathbf{F}^C is the conservative force, exactly the same as the conservative forces in atomistic MD and CG MD systems, \mathbf{F}^D is the dissipative component of the interaction with the solvent, \mathbf{F}^R is random noise also associated with thermal interaction with the solvent, $\mathbf{r}_{ij} = \mathbf{x}_i - \mathbf{x}_j$, and $\mathbf{v}_{ij} = \mathbf{v}_i - \mathbf{v}_j$ ($\mathbf{v}_i = \frac{d\mathbf{x}_i}{dt}$). The dissipative and random terms are given by

$$\mathbf{F}^D(\mathbf{r}_{ij}, \mathbf{v}_{ij}) = -\gamma \omega^D(r_{ij}) (\mathbf{v}_{ij} \cdot \hat{\mathbf{r}}_{ij}) \hat{\mathbf{r}}_{ij}, \quad (2.19)$$

and

$$\mathbf{F}^R(\mathbf{r}_{ij}) = \sigma \omega^R(r_{ij}) \xi_{ij} \hat{\mathbf{r}}_{ij}, \quad (2.20)$$

where γ is the friction coefficient, σ is the random force coefficient, ξ_{ij} is a random variable distributed normally with unit variance, and $r_{ij} = \|\mathbf{r}_{ij}\|$. The weight functions $\omega^D(r_{ij})$ and $\omega^R(r_{ij})$ describe the strength of the dissipative and random forces respectively as a function of the interparticle distance. The two are necessarily related by [159]

$$\omega^D(r_{ij}) = [\omega^R(r_{ij})]^2, \quad (2.21)$$

while the random force and friction coefficients are related to the temperature T and the Boltzmann constant as

$$\sigma^2 = 2k_B T \gamma. \quad (2.22)$$

Since the forces in DPD depend on both positions *and* velocities, using a Verlet type integrator would not be appropriate since they split the position and velocity updates into two steps (the Verlet integrator was described in Section 2.1.1). Many variations of the Verlet integration scheme have been proposed; see Refs. [123, 160, 161] for a detailed discussion and comparison of different integrators for this system. In this work we use the DPD-VV integrator proposed by Besold *et al.* [160]. The DPD-VV integrator is described in Section 5.2.3.

Chapter 3

The Cell From a Mechanical Perspective

The cell is an incredibly complex entity with many phenomena occurring over multiple time and length scales from the quantum (such as with photosynthesis in some plant cells) up to the classical (such as in the growth of a tree or animal). This is further complicated by the interdependence of the processes between the different size scales (such as a tree's growth into a shaded region slowing down photosynthesis, and consequently slowing down the tree's growth). It would be impossible to capture all of this complexity in one's lifetime, let alone a single thesis or project. We shall see in the first section of this chapter, that there are many interesting facets of cell behaviour that connect cell biology to cell mechanics. Our interest is to understand this reciprocity between the mechanical and biological aspects of cell behaviour. Due to the complexity of this topic, we must see what assumptions we can make about the cell's structure to be able to continue. Therefore, in this chapter, we shall explore the properties of cells that we can use to make some simplifying assumptions about the system, which for us is a single or a collection of cells interacting with each other and some medium.

To begin we first introduce some rudimentary cell biology in the first section of this chapter Section 3.1. The depth and breadth of this topic is far outside the scope of this thesis (or any single thesis for that matter). But it is important to give ourselves some background information

that can shed some light on the validity of the assumptions made in our studies that follow later in this thesis. Biological facts that are not captured by our models will also be a source to propose improvements that can be made to our research as we go forward. Note that the biology described Section 3.1 largely only pertains to the phenomena that involve some sort of interaction between mechanics and cell behaviour. We shall ignore many other details about cell biology. Readers interested in a well-rounded review should seek it in standard textbooks such as Refs. [11, 162, 163].

The central assumption, or collection of assumptions, in this thesis is the notion of a *mechanical* cell. This object approximates the entire cell with only its mechanical parts. An explanation of this idea with some justification is given in Section 3.2. Many of the existing computational models of cells can be thought of as based on the mechanical cell. That is certainly for the model described in this thesis later in Chapter 5.

We then explain how the mechanical cell can be used to study cell growth and division in Section 3.3. This will be most applicable to the *CellSim3D* [42] model, described in Chapter 5, but it may be useful to any model developers who wish to approximate the process of a cell dividing into two child cells, known as *cytokinesis*.

Finally, a non-comprehensive review of models for cell behaviour is given in Section 3.4. There we discuss some cell models that can be used to study the physical properties of cellular tissues.

3.1 A Short Introduction to Cell Structure

Cells can be categorized into two types: prokaryotes and eukaryotes. Most prokaryotes are unicellular organisms. Figure 3.1 shows a schematic of a prokaryotic cell, and Figure 3.2 shows one of a eukaryotic cell. Both types of cells contain bodies that have specialized tasks such as the cytoskeleton (govern the mechanical structure of the cell), ribosomes (involved in protein synthesis), or the cell membrane which acts as a selective barrier that controls the inflow and outflow of material. However, the cells differ greatly from each other too. Prokaryotic cells tend to be much smaller than eukaryotic cells with diameters of about 1 to 10 μm [11]. The genetic information is stored in a somewhat jumbled aggregate of genetic mate-

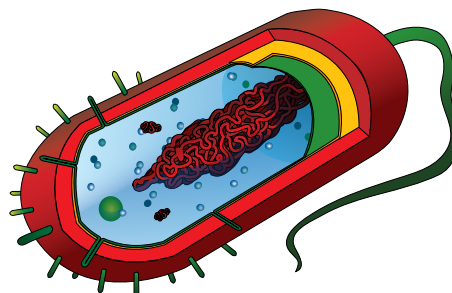


Figure 3.1: A prokaryotic cell. All bacteria are prokaryotes. This type of cell can be enveloped by a capsid and does not contain any specialized components in contrast to eukaryotes. Surprisingly, the human body may contain roughly the same number of cells, if not more, of these type of cells than human cells [164]. The image here shows various other structures around the bacterium as well such as flagella or villi [11], which are not necessarily universal, but give a general impression of what a bacterium may look like. Image created by Mariana Ruiz Villarreal, Public Domain, available at <https://commons.wikimedia.org/w/index.php?curid=3648821>

rial, sometimes known as the nuclear region [11]—which is not a nucleus. They also tend to grow much faster than eukaryotic cells. Prokaryotes may also be equipped with flagella that can be used for motion. Compartmentalization of functionality into specialized bodies is also absent in prokaryotic cells.

Eukaryotic cells on the other hand are much larger by comparison [11] with diameters ranging from 10 to 100 μm , and they have a more complex structure overall. While they too are also enveloped by a cell membrane, and plant cells can also be surrounded by rigid cell walls as well, they have other membrane enclosed objects within them named organelles. Organelles are specialized mini-organs within the eukaryote that have specific functions, such as energy generation, intracellular transport, or storage of biochemicals. Another thing that eukaryotes have that prokaryotes do not is the nucleus, which organizes all of their DNA into very dense and complex protein-DNA complexes named chromatin. Nuclei also manage the transcription and replication of DNA.

Eukaryotes can be single celled organisms themselves, or they can self-

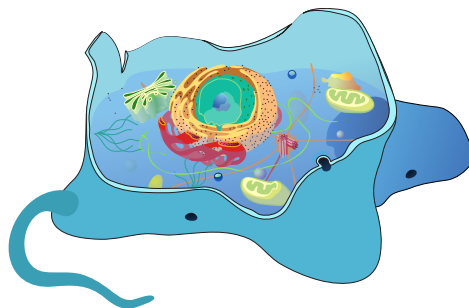


Figure 3.2: A eukaryotic animal cell. Plant cells are, for our purposes, quite similar with the addition of a cell wall. The human body contains on the order of 10^{13} [164] cells. Groups of these cells, organs, can have specialized functionality but they all stem from common ancestors. Image created by Mariana Ruiz Villarreal, Public Domain, <https://commons.wikimedia.org/w/index.php?curid=4266142>.

assemble to create a whole host of living organism. The human body contains about 30 trillion cells [164], which are organized into organs. In this thesis, the models that are used to study cells can be used to study either type of cells since we only focus only on the mechanical properties. As we will see later, the distinctions between prokaryotes and eukaryotes will not be of great significance. We will distill the *physical*, or *mechanical*, properties of cells into a simpler structure (see Section 3.2) that can be used for either type of cell. Perhaps one of the most interesting properties of such models is that they are applicable to many types of cells.

3.2 The Mechanical Cell

The Mechanical Cell is a model that only approximates its mechanical properties. We will ignore all biology and chemistry for now, and focus only on the components of the cell that give it its mechanical properties, such as stiffness, pressure, adhesion to other cells and environment. Figure 3.3 shows a cartoon of the major components of the cell that we focus on. The major components shown Figure 3.3 are the cell boundary, interior, and exterior (environment). Cell boundaries, an approximation of the cell membrane and cell wall (if one exists in the species we are interested in), and the actomyosin cortex are discussed in Section 3.2.1. The

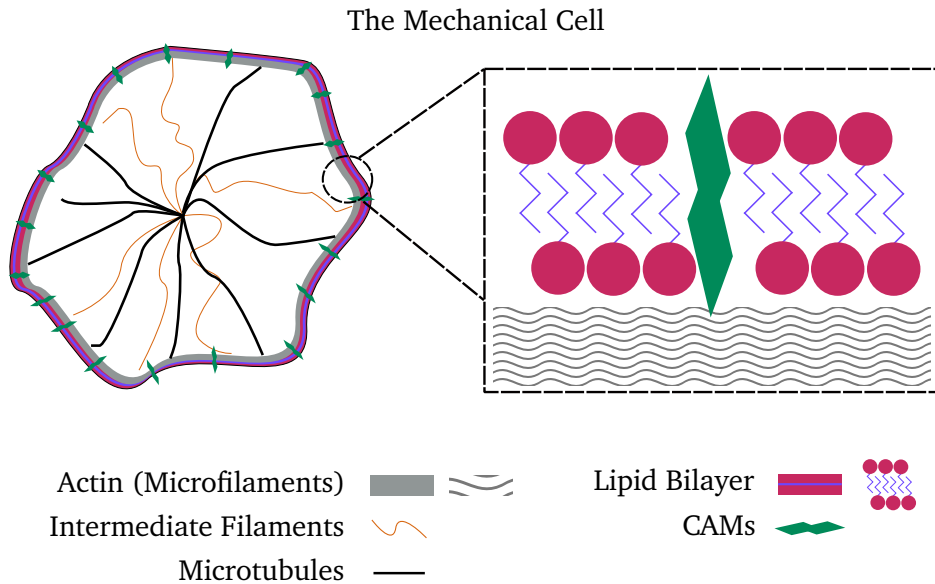


Figure 3.3: A simplified model of the cell [11]. This structure shows the basic parts of the cell that we will focus on in this thesis. The CellSim3D [42] model was developed based on this idea. We see here the cell's actomyosin cortex, microtubules, and intermediate filaments. These three together give the cell its mechanical properties. The white space in this figure outside the cell is the extracellular matrix (ECM). The membrane contains Cell Adhesion Molecules (CAMs) that act as adhesion sites with other cells and with the ECM.

interior of the cell, which is composed of the organelles and cytoplasm are discussed in Section 3.2.2. The interactions between cell and environment (the cell being approximated by only its boundary) are discussed in Section 3.2.3.

An important component missing from the *mechanical* cell is the nucleus which can play important roles in the biomechanics, and therefore mechanotransduction, of various types of cells. However, not all cells contain nuclei [11, 162, 163]. We assume that the nucleus does not play an important role for our model.

3.2.1 The Cell Boundary

The outer surface of cells is made of two components: the cell membrane, and the actomyosin cortex [165, 166]. There are whole fields of study dedicated to understanding these two components alone. We neglect many of the details of these objects for our model. However, as we shall see below, we can borrow that information known about the mechanical properties of the cell boundary to develop models that can be used to study cell and tissue growth. An approximation of the cell boundary is shown in Figure 3.3. This image represents simplified image of the cell membrane and cytoskeleton that can be used to simulate cell mechanics. Readers are referred to Refs. [68, 167, 168] for recent reviews on the modelling of cell membranes.

The cell membrane is a highly dynamic structure that envelopes the whole cell. It is made up of a phospholipid¹ bilayer dotted with different kinds of proteins and oligosaccharides² [169–172]. In addition to these complexities, it also acts as a gateway to the outside world with pores opening and closing to allow the passage of materials from inside to outside the cells and vice versa [11, 166] (this is not depicted in Figure 3.3 for the sake of simplicity). Lombard *et al.* [165] gave them the elegant name of “selective barriers” that control the crossing of various materials into and out of the cells. These membranes themselves do not have the strength required to support the cell’s shape. In bacterial, plant, and fungal cells, cells are surrounded with rigid cell walls that give the cell a well defined shape [173, 174]. In animal cells, the elastic properties of the cells are based on the cytoskeleton composed of the *actomyosin cortex* [11, 175].

The actomyosin cortex is a network of protein fibres, named F-actin [19, 174, 176, 177]. The fibres are oriented around the cell to create a mesh that envelopes the whole cell. F-actin is itself a supramolecular polymer, made of G-actin. Thus, the fibre length is dependent upon the polymerization of G-actin. The actin fibres interact with each other through non-bonded interactions, but they can also be attached to each other by molecular motors, myosin. The myosin motors consume energy (via the ADP-

¹A phospholipid, to simplify greatly, is a fatty acid with phosphate groups in the hydrophilic head.

²An oligosaccharide is a short sugar chain. Sucrose, table sugar, is a disaccharide.

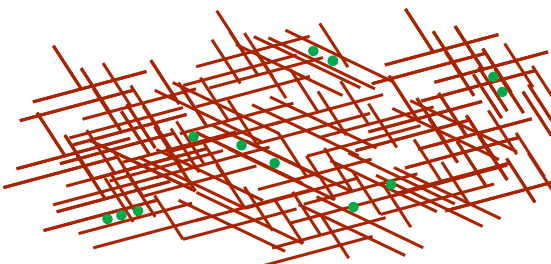


Figure 3.4: Actin fibers are shown in red and myosin motors in green. The actin fibers are interacting with each other in a non-bonded manner. But the myosin also creates an active binding between the fibers. The concentration and activity of myosin can alter the average stiffness and viscosity of the whole network [11, 175, 178, 179].

ATP reaction) and walk along the fibres [11, 175]. When the myosin motors are attached to two fibres, they drive them along each other. This is yet another factor that contributes to cortex dynamics. Figure 3.4 shows a facsimile of the actomyosin network near the surface of cells. Actin fibers are shown in red, and myosin motors in green.

Cells can regulate the polymerization of actin, and the activity and concentration of myosin motors, to induce a whole host of fascinating movements of the cell. These two small effects play a key role in every cellular function that entails any sort of mechanical force generation, including cell growth, migration, and interactions with other cells or Extracellular Matrix.

In most mechanical models, the membrane and actomyosin cortex are treated as a single object that has some mechanical properties such as stiffness, and viscosity associated with its deformation. A non-comprehensive review of such models for cells is given in Section 3.4. In those models, the properties of the cell boundary are either constant, or not simulated. *CellSim3D* [42] (Chapter 5) is such a model as well. There are some models in the literature that study the membrane and actomyosin cortex more explicitly, such as the models in [180, 181]. From this point onward, we will use the terms actomyosin cortex, cell membrane, or just membrane, to refer to the combined structure of the cellular envelope.

Cell Adhesion Molecules and Focal Points

Apart from defining the cell shape, the cell membrane contains many proteins, named Cell Adhesion Molecules (CAMs) that mediate interactions with the cells environment, and with other cells. This family of proteins are divided into many categories: integrins, selectins, cadherins, and more [182]. CAMs bind to other cells through ligands. The ligands themselves can be other CAMs. The binding can be specific [182], but for the purposes of mechanical modelling, they can be treated as simple adhesion points. The type and quantity of these proteins in the membrane is regulated by the cell, which is yet another way the cell can actively modify its mechanical properties. When the cell is in need of stronger or more persistent adhesion sites, focal points with larger than average concentration of CAMs can be created to strengthen the binding with the substrate [183]. Cells can modify focal adhesion points in response to changes in the biochemical signatures, and stresses in their environment [183].

While necessary for the adhesion of the cells with their neighbours, CAMs are also known to play a role in various biological processes. For example, selective adhesion directs the development of embryos during early development [182].

Interested readers are advised to read Ref. [184] and Ref. [34] for more detailed descriptions of the cell membrane and [182, 185, 186] for information regarding cell adhesion.

3.2.2 The Cell Interior

We saw in Figure 3.1 and Figure 3.2 that the insides of cells are filled with various other bodies that make developing models for cells difficult. We shall assume that all the mechanical properties of the cell only derive from certain internal components and that most of the organelles tend to be small or soft, and do not contribute to mechanical properties of cells at the surface of cells.

The mechanical properties of the cell interior are a result of the cytoskeleton network which are common to most eukaryotic cells [187]³,

³There are many authors that regard the cell membrane as part of the cytoskeleton. As far as we are concerned, this is purely terminology. We assert that the membrane is not part of the cytoskeleton here, but it does not ultimately matter whether it is or is not

the most notable exception to this are red blood cells. These networks are made of long protein self-assembled supramolecular polymers and the cytoplasm. These polymers exist in a dynamic equilibrium within a bath of monomers, much like the actin fibers in the cell membrane. Thus, the cytoskeletal polymers are constantly polymerizing and depolymerizing at their ends. The cytoplasm can be treated as a Newtonian viscous fluid that is contained within the cell [20, 188]. It also contributes to the cell's structure and shape due to hydrostatic pressure [189–193] arising from differences in osmolyte concentrations in the cytoplasm compared to the outside of the cell. This effect is also dependent on the contractile strength of the actomyosin cortex. The fibres of the cytoskeleton provide support for the transmission of both intracellular and extracellular cues throughout the cell.

Intermediate filaments and microtubules together give the cell body its strength and stability in the outward radial directions [194]. These components are absent in prokaryotic cells which have other strategies to improve their elastic strength, such as stiff capsids. Intermediate filaments are present in both the cell nucleus and cytoplasm. Microtubules only exist in the cytoplasm. Together, the microtubule and intermediate filament network act as mechanical shock absorbers for the cell and are key components in the transport of mechanical signals from the cell boundary to the cell interior. The microtubule network is also an essential part of endocytosis [195–197]. Readers are referred to [187, 198, 199] for more details.

3.2.3 The Cell Exterior

Cells do not always just exist freely in liquid. Especially in organs there are a great deal of three dimensional scaffolds that the cells can be embedded in, the extracellular matrix (ECM). These scaffolds can be made of a variety of proteins. The most commonly known one is collagen, but there are others as well such as elastin, fibronectin, and laminins [200]. The proteins bind to each other and the adhesion proteins of cells. It is the mechanical properties of the ECM and cells combined that give organs their final mechanical properties.

Highly dynamic feedback loops exist between the ECM and the cells [201–203]. The ECM is not simply a mechanical scaffold. The cells can main-

tain and alter the properties of the ECM surrounding them, and alter their properties to better suit their needs. Diseased cells, for example, can change the properties of ECM taken from healthy tissue. Even ECM altered or produced by unhealthy cells can affect the health of normal cells [204].

The ECM also has a major role in cell migration, cells are known to favour certain types of ECM over others, and they will migrate to areas that are more favourable. Both the biochemical and biomechanical signatures of the ECM play important roles in migration. See [200, 204] for more details on this topic.

3.3 Cell Growth and Division

The different parts of the cell's life cycle are shown in Figure 3.5. The cell's cycle can be thought to contain four phases [11, 205]: two growth phases (G_1 , G_2), synthesis (S), and mitosis (M). Most of the growth occurs during G_1 and G_2 , with the addition of error checking of DNA replication in G_2 . DNA replication occurs in the S phase, which is typically the longest phase and can take about half the cell cycle time to finish. Mitosis is the shortest phase and is typically a small part of the cell life cycle time. Cells also enter a resting state, G_0 which may persist for very long times (up to years) [206].

The cell cycle can be summarized as follows:

1. Interphase:

This phase is between the moment a cell is born until it divides. Cells spend most of their time in this phase carrying out their function, however there are portions of this phase during which they grow.

(a) G_0 : Differentiation and growth control

This phase is actually outside the cycle and it is also known as “senescence”. This is the time during which the cells are highly active carrying out their functions (being a liver cell, or being a pancreas cell), which can entail their movement. A stem cell can differentiate into a different cell type during this phase. This state is not necessarily permanent, the cell can pass into the G_1 phase and reenter the cycle to grow again.

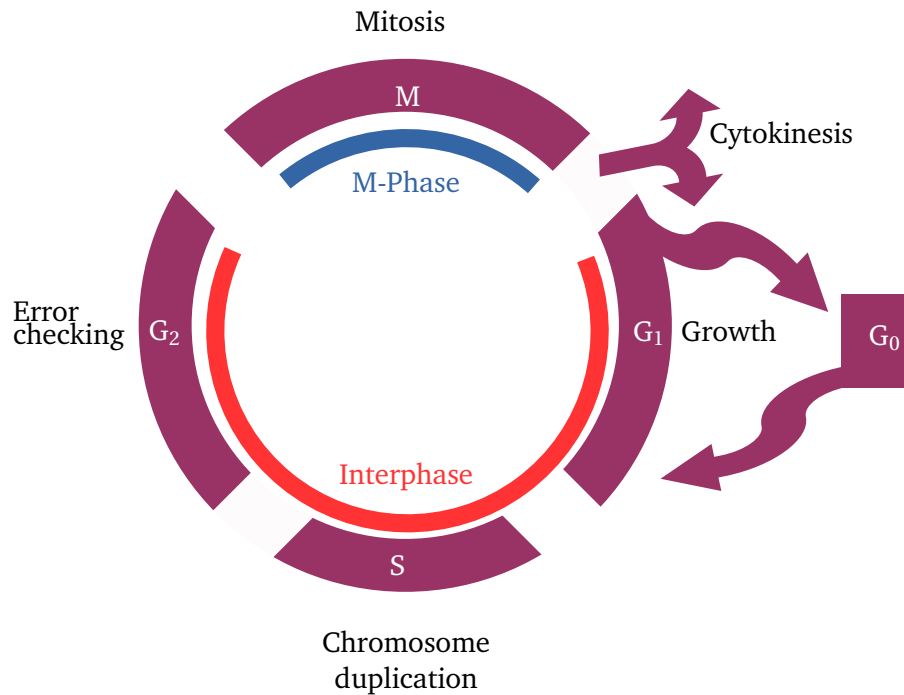


Figure 3.5: Depiction of the eukaryotic (animal and plant) cell cycle. Most time is spent in the Interphase, when growth and function is taking place. Cell division occurs during M-phase. All cells are either at some point along this cycle, or in G₀ phase. Adapted from Figure 40-2 in [11].

(b) **G₁: First gap phase**

This phase of the cell cycle lasts the longest. When a new cell completes G₁, it will have roughly doubled in size. At the beginning the cell checks for some sort of trigger for cell growth. It is not clear what could trigger this [207]. A possible trigger may be the presence, or sufficient concentration, of some growth hormone. There are checks for sufficient nutrient level for growth (increase in mass or volume) [11].

The growth of cells occurs by the transport of material from outside the cells, into the cell. This increases the cell's mass and propels it forwards toward M phase [205, 208].

(c) **Synthesis phase (S): DNA replication**

Eukaryotic DNA can be highly complex and long (human DNA is estimated to be two to three metres in length [11, 209]), so its replication must be controlled. Replication occurs at multiple points of the DNA strand for efficiency. The duplicate copies of DNA are linked together in a protein complex for error checking

(d) **G₂: Second gap phase**

The DNA duplicates are checked for damage or replication errors. This phase is relatively short. Mitosis is triggered, when a threshold of mitosis related enzymes concentration and activity is reached.

2. Mitosis phase (M)

Once the business of growing the cell is completed, the cell moves the copies of DNA (known as chromatids) to opposite ends of a cellular scaffold named the mitotic spindle. The spindle is a stiff bundle of proteins that define the orientation of cell division. Once DNA is sent to the different ends of the spindle, cytokinesis (the cleaving of the cell into two), the next phase of the cycle, can begin. Cytokinesis proceeds in five steps. Some of these steps are shown in Figure 3.6. There is also other forms of cell division, meiosis [210] and binary fission [211], which we do not discuss here.

(a) Prophase: Mitotic spindle formation

The protein fibers of the cytoskeleton self-assemble into a spindle that will determine the placement of the two daughter cells.

(b) Prometaphase: Nuclear breakdown

Nucleus is broken down and the chromatids begin their journey along the mitotic spindle to the two sides of the parent cell.

(c) Metaphase: Mid-point

Chromatids are about halfway across the mitotic spindle to the other side.

(d) Anaphase: Chromatid Separation

Chromatids separate and begin moving to the opposite sides of the mitotic spindle. The cell starts to develop the furrow along which division will occur.

(e) Telophase: Nuclear reformation

Nuclei form around the chromatids on either side of the parent cell.

3. Cytokinesis: The separation of two daughter cells from the parent cell

This process is not yet completely understood [212], but we can discuss the basics of what is going on. It is not completely accurate to say that cytokinesis occurs strictly after the M phase, it is happening more or less in parallel [11]. As M-phase is carrying on, an actomyosin band is formed perpendicular to the mitotic spindle, such that it divides the parent cell into two halves. The band is shown in light and dark blue in Figure 3.6. The band is actively consuming energy, strengthening, and pinching the two halves of the parent cell away from each other. Over time, the spindle dissolves away and the cell membrane is deformed in its centre far enough to be joined, and the two daughter cells are left. Ref. [212] provides a detailed discussion of cytokinesis.

3.3.1 The role of division plane alignment

An important geometric property of cell division is the orientation of the cell division plane[213–215]. This is the plane along which the mitotic

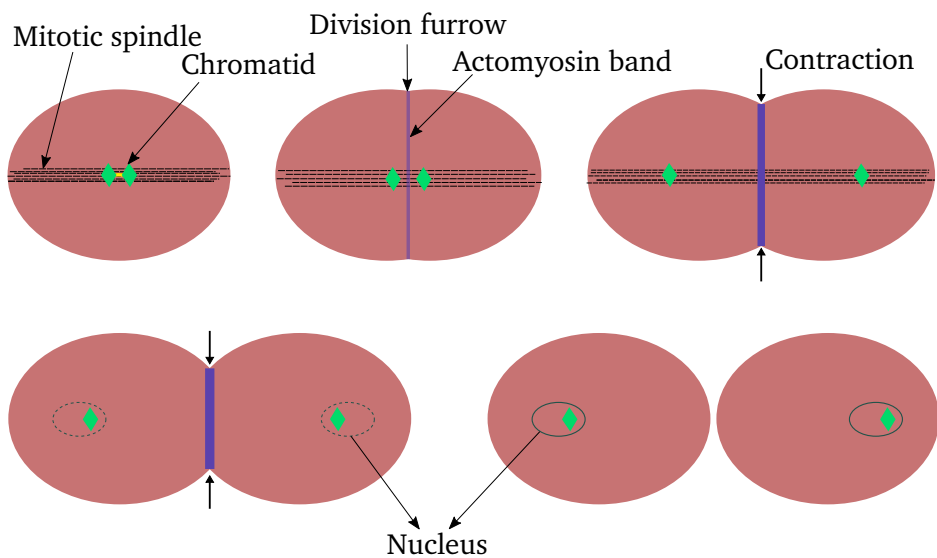


Figure 3.6: This schematic shows the steps involved in cytokinesis. Once the cell has reached sufficient size, the chromatid complex, the duplicated DNA, is placed along the mitotic spindle (a self-assembled stiff band of microtubules that stretches along the cell). As the chromatid separates and the DNA is moved to the opposite sides of the cell, an actomyosin band is formed perpendicular to the mitotic spindle and contracts to furrow the cell membrane. Over time the contraction strengthens and increases the furrowing. Simultaneously, a nucleus begins to form around the genetic material (chromatids) as the two cells start to separate.

furrow is developed during cell fission. It is necessarily defined by the actin contractile ring, shown in blue in Figure 3.6. The ring must be formed consistently to generate complex multi-cellular organisms [216, 217]. A change in division plane orientation and location is also a hallmark of cells differentiating into different cells [216, 218]. This is thought to be a consequence of the positioning and the structure of the mitotic spindle.

The orientation of the division plane, and how it is selected can vary between different species of cells. But instead on discussing the biochemical nature of this process, we will only focus on the possible outcomes of the process and explore the possible orientations of division plane. Most commonly accepted alignments of division planes are discussed below.

There are two possibilities for the location of the cell division plane, either the division plane can pass through the centre of mass of the cell (since cells are more or less uniform in density, this is often the same as their centroid) or through some other point inside the cell. The random point could be different for each cell, and it generally results in asymmetric division. Figure 3.7 depicts these two kinds of division. Child cells that are the result of symmetric division are identical, and those that a result of asymmetric division are different. This off-centre positioning of the division plane, is one of the ways that cells can convert into cells of different type. Consequently, the two child cells may also have different masses. For example, a stem cell can start by dividing this way into another cell, say a liver cell, then the liver cell continues to produce more liver cells ⁴.

When passing through the cell's centre of mass, the orientation of the division plane can also be chosen with variety of different rules (not quite rules, but observed to be consistent most of the time in experiments). Hertwig's rule states that the division plane is oriented perpendicular to the longest axis of an ellipsoidal cell, and passing through the centre of mass [219]. Errera's rule is possibly the same as Hertwig's which states that the division plane must contain the shortest path running through the centre of mass of a cell [220]. These two rules would produce identical child cells, such that the cells are produced in the same direction between generations, so we refer to them as *consistent* division plane alignment.

⁴We do not claim that this is how whole livers are created in reality. It is only one of the many possible steps involved.

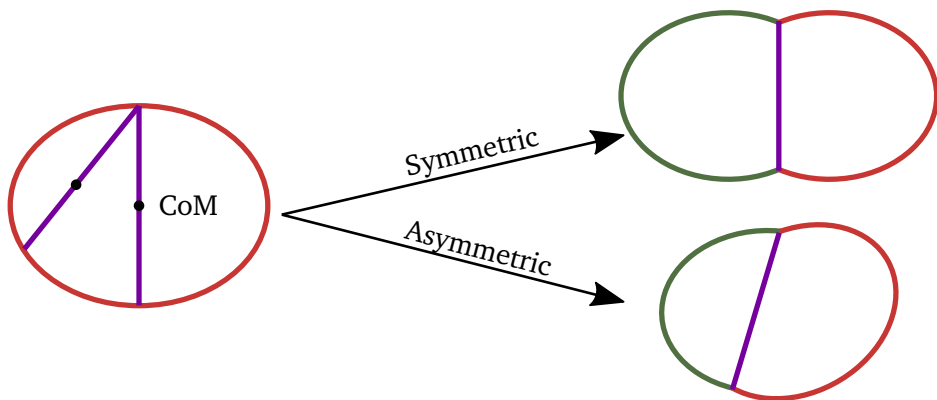


Figure 3.7: Cross-section of symmetric and asymmetric cell division. The parent cell is shown on the left before with two possible division planes. Organelles are not shown for simplicity. Symmetric division plane alignment produces identical child cells, asymmetric division plane alignment produces different cells that may have different organelles and biomechanical properties.

Consistent plane alignment can also be such that the alignment changes slightly between generations and producing interesting spiral patterns. However, the division plane can also be aligned randomly and produce spherical (or disk shaped) tissue. Figure 3.8 show some examples of the systems with these two types of division plane alignment types. In this thesis, we only focus on symmetric and random cell division.

3.4 Current Models For Simulating Cell Behaviour

The topic of modelling behaviour is a deep and interesting one. As we discussed in Chapter 3, there many aspects of cell behaviour that can be studied computationally. This stems from the inherently multi-scalar nature of cells, with vital processes spanning many orders of magnitude in time and length scale. At the atomistic scale there are complex vast networks of chemical reactions that govern the various elements of cell biology, and may involve reactions between small and large molecules. A classic example of this protein is synthesis which involves DNA, RNA, amino acids, and other proteins [221, 222]. For all of the myriad processes there are

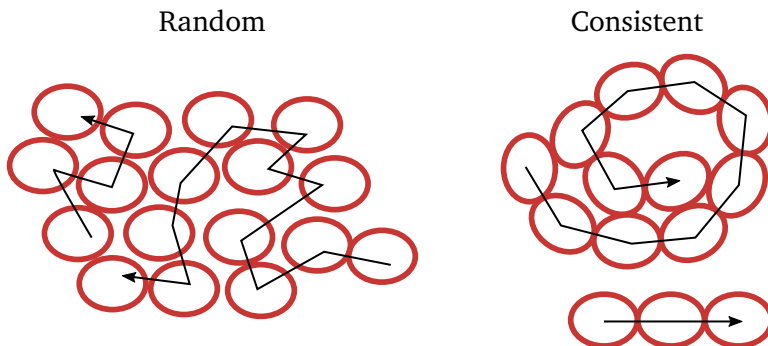


Figure 3.8: Results of random and consistent division. Arrows show each successive generation. Left: A system of cells resulting from random division plane alignment in all cell division events. Some interesting topological details of this system can be seen, but the discussion of this phenomenon is left for later, see Chapter 6. Right: The result of consistent division plane alignment. The spiral pattern is due to a slight increase in division plane angle with respect to the horizontal form generation to generation. The straight line is a result of no change.

myriad modelling methodologies and software, which include molecular dynamics (see Chapter 2). A complete description of this topic is out of the scope of this thesis. We will instead focus on providing a summary of some methods used to study the growth and mechanics (in which we include migration) of cellular tissues, and the connection between them.

Many of the models discussed here, especially the agent based models, can be applied to that approximation of cells. We shall consider two types of models:

1. Mathematical models

In this branch of cell models differential equations are derived, or stipulated, from other laws of physics that aim to link the properties of the cells to their environment. These kinds of methods are discussed in Section 3.5. Mathematical models can be computationally cheaper to solve than agent based models, but they also may require a larger number of simplifying assumptions to be able to solve them

2. Discrete cell models

This branch contains models where cells are modelled as individual bodies with certain interactions defined between them. A range of

methodologies have been proposed in this field and are discussed in Refs. [223, 224]. Some of discrete models are discussed in Section 3.6. These kinds of models may simulate many thousands or tens of thousands of cells in 2D and 3D, making them more computationally expensive. Nevertheless, they provide a far higher resolution compared to purely mathematical models.

This non-comprehensive summary of the models in the literature will give readers context and motivate the need for a new model in this field. More detailed reviews of cell models are available in Refs. [223, 224].

3.5 Mathematical Models

In general, mathematical models have been developed to study many cellular phenomena such as: cell-cycle control, cell death, cell differentiation, cell aging and renewal [225–227]. Sub-cellular phenomena have also been studied with these methods, including DNA control (Transcription, Replication, Repair), or endocytosis[228]. Readers interested to learn more of this field are referred to Refs. [229, 230].

3.5.1 Models of Cell Population Dynamics

The measurement of cell population trends and comparing between different types of cells, or the same species of cells exposed to different environments, has traditionally been a vibrant field of study in biology. Tracking the progression of cell population over time is a relatively straightforward experimental measurement, while still being a relevant marker of cell health [11, 231, 232]. For example, the dose-effect curve, which shows the number of cells surviving after a dose of some drug, is a classical measurement of toxicity, or effectiveness of treatments [233–235]. The trends in the number of cells in a culture over time can easily be observed by monitoring colony size through a microscope [236–238]. The population curve can also differ greatly within the same species depending on what stage of life that organism is in (development, reproduction, death, etc.).

In idealized systems where there is no hindrance to growth, some fraction (up to 100%) of cells can divide, so the growth rate is given by

$$\frac{dN(t)}{dt} = rN(t) \quad (3.1)$$

Where N is the population at some moment in time, and r is fraction of cells that will divide. This has a simple solution given by

$$N(t) = N_0 e^{rt} \quad (3.2)$$

where $N_0 = N(t=0)$ is the initial number of cells. This growth is named intrinsic growth [239, 240]. It assumes no competition between cells for growth, hence the constant growth rate r . However, this is never possible in real systems since as there are multiple factors hindering growth such as competition with other cells for nutrients, the limited lifetime of cells with an associated death rate, the threat of disease and/or predators. Normally, one would observe sigmoidal growth in the system [232, 241, 242]. Typically, growth starts at a small population, increases to a maximum set by the carrying capacity of the medium, and finally decays to zero once all of the nutrients in the system have been consumed. One can define a generalized logistic function that is fitted to population trends as

$$N(t) = \frac{N_0}{(1 + Qe^{-rt})^{\frac{1}{v}}} \quad (3.3)$$

where $v > 0$ is a constant (most of the time $v \approx 1$), r is the growth rate and $Q = \left(\frac{N_{\max}}{N_0}\right)^v$ is the carrying capacity of the system, and $N_0 = N(t=0)$. Note that the growth rate here accounts for both cell division and death. Some other functions have also been suggested for understanding growth [232, 242–244] such as the simplified logistic function given by

$$N(t) = \frac{N_{\max}}{1 + e^{-r(t-t_0)}}, \quad (3.4)$$

where N_{\max} is the maximum number of cells that can be supported by the system, r is the growth rate, and t_0 is the time corresponding to $N = \frac{1}{2}N_{\max}$, or the Gompertz function [232, 244] defined as

$$N(t) = N_{\max}e^{-be^{-rt}} \quad (3.5)$$

where b is just a shift on the time axis depending on where the $t = 0$ is placed. There have been considerable studies on these functions and their use in the fields of modelling growth [230, 232, 242, 243], it will be sufficient for our purposes to take them as given, without justification as to *why* such functions are good ways to estimate growth. There has been quite some effort in linking the different terms of these logistic functions, to biological factors. Good examples are the work by Schnute *et al.* [232] and Zwietering *et al.* [242].

3.5.2 Continuum Models of Cell Behaviour

While analyzing the population trends of cells is a viable method for understanding cell behaviour, the functions described in the previous section do not account for spatial variations or quantify the mechanical forces within cells. The methods mentioned here are able to study the mechanical parts of cell behaviour, both as single cells or collections of cells, and the interactions between them. These mathematical models that abstract microscopic interactions between cells into functions which may describe parameters such as density, growth rate, death rate, intercellular interaction strength [245], or interaction strength with the medium [246].

For tissues of cells, functions that depend on both space and time are derived that describe the dynamics of a continuum of cells [223, 230, 247, 248]. This method yields the dynamics of the total population as whole and individual behaviour averaged out. Continuum models have been used to study a variety of phenomena such as tissue deformability [249], tumour growth [230, 250], viscosity of tissues [245], and anisotropic tissue growth [251]. The dynamics of individual cells are studied as well such as the work by Sens *et al.* [252, 253], where they define functions between cell membranes and other cells as well as objects in the cells' environment. The work of Banerjee *et al.* [254] is an example of mathematical modelling to study cell migration. Recently Palmieri *et al.* [255] devised a model which is the continuum limit of the Cellular Potts Model (discussed in Section 3.6.1). In their work, Palmieri *et al.* devised a method which determines cell shape dynamics from changes in free energy that depends on the elastic response of cells to deformation, preferred radius of each cell, and penalty for cell overlap. Their model also accounts for each cell's velocity. Palmieri *et al.* were able to reproduce spontaneous mi-

gration of anomalous cancer cells in a monolayer of healthy cells [255]. Unfortunately, cell repulsion is not taken into account which plays a vital role in cellular phenomena [256–258], and the phase-field description of cellular interaction and structure limit the granularity with which cellular interfaces can be studied.

3.6 Discrete Cell Models

Discrete Cell Models (DCMs) implement cells as individual bodies that can interact with their environments or other cells. These models aim to simulate the physical properties of different cells and to see how they affect their behaviour. These models are generally more computationally expensive [223], however they allow us to study of cell behaviour at a higher resolution, and to tune the mechanical properties of cells with greater granularity.

Most of the models discussed here approximate the structure of the *mechanical* cell as either collection of lattice points, such as in the Cellular Potts Model (CPM) (Section 3.6.1), or as polygonal structures with edges and faces that interact with each other, such as Delaunay Object Dynamics(Section 3.6.4). There are also a few methods that approximate cells elastic surfaces (Section 3.6.5).

3.6.1 The Cellular Potts Model

The Cellular Potts Model (CPM) is a lattice based model that can be used to understand the factors at the cellular scale that affect tissue organization [259–262]. It is a generalization of the Ising model[263] where instead of considering two possible states, such as for example atomic spin states -1 and +1, the Potts model considers any number of states. See the review by Wu[264] for a more detailed description of the Potts model. Graner and Glazier first studied cell sorting by extending the Potts model to study cells [261, 262], but it has since been used other different phenomena such as cell migration [265], and morphogenesis [266]; the differentiation of embryonic stem cells into different types of tissue and ultimately organs.

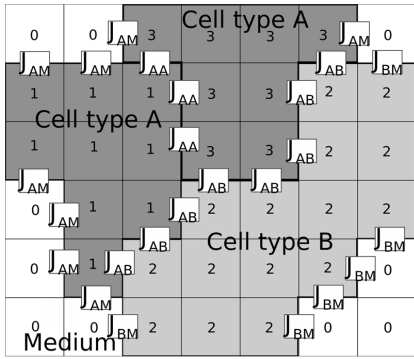


Figure 3.9: Figure showing a Cellular Potts Model (CPM) model set up. The cells have indices 1,2,3 and the medium is with index 0. Each cell is defined by domains of the same index. There are three interaction terms: J_{AM} which is for the interaction between cell type A and the medium, J_{AB} which is for the interaction between the A cells and B cells, J_{AA} between the cells of the A type, and J_{BM} for the interaction between B and the medium. Taken from [260], CC license.

Each cell is defined by a collection of lattice sites with different spins, as shown in Figure 3.9. In CPM, there are as many spins as cells. Three are shown in the figure, but there is no limit, spin 0 is reserved for the medium. The energy of, say, the state shown in Figure 3.9 is given by

$$H = E_{\text{adh}} + E_{\text{vol}} + E_{\text{chem}}, \quad (3.6)$$

where E_{adh} is the energy due to the interaction of different cells, E_{vol} is an energy associated with the area of each cell (representing the energy required to deform a cell from its equilibrium site), and E_{chem} approximates the response of the cells to an external chemical gradient.

Let (i, j) be the index of each lattice site in 2D and c be the index of each cell. Let $\theta(i, j)$ return the type of the cell containing lattice site (i, j) . In Figure 3.9 there are three cells, two of which are of type A. The adhesion term, then, is defined as

$$E_{\text{adh}} = \sum_{(i, j), (i', j') \text{neighbours}} J_{\theta((i, j)), \theta(i', j')} (1 - \delta_{\theta(i, j), \theta(i', j')}) \quad (3.7)$$

in which the sum is taken over all lattice sites that neighbour each other, $J_{\theta(i, j), \theta(i', j')}$ is an energy term (J_{AB} , J_{AM} , J_{AA} in Figure 3.9) that simply quantifies the strength of the interaction between cell A and B; $\delta_{\theta(i, j), \theta(i', j')}$ is the Kronecker delta that switches the interaction term on or off. E_{adh}

simply determines if an intercellular or cell-medium interaction is favourable or neutral.

The second term in Equation 3.6, E_{vol} , represents the energy required to deform a cell by changing its volume. It is defined as

$$E_{\text{vol}} = \sum_c \frac{1}{2} \kappa (\nu_c - \nu_{c,0})^2 \quad (3.8)$$

where κ^{-1} is the compressibility of cell c , and ν_c its the instantaneous volume (number of sites with the same index of the cell) and $\nu_{c,0}$ is its cell volume at equilibrium with the medium.

The last term in Equation 3.6, accounts for the cells reaction to external fields, such as chemical gradients. It is defined as

$$E_{\text{chem}} = \sum_c -\mu_c \mathbf{n}_c \cdot \mathbf{r}_c, \quad (3.9)$$

where μ_c is the strength with which the cell reacts to the external field, \mathbf{n}_c is its polarization vector, and \mathbf{r}_c is its centre of mass.

The dynamics of the system is then calculated with Metropolis Monte Carlo Steps (MMCS) scheme [267]. In each MMCS, the state of the system is changed randomly by changing the spin of each lattice site randomly and calculating the energy of the new state with Equation 3.6 and accepting or rejecting a new state with a probability given by

$$P(\Delta E) = \begin{cases} 1 & \text{if } \Delta E \leq 0 \\ e^{-\frac{\Delta E}{T}} & \text{if } \Delta E > 0 \end{cases} \quad (3.10)$$

where T approximates the effective cytoskeletal fluctuation amplitude of cells in units of energy [266] (not a temperature). This single quantity describes how dynamic the cell is.

The CPM model can be used to study cell migration [265], and sorting and tissue organization [260, 261]. It has also been extended to study growth [259] by altering Equation 3.8 to induce increase in cell volume. Additionally, CPM has been used successfully to study packing topologies [268], cell sorting [269] and embryonic development [270], collective migration [265, 271], and tumour growth [272].

While this method has been used to study a lot of different types of cell behaviours [273, 274], it clearly lacks the ability to accurately describe

intercellular interactions. The parameters of the CPM Hamiltonian do include terms for the cell polarity, the degree of fluctuations in the cells, however it is not clear how they can be linked directly to the mechanical properties of cells and medium.

3.6.2 Topological Models

This class of models are based on the work of Matella and Fletterick from the 1980s [275–277]. These kinds of models rely on a planar network of trivalent vertices, edges, and faces [278–280]. They are therefore suited to study the emergence of cell coordination in growing epithelial systems. The dynamics of the cells are simulated by manipulating the map structure to introduce cell division, but no growth, division, migration, or death is simulated [277, 281]. Topological models were created to only study the emergence of coordination between cells, i.e. the *topology* of epithelial tissue. However, they ignore all other aspects of cell mechanics. Therefore, topological models cannot be used to study mechanotransduction. An example of the results of a topological simulation and the real tissue it aims to study are shown in Figure 3.10. Figure 3.10(a) shows an experimental measurement of the number of neighbours each cell has (N_n) in an epithelium taken from a fruit fly's wing. Each cell is coloured according to how many neighbours it has. This measurement itself is interesting as the distribution of the number of neighbours is a property of the underlying epithelial tissue. This is discussed in more detail in Section 6.3.2. Now, compare to the results of a topological simulation, also done by Patel *et al.* [281], in Figure 3.10(b). The distribution of N_n is comparable to the real system (see Ref. [281] for details), however all other information about the shape of the cells is lost.

Topological models may be useful in the study of the number of neighbours of tissues, however they are not adequate for studying mechanotransduction due to the lack of any cell dynamics in the models.

3.6.3 Vertex Models

In vertex models (VM) each cell is represented geometrically by a polygon, where the perimeter of a polygon represents the cell membrane [282–

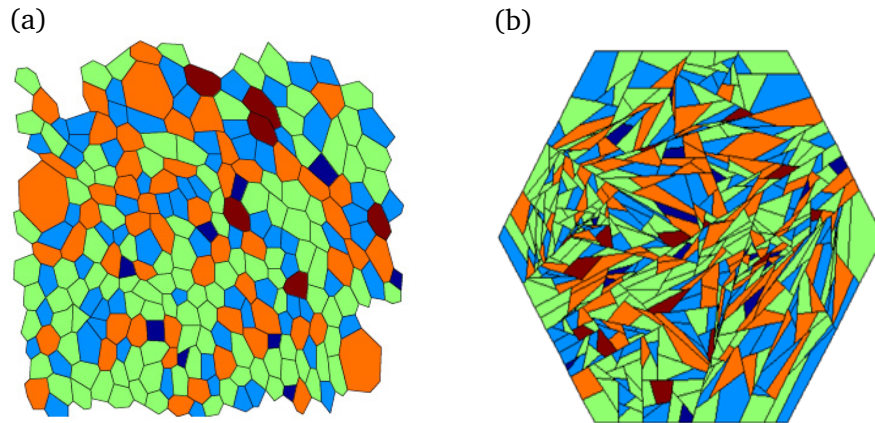


Figure 3.10: Tissue topology measured with a topological model by Patel et al. [281]. (a) Real epithelial tissue taken from a *Drosophila* (fruit fly) wing. (b) Topological model showing the tissue after 9 generations of growth. Colours represent number of neighbours (N_n): darkblue=4, blue=5, green=6, orange=7, maroon=8. Images taken from Ref. [281], CC license.

[284]. Topological models were traditionally used to study inorganic systems such as soap bubbles [285], foams [286], and crystal grain boundaries [287]. Their use for deformations of epithelial systems was first demonstrated in [288], and they have been used to study epithelial systems since. Detailed discussions of VM methodology and application are given in Refs. [284, 289].

In VMs, each cell is represented as a polygon, with vertices and edges shared between adjacent cells. Each polygon represents a 2D cross-section of a real epithelial cell. This simplification makes VMs inexpensive to represent computationally. The motion of the vertices is governed rules based on the location of each vertex, its connection to other vertices, and geometrical features of the neighbouring cells, such as surface area or volume. The rules themselves vary [284] and can be tuned according to the biological problem of interest. New cells are created in the same way as in topological models, by adding a new pair of vertices, with positions drawn from a uniform distribution [284], or along the shortest axis through the centre of the cell [290]. An example of cell division simulated in this manner is shown in Figure 3.11.

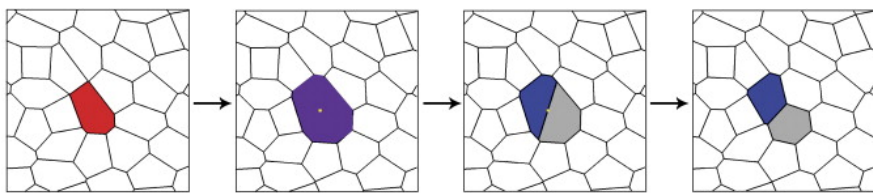


Figure 3.11: Progressions showing the addition of new cells to simulate cell growth. A viable candidate for division is chosen and divided to add a new cell to the system. This scheme is used in both topological and vertex models, though the rules themselves can vary between the two methodologies. Image taken from Ref. [283] with permission from Cell Press.

VMs have been used to show the impact of cell mechanics, growth rate, and mechanics on epithelial packing[283, 291]. Since the formulation of VMs is 2D, it cannot be used to study 3D tissues. There are some variations of VMs [289] that are 3D, though they are still meant to study epithelial systems as a surface in 3D with a thickness. It also lacks the proper treatment of dynamic cell membranes. The structure of the cells VMs inherently assumes closely packed cells, so it cannot be used to individual cells, or the dynamics of how tissue packing changes. Lastly, VMs also neglect any intermembrane dynamics as membranes are not simulated explicitly and neighbouring cell membranes are assumed to be in constant close contact.

3.6.4 Triangulation or Tessellation Based Models

Unlike CPM or vertex models, this class of modes represents cells by a points in continuous space and a Voronoi Tessellation around them defining their border, or a Delaunay triangulation defining their interactions with neighbouring cell. There are a few such models available in the literature, such as Delaunay Object Dynamics (DOD) and other models developed by Radszuweit *et al.* [292] using the same methodology.

Delaunay Object Dynamics (DOD) is a three dimensional technique where each cell is modelled as a three dimensional, elastic, and adhesive Voronoi cells [247, 293–295]. Each cell is described as a three dimensional polygon that is constructed with Delaunay triangulation. Readers

interested in the details of Delaunay triangulation are referred to [293, 296, 297]. Each face and edge of each cell is then modelled with damped Newtonian Mechanics [293]. The Delaunay triangulation used in this method is slightly varied from regular Delaunay triangulation and is termed weighted Delaunay triangulation [295, 298]. To put it simply, Delaunay triangulation is a method of triangulating a set of such that it obeys the Delaunay Condition [293] which states that the circle circumscribing any triangulation must not contain any other points. DOD is constrained by the triangulation algorithm that is used as it is difficult to triangulate irregular polygons, which cells can. Another tessellation based method is the one proposed by Radszuweit *et al.* in Ref. [292]. There, cells are described based on the Voronoi tessellation of points that represent their centres. This method is similar to DOD in that it uses the tessellation of random points on a square grid to represent cells. Then, the dynamics of cell growth are modelled by stochastic processes that add new points over successive generations.

Tessellation based models assume, as in the VMs discussed in the previous section, that cells are always closely packed in 2D or 3D. Thus, they do not include inter membrane dynamics or a method to analyze the forces generated between cell membranes. Furthermore, there are no available software implementations of DOD, or the model due to Radszueweit *et al.*.

3.6.5 The Cellular Discrete Element Model (CeDEM)

This model aims to approximate cells with the techniques of molecular dynamics (MD) in 2D. CeDEM is based on another model first designed by Karttunen and Åström in Ref. [299], to study aggregation and jamming of soft particles in confined spaces. Later, in 2014, Mkrtchyan, Åström, and Karttunen expanded upon the model by adding modes of cell growth and division[43, 300]. With it, they were able to accurately reproduce the coordination of epithelial tissues. This 2D system is generalized to 3D with *CellSim3D*. Details regarding the new force field and simulator are given in Chapter 5. Readers are advised to see Ref. [43] for a detailed description of CeDEM. What follows in this section is a summary.

Each cell is approximated by a closed loop of nodes, as shown in Figure 3.12, that interact with each other through a force field that contains terms for intracellular interactions, intercellular interactions between neigh-

bouring cells, and the growth of cells with a pressure force. Cells in that are growing are known to regulate their pressure before division [189, 190].

The forces acting on node i in some cell are governed by

$$m\ddot{\mathbf{r}} = \mathbf{F}_i^{\text{cell}} + \sum_j \mathbf{F}_{ij}^{\text{rep}} + \sum_j \mathbf{F}_{ij}^{\text{adh}} + \sum_j \mathbf{F}_{ij}^{\text{fric}} - c\mathbf{v}_i, \quad (3.11)$$

where $\mathbf{F}_i^{\text{cell}}$ contains terms for the cell's contractility, structure, and growth (the intracellular term), $\mathbf{F}_{ij}^{\text{rep}}$ and $\sum_j \mathbf{F}_{ij}^{\text{adh}}$ contain terms that define intercellular adhesion and repulsion respectively summed over all nodes j belonging to other cells within range, $\sum_j \mathbf{F}_{ij}^{\text{fric}}$ is the intercellular friction term summed over all cells within range, and finally $-c\mathbf{v}_i$ is friction due to the medium, which is assumed to be a simple fluid.

The intracellular forces approximate the mechanical properties of cells with a two dimensional coarse-grained structure, shown in Figure 3.12. Each cell consists of 76 nodes, and each pair of bonded nodes interact with spring force, which is balanced by an outward pressure force, (Pl). Each node is bonded to two neighbour nodes, and experiences a force given by

$$\mathbf{F}^{\text{cell}} = \sigma_1 \hat{\eta}_1 - \sigma_2 \hat{\eta}_2 + \frac{Pl}{2} (\hat{v}_1 + \hat{v}_2), \quad (3.12)$$

where $\hat{\eta}$ denotes the bond vector between two connected nodes, and \hat{v} is a vector normal to the bond (the $\hat{\cdot}$ denotes a normalized vector), σ is the magnitude of the bond force and (Pl) is the magnitude of the pressure force. The subscripts indicate which bond the value pertains to. Each bond is assumed to be a spring with the magnitude of the bond force being given by $\sigma = -K^{\text{spr}}(l - l_0)$ where l and l_0 are the instantaneous and equilibrium bond lengths respectively.

The magnitude of the pressure force is an increasing value from (Pl)_{init} at a rate of $\Delta(Pl)$ every time step; both are parameters in the input to the simulations.

Neighbouring cells can interact through a variety of molecules named Cell Adhesion Molecules (CAMs), discussed in Section 3.2.1. This interaction is approximated by the adhesive and repulsive terms in the CeDEM force field. Nodes of different cells experience repulsion (Equation 3.14), adhesion (Equation 3.13), and intercellular friction (Equation 3.15).

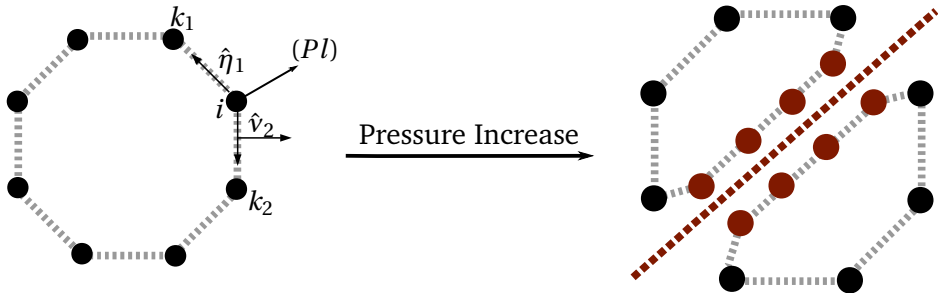


Figure 3.12: Schematic showing a summary of the two dimensional Cellular Discrete Element Model (CeDEM) [43]. Each cell is a closed loop of interacting particles as shown on the left hand side. The right hand side shows two cells just after division. Growth is induced by an increase in the pressure force. Image recreated from [43] with permission from the Royal Society of Chemistry.

Each node acts as a site for adhesive interaction. All sites are assumed to have the same adhesion strength $K_{ij}^{\text{adh}} = K^{\text{adh}}$. The adhesion force is defined as

$$\mathbf{F}_{ij}^{\text{adh}} = \begin{cases} K^{\text{adh}}(R_c^{\text{adh}} - R_{ij})\hat{\mathbf{R}}_{ij} & \text{if } R_{ij} < R_c^{\text{adh}} \\ 0 & \text{otherwise,} \end{cases} \quad (3.13)$$

and the repulsive term as

$$\mathbf{F}_{ij}^{\text{rep}} = \begin{cases} -K^{\text{rep}}(R_c^{\text{rep}} - R_{ij})\hat{\mathbf{R}}_{ij} & \text{if } R_{ij} < R_c^{\text{rep}} \\ 0 & \text{otherwise.} \end{cases} \quad (3.14)$$

where K^{adh} and K^{rep} are the adhesive and repulsive spring constants; R_c^{adh} and R_c^{rep} are the adhesive and repulsive cutoffs respectively. R_c^{adh} is chosen to be greater than R_c^{rep} .

Intercellular friction between nodes i and j belonging to different cells is defined as

$$\mathbf{F}_{ij}^{\text{fric}} = -\gamma \mathbf{v}_{ij}^{\tau}, \quad (3.15)$$

where γ is the intermembrane friction coefficient and \mathbf{v}_{ij}^{τ} is the component of their relative velocity tangential to the surface of the cell that node i belongs to.

More details about the model, how the simulations are run, and what studies can be carried out through them, are available in Ref. [43]. Since CeDEM is a 2D model, it can only every simulate purely two dimensional systems, such as epithelia (more details in Section 5.3.1) which are sheets of cells interacting laterally. It *can* be altered to study one dimensional (filamentous) tissues that are made of chains of cells, as is done in Chapter 4, but studying cell behaviour in 3D would be impossible. The *Cell-Sim3D* model, described later in this thesis in Chapter 5, arose from the extension of CeDEM into 3D. Its features include all of CeDEM's.

Chapter 4

Morphology of Proliferating Cellular Matter in One and Two Dimensions with CeDEM

Based on: Madhikar, P., Åström, J., Baumeier, B. & Karttunen, M. Morphology of Proliferating Cellular Matter in One and Two Dimensions. Soft Matter, (submitted)

Morphology and dynamics of proliferating cells are among the fundamental issues at different stages of cellular development [280, 301–305]. They are controlled by a number of factors, but from the physical point of view, morphology is tightly coupled to intercellular forces, see e.g., Refs. [305–307]; mechanical forces have been shown to be important in cancer development and it has been suggested that tumour growth may even be arrested by intercellular mechanical forces [308, 309]. Among the many complications in investigating force transmission are that at their embryonic state, cells may not yet have developed junctions and may display more fluid-like behaviour, and that cell-cell adhesion depends on the cell types [306, 310–312]. Junctions are crucial in cell-to-cell stress transmission [306, 307, 313, 314] but it is, however, challenging to probe the individual junctions experimentally.

From a coarse-grained point of view, that is, ignoring chemical details and treating cells as elastic objects, cellular systems can be seen as disperse soft colloidal systems under evolving pressure applied non-

uniformly throughout the system. Several studies have tried to capture aspects of growing soft colloidal systems (e.g. for modelling tissue growth) at different levels [299, 315–317] but even in simple systems many fundamental questions remain open including the precise nature of colloidal phase diagrams when colloids are soft with size dispersity [318], and structure selection via self-assembly [319]. Cellular systems are more complex since they exhibit additional behaviours such as cell growth and division, they have varying mechanical properties (e.g. elasticity and cell-cell adhesion) and their response to external stimulus may be sensitive to the local environment.

Dimensionality has an important role in particular in regulation of intra- and intercellular forces at different levels, see e.g. Refs. [320–324]. Some systems, such as epithelial tissues and *Drosophila* wing discs, are inherently two dimensional which gives them distinct morphological properties due to the nature of cellular packing, and the transmission of, or response to, forces [280, 312, 325]. In addition, jamming can be very strong in two dimensional systems, varying stiffness and intermembrane friction are a step towards investigating jamming in cellular systems [326, 327]. Our main focus is on the above effects in systems consisting of hard cells in a soft matrix and vice versa. Besides being important in understanding the mechanisms of cell movement under pressure [307], such situations have been proposed to be important in tumour growth [308, 309] – cancer cells are often softer than healthy cells [255, 328] although the opposite has also been reported [329, 330]. Cell stiffness, its measurements and connection to cancer metastasis have been recently reviewed by Luo *et al.* [331].

One of the intriguing questions in cell division is: Why do cells exhibit diverse morphologies upon division and growth? In addition to uniform structures, a plethora of structures with various mechanisms and division modes have been suggested but the issue remains largely unresolved [278, 312, 332, 333]. To illustrate how different morphologies can arise, consider cyanobacteria. Figures 4.1(a)-(c) show *A. circinalis* and Fig. 4.1(d) *A. flos-aquae*. Both of them can be approximated as quasi one-dimensional structures. In contrast to most other cells, however, cyanobacteria have continuous outer membranes shared by the whole filament consisting of multiple cells [333, 334]. The inner membranes, however, belong to in-

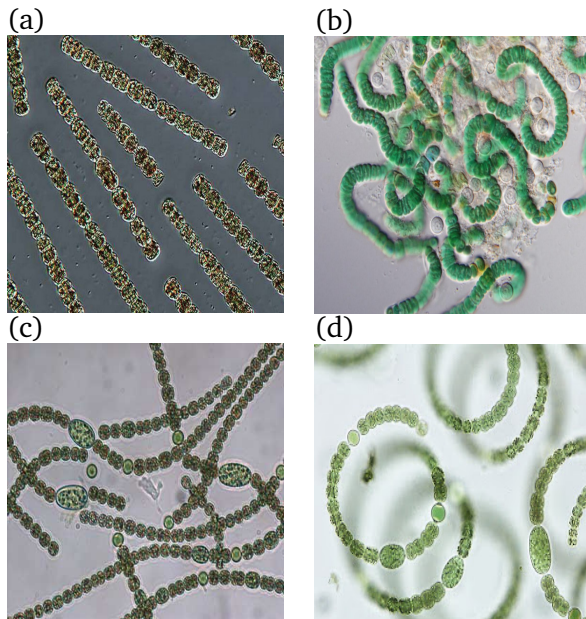


Figure 4.1: (a) *A. planctonica*. Image with permission from the Laboratory of Phytoplankton Ecology [335]. (b) *A. laxa*. Image with permission from the A. Braun Culture Collection of Autotrophic Organisms [336]. (c) *A. circinalis*. Image with permission from the Kudela Lab, University of California Santa Cruz [337]. (d) *A. flos-aquae*. Image with permission from Demarteau/Aquon [338].

dividual bacteria only. It has been suggested that this together with specialized junctions leads to filamentous structures (there are also subtleties related to, e.g., size selection of the filaments) [333, 334].

Previously [43], the orientation of the division line was selected randomly. The simplest way to model cyanobacteria morphologies is to choose the orientation of the division plane in such a way that it is approximately parallel between neighbouring cells. Although an approximation, this approach should be able to produce similar morphologies.

Two dimensional cellular systems can be studied with a number of computational methods (summarized in Section 3.6) including off-lattice vertex models [198, 278, 279, 281–284, 291, 339], and Voronoi Tessellation or Delaunay triangulation based models [247, 292, 294, 340, 341]. Since these models approximate cell membranes as edges or planes,

they are not able to describe intermembrane interactions with high accuracy and it is not possible to calculate intercellular forces. The immersed boundary method of Rejniak *et al.* [188, 342] explicitly models intermembrane interactions and may be suited to such problems, however it is not clear if this method can be used on large systems of cells. There are on lattice methods as well such as the Cellular Potts Model (CPM) [259, 261, 262, 270, 272] where interactions between lattice sites represented different cell types and are mediated through various energy functionals, which can be linked [255, 343] to phase field models. CPM models cellular interactions with scalar energy terms, making it impossible to study forces between cells. In summary, these models for two dimensional systems, while suited to the problems that they were designed for, are difficult to use to study interactions between cells that are mechanically distinct.

One dimensional systems have gained lesser attention and the models are typically of reaction-diffusion type with fixed geometry and size as discussed extensively in the review by Herrero *et al.* [333].

The two dimensional Cellular Discrete Element Model (CeDEM), summarized in Section 3.6.5, with more detail in Ref. [43], is able to address the issues described above. It can be used for both one dimensional and two dimensional systems, with tighter control on the mechanical properties of each individual cell. It is extended to three dimensions with the *CellSim3D* model, discussed in Chapters 5 and 6, and in Ref. [42]

4.1 Model and methods

We employ the two-dimensional CeDEM to investigate tissue morphologies in one and two dimensions. Full details and derivation of the model are provided in Ref. [43] but to summarize, in CeDEM the cell membrane is discretized as beads connected by bonds of stiffness K_i^{spr} .

Cellular growth is controlled by a growth pressure and division by a threshold in cell area (above which cells divide) and the orientation of the cell division line. Importantly, CeDEM allows the topology (the polygonal distribution) to vary spontaneously [43].

Here, we extend CeDEM for simulations of different cell types using three simple approaches:

1. changing the cell division line orientation,

2. changing cell stiffness, and, finally,
3. changing the friction between cell membranes; in CeDEM cell membrane and cytoskeleton are treated as a coarse-grained single object.

Until now, the orientation of the division line of each cell was chosen randomly and it was constrained to pass through the centre of mass of the cell undergoing division. This results in tissue growth such that it fills the available space roughly uniformly [43]. Modification 1) above allows for simulations of cyanobacteria-like structures shown in Fig. 4.1.

Modification 2) allows for simulations of different types of cells. As mentioned above, cancer cells are typically considered to be softer than the matrix cells. Softness, or higher malleability, is typically associated with the invasiveness of cancer cells [331]. This has recently been challenged by Nguyen [330] *et al.* who measured Young's modulus of pancreatic cancer cells using different cell lines and found the stiffer (than the matrix cells) cells to be more invasive than the softer cancer cells. Whether this is purely mechanical or due to simultaneously occurring biological processes remains unclear. What matters for our purposes is that there are two, or more, types of cells of different stiffness. Here, we use two types: 1) *Type1*, stiff cells with a low growth potential with stiffness $K_1^{\text{spr}} = 4 \mu\text{N}/\mu\text{m}$. The low growth potential means that the cell membrane is so stiff that the applied pressure is barely enough to grow the cell to a size above the division threshold. Therefore, if the cell is even lightly squeezed between other cells it will not divide before force equilibrium is reached and growth stops. 2) *Type2*, soft cells with a high growth potential with stiffness $K_2^{\text{spr}} = 1 \mu\text{N}/\mu\text{m}$. These cells have a high growth potential which means that cell membrane stiffness is so low that the cell area easily grows beyond the division size. The cells are identical in all other ways except their stiffness.

Finally, modification 3) allows for comparisons of systems of cells with different intermembrane friction coefficients. Cell-cell friction and its importance in mechanotransduction has recently been reviewed by Angelini *et al.* [344]. Intermembrane friction is modelled as

$$\mathbf{F}_i^{\text{ext}} = -\gamma \mathbf{v}_{ij},$$

where γ is the friction coefficient and \mathbf{v}_{ij} is the component of the relative velocity between two membranes tangential to the cell that bead i belongs

Parameter	Notation	Sim. Units	SI Units
Nodes per cell	N	76	-
Node Mass	M	0.1	0.1 pg
Medium viscosity	c	1	1000 Pas
bond length	l_0	0.1	1 μm
Bond Stiffness	K^{spr}	100, 400	1, 4 $\mu\text{N}/\mu\text{m}$
Adhesion stiffness	K^{adh}	56	0.56 $\mu\text{N}/\mu\text{m}$
Intercellular friction	γ	0, 20	0, 200 $\mu\text{g}/\text{s}$
Division Area	A^{div}	1	100 μm^2
Starting Pressure	$(Pl)_{\text{init}}$	15	1.5 nN/ μm^2
Pressure increase	$\Delta(Pl)$	5×10^{-5}	5×10^{-6} nN/ μm^2
Repulsion cutoff	R_c^{rep}	0.1	1 μm
Adhesion cutoff	R_c^{adh}	0.2	2 μm
Time step	Δt	1×10^{-4}	*
Division checkpoints	T^{div}	0.2	*

* Scaled to produce tissue comparable to *Drosophila* (fruit fly) wing disc; such that simulation time of 5 corresponds to approximately 10 hours.

Table 4.1: Values of the parameters used in the simulations for this chapter. These values determine the mechanical properties of the cells and their environment. Notation and units taken from Ref. [43].

to. We compare systems where $\gamma = 0.0 \mu\text{g}/\text{s}$, that is, cells do not interact very much with their neighbours, and strongly interacting cells with $\gamma = 200.0 \mu\text{g}/\text{s}$.

The parameters used in the CeDEM simulations for this chapter are shown in Table 4.1

4.2 Results

4.2.1 Quasi-one-dimensional morphology

We start from (quasi-) one-dimensional systems and compare the structures from experimental systems (Figure 4.1) and simulations (Figure 4.2). First, instead of just dividing all cells that are above some threshold area, we allow a single cell to divide only once. Thus, only the youngest cells are allowed to divide similar to budding growth in bacteria [345]. Addition-

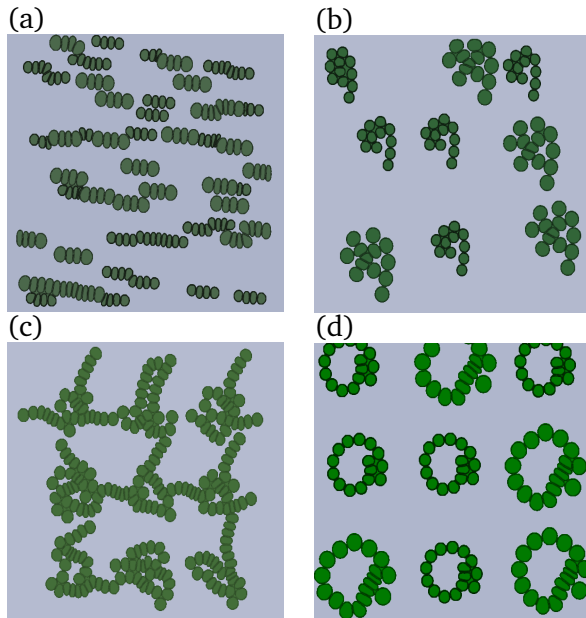


Figure 4.2: The type of cell can be changed by changing the division plane choosing rules. (a) Division planes parallel at each generation, (b) division plane turning left at an increasing rate, (c) small clusters of original cells dividing at perpendicular and constant orientation angles, and (d) division plane turning left at constant rate.

ally, we make the division plane non-random. Different scenarios lead to morphologies as shown in Figure 4.2: Keeping the division plane parallel for each generation leads to morphologies similar to *A. plantonica* (compare Figures 4.1(a) and 4.2(b)). Letting the division line rotate slightly more by every generation produces Figure 4.2(b). Allowing all cells to divide and letting them divide along two perpendicular lines produces Figure 4.2(c), approximating the morphology of *A. laxa* in Figure 4.1(b). Finally, constant rotation every generation leads to Figure 4.2(d), which is structurally similar to Figures 4.1(b) and 4.1(d).

Although the morphologies in Figure 4.2 are created by the simple rules as discussed above, and there may well be other rules that lead to similar morphologies, it is important to keep in mind that to arrive to such structures real systems have molecular mechanisms that lead to the emergence of such structures. The microscopic molecular level mechanisms are

effectively manifested as rules at the macroscopic level. The exact mechanisms as why filamentous shapes form remain to be resolved, but current evidence shows that septal junctions have an important role [333, 346].

4.2.2 Soft and stiff cells in 2D

We now focus on two-dimensional larger and denser samples of cells with two cell types, stiff (*Type1*) and soft (*Type2*), in the same system. We assume that softer cells are tumour cells. This assumption is based on the fact that cancer cells tend to be softer [255, 328]. The initial setups for simulations of such systems were created with equal proportions of *Type1* (red) and *Type2* (blue) cells, see Figure 4.3(a). Growth is simulated with identical parameters for all cells, except membrane stiffness, until confluence. Figure 4.3(b) shows the tissue structure at the end of the simulation with the system mostly filled with soft cells (blue) while the stiff cells (red) are compressed into dendrite-like structures. Another distinct feature is that the cells interpenetrate in the regions marked with light purple in Figure 4.3(b). This type of behaviour occurs in diverse systems as shown by Eisenhoffer *et al.* for canine, human and zebrafish epithelial cells [347] and discussed at length in the review by Guillot and Lecuit [312] (see in particular Figure 2 in Ref. [312]). The forces can become so high that the cell membranes practically intersect each other. These cells would be good candidates for cell death. Experiments have also suggested that for live cells, such conditions may lead to pathologies [347]. CeDEM does not currently support cell death in terms of cells disintegrating and disappearing from the system. Cells do, however, get squeezed into very small space and division ceases in the purple regions of Figure 4.3(b).

Figure 4.3(c) shows a smoothed histogram of the average intermembrane (or contact) forces between cells. The white dots show the centres of masses of the stiff cells. The peaks in the contact force distribution correlate highly with the locations of the stiff cells indicating that *Type2* cells overwhelm *Type1* cells as the tissue grows and also that the system imposes higher stresses on the stiff collapsed cells.

At this point, we ask the question if this collapse of stiff cells can be mitigated by making their interactions stronger. This can be examined by changing the magnitude of intermembrane friction γ . Since cells need to find space to grow, they need to slide past each other into empty regions.

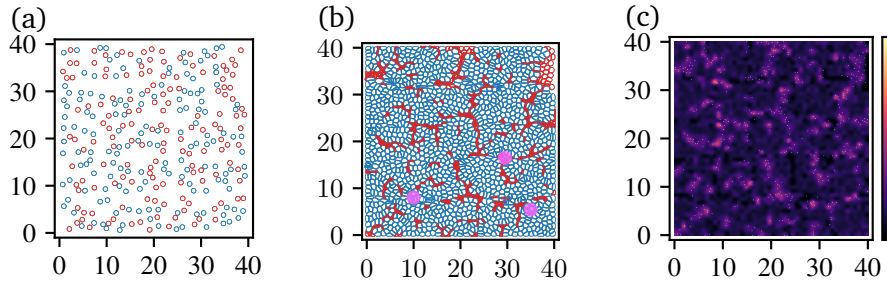


Figure 4.3: *X* and *Y* axis represent spatial coordinates in 2D in units of 10 μm . (a) Initial configuration. Stiff cells are depicted in red, and soft in blue. Growth is simulated from this state until confluence. (b) A confluent tissue soft and stiff cells. Stiff cells form dendrite or vein-like structures in a matrix of soft cells. The regions marked with light purple are areas where cells interpenetrate and cell death could occur — though death is not simulated by CeDEM. (c) Contact force distribution in the same tissue (color bar ranges from 0 to 150 nN). Large contact forces are located at stiff cells and at boundaries between soft and stiff cells. White markers are the centres of masses of the stiff cells.

In other words, higher friction induces jamming between the cells which means that they easily get squeezed between each other and therefore reaching the division threshold area takes a much longer time. The softer cells will also need to counteract this effect to grow. Figure 4.4 shows a similar simulation setup as before, except with different values of γ . Figure 4.4(a) shows the initial conditions, and Figures 4.4(b) and (c) show the final state at $\gamma = 0.0 \mu\text{g/s}$ and $\gamma = 200.0 \mu\text{g/s}$, respectively.

At low intermembrane friction ($\gamma = 0.0 \mu\text{g/s}$), there are more cells at the end of the simulation indicating that growth is faster. The high intermembrane friction system ($\gamma = 200.0 \mu\text{g/s}$) is more porous with slower growth. The friction-less system (Figure 4.4(a)) corresponds to very early stages of development when junctions have not yet developed. The latter system (Figure 4.4(b)) corresponds to when cell adhesion molecules have developed. In both cases, the simulations were run for an interval of time corresponding to 10 division cycles.

To investigate further, we study the sizes of the cells in each case and the forces that are acting on the cells. Figure 4.5 shows the number distributions of cell area (Figure 4.5(a)) and the total force (attractive, repul-

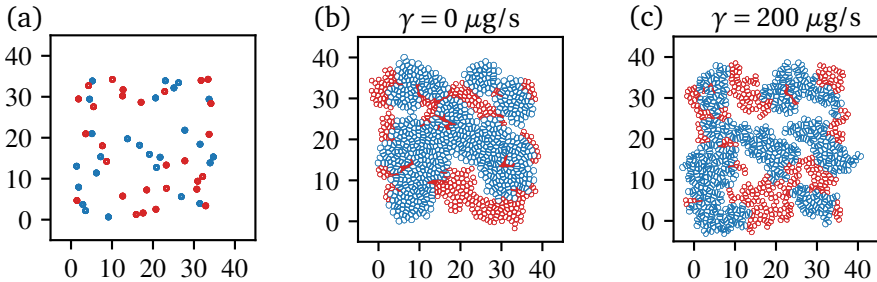


Figure 4.4: *X* and *Y* axis represent spatial coordinates in 2D in units of 10 μm . Morphologies of simulated cells with different intercellular friction.(a) Initial conditions stiff cells are in red and soft cells in blue. The two are in equal proportions.(b) Morphology of zero intercellular friction cells.(c) Tissue with high-friction cells ($\gamma = 200.0 \mu\text{g/s}$). Both cases were simulated for a time corresponding to 10 division cycles.

sive, and friction) that each cell feels due to its neighbours (Figure 4.5(a)). Both distributions display lower total number of cells in the high friction tissue. The peak in area distributions is just below $100 \mu\text{m}^2$, which is due to the threshold division area ($A^{\text{div}} = 100 \mu\text{m}^2$). Some of the cell areas have grown past this limit as cell division occur only at discrete time intervals in CeDEM so some cells are larger. The $\gamma = 0$ distribution shows a small peak at $A \approx 20 \mu\text{m}^2$, which is due to the higher number of collapsed cells in the low friction system. The large-area peak represents the soft-cell majority, and its shape is approximately Gaussian, consistent with the observation from simulations of non-dividing soft colloids [299]. For $\gamma = 200.0 \mu\text{g/s}$ the distribution has not yet developed two peaks and there are some cells that can grow rapidly in the sparse areas of the packing.

Finally, we study the case of a cluster of soft cells surrounded stiff cells in Figure 4.6. We first investigate the case when $\gamma = 0.0 \mu\text{g/s}$. In this case, Type2 cells with the larger growth potential continue to proliferate even when the tissue approaches the state of being space-filling, while Type1 proliferation almost stops. This leads to a tumour-like growth of Type2 cells and compression of Type1 cells at the tumour boundary.

Figure 4.6(a) and (d) show the morphologies for for $\gamma = 0.0 \mu\text{g/s}$ and $\gamma = 200.0 \mu\text{g/s}$ at confluence ¹. The faster growth of the tumour at $\gamma =$

¹Confluence means that the cells fill the simulation box fully.

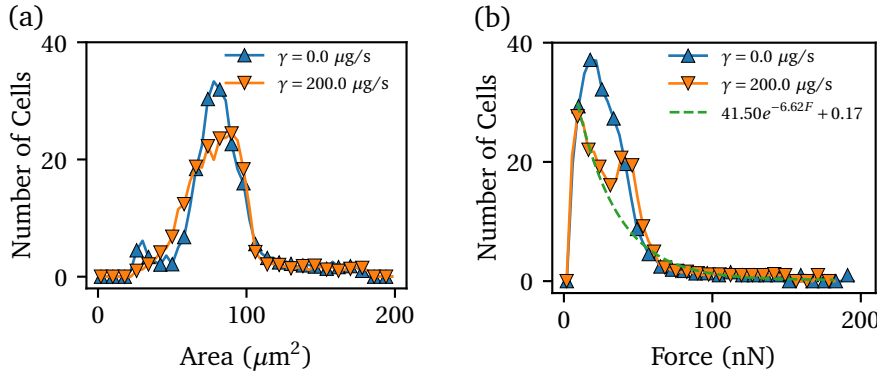


Figure 4.5: a) Number distributions of cell areas. There is a peak at low areas corresponding to collapsed stiff cells. b) Number distribution of intercell forces (denoted by F) at low intermembrane friction ($\gamma = 0.0 \mu\text{g}/\text{s}$), corresponding to Figure 4.4(a), and high intermembrane friction ($\gamma = 200.0 \mu\text{g}/\text{s}$), corresponding to Figure 4.4(b). The green dashed line is an exponential fit to the $\gamma = 200.0 \mu\text{g}/\text{s}$ case, ignoring the second peak.

$0.0 \mu\text{g}/\text{s}$ is clearly visible. Initial conditions for both cases were identical; stiff cells were placed in the centre and stiff cells were placed randomly surrounding them. Figure 4.6(b) and (e) show spatial size distributions in the two cases. The dark regions in the histograms correspond to pores in the system. Cell sizes are roughly equal within the tumour and inside the matrix. Along the tumour boundary, however, the matrix cells are compressed and the tumour cells are enlarged. This effect is seen in both cases but is much more pronounced when $\gamma = 0.0 \mu\text{g}/\text{s}$. Lastly, Figures 4.6 (c) and (f) show the distribution of the mean contact forces. Inside the tumour the contact forces are low, and the largest forces are seen scattered on the tumour boundary. Again this effect is more pronounced in the $\gamma = 0.0 \mu\text{g}/\text{s}$ case.

However, even though there are fewer stressed cells at higher γ , the few cells that are stressed feel higher stresses. This is quantified in Figure 4.7(a) and (b) which show the population distribution over contact force. In both of the current cases we see an exponential tail representing the small population of stressed cells at the tumour boundary. There are more cells that feel higher stress in Figure 4.7(a) with $\gamma = 0.0 \mu\text{g}/\text{s}$, than in Fig. 4.7(b) with $\gamma = 20$. However, these cells feel more stress at higher

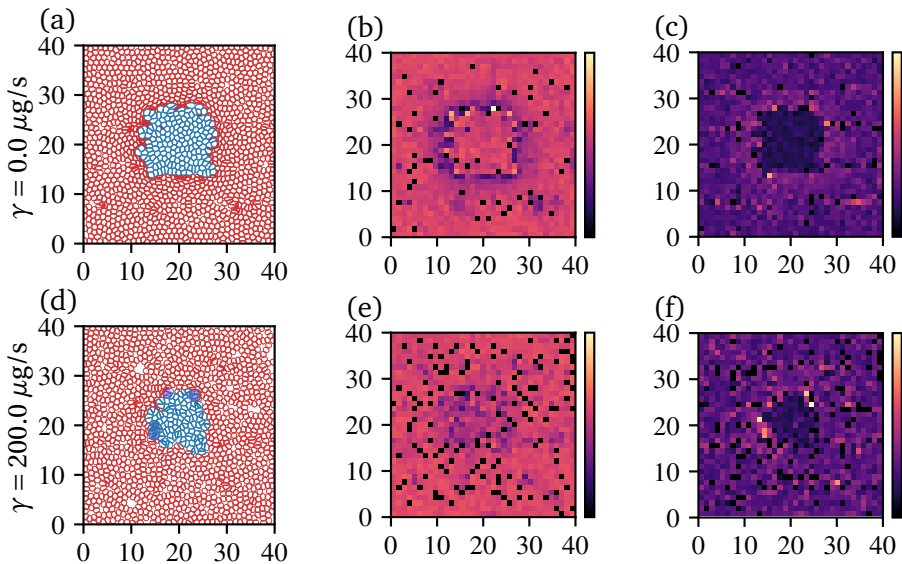


Figure 4.6: X and Y axes represent spatial coordinates in 2D in units of $10 \mu\text{m}$. (a) Inclusion of Type2 (blue) cells in a matrix of Type1 (red) cells, $\gamma = 0.0 \mu\text{gs}^{-1}$; confluent configuration.(d) $\gamma = 200.0 \mu\text{gs}^{-1}$. Configurations for the two cases are at confluence. Purple regions show areas were cells interpenetrate and death could occur.(b) Spatial cell size distribution, $\gamma = 0.0 \mu\text{gs}^{-1}$,(e) $\gamma = 200.0 \mu\text{gs}^{-1}$ (color bars range from 0 to $150 \mu\text{m}^2$). (c) Spatial contact forces distribution $\gamma = 0.0 \mu\text{gs}^{-1}$,(f) $\gamma = 200.0 \mu\text{gs}^{-1}$ (color bars range from 0 to 150nN). Black squares: voids in(b),(c),(e), (f)).

intermembrane friction.

There is only very limited amount of data available for force distributions in proliferating systems. However, they have been measured for soft colloidal systems under compression. It is well established that the distribution has an exponential tail in the vicinity of the jamming transition [299, 348, 349]. It has also been recently shown experimentally by Jose *et al.* by using 3-dimensional packings of soft colloids that the distribution well above the jamming distribution becomes Gaussian [349]. As Figure 4.7 shows, the exponential tail is present in our two-component 2-dimensional cell systems both at zero and high friction. The fact that the cells grow also means that their volumes are not conserved (in contrast to experiments with typical colloids). This is also the case for the cells that are being pushed and compressed by their neighbours as is evident from the snapshots in Figures 4.4 and 4.6. What is clearly different here is the distribution at low forces: the exponential is preceded by a Gaussian distribution. Gaussian peak has been observed in simulations of soft colloids in two dimensions with zero friction [299]. In contrast, in the three dimensional experiments of Jose *et al.* the low force part of the distribution remained almost flat except well above jamming transition. This may have to do with the hardness of the particles: Erikson *et al.* studied materials of different hardness and the force distribution at lower forces depends strongly on hardness [348]. In addition, van Eerd *et al.* have reported faster than exponential decay from their high accuracy Monte Carlo simulations [350] although the deviations can be very hard to detect without high accuracy sampling methods.

Here, peaks in the distribution develop at relatively large forces within the bodies of stiff cells. This becomes particularly evident when a tissue of soft and stiff cells becomes so dense that it approaches space-filling. In this case, almost all stiff cells collapse and form narrow veins or dendrites. With a suitable initial mixture of stiff and soft cells, the soft cells form a matrix with a percolating fractal network of stiff cells which covers only a small fraction of the total area but penetrates almost everywhere (Figure 4.3(b)). This shows a possible pathway for the formation of signalling and transport networks in a simple multi-cellular system.

The results in Figure 4.6 show that the softer cells introduced into matrices of stiffer cells grow faster when intermembrane friction is low;

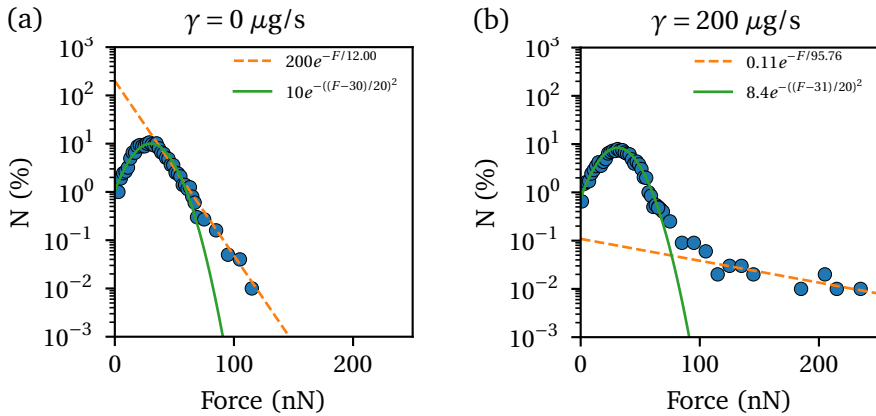


Figure 4.7: Distributions of intercellular forces (denoted by F) when a soft Type2 cell is introduced into a tissue consisting of stiff Type1 cells. (a) $\gamma = 0.0 \mu\text{g/s}$, in the configuration shown in Figure 4.6(a) and (b) $\gamma = 200.0 \mu\text{g/s}$ in the configuration shown in Figure 4.6(d). The distribution of both is similar except the $\gamma = 200.0 \mu\text{g/s}$ case is slightly wider at forces between 0-100 nN and there is a smaller number of cells in (b) that experience high forces. See the text for a detailed discussion and relation to jamming.

weaker cell-cell interactions provide conditions for easier growth. This also suggests that intercellular interactions can be an indicator of how well epithelial tissue can diminish the growth of rogue cells that have a higher growth potential.

4.3 Conclusions

In this work we use the CeDEM model to study how filamentous growing bacteria can create varied quasi-one-dimensional morphologies. We show that modulating the cell division line orientation can be one of the ways such morphologies can arise. What determines the division line orientation is, however, an open question but cell-cell junctions have been indicated having an important role [333]. We propose considering simple division line placement rules as a possible effective manifestation of yet unknown microscopic mechanisms.

We then studied larger, denser systems of cells of two different types in

two dimensions. Cell populations are differentiated by their membrane-/cortex stiffness. We showed that this simple difference is enough, provided internal pressure is identical for both, to favour soft cell growth. Even if a few soft cells are surrounded by stiff cells, it is enough for the softer cell to grow rapidly. This effect can be mitigated by a higher interaction strength between cells. Both of the effects above required some modifications of the CeDEM model presented before in Refs. [43, 299]. We also studied the force distributions which show similarities to non-proliferating soft colloidal systems. Although not studied here in detail, the model allows for tuning the cell-cell friction, an issue raised recently by Vinutha and Sastry for shear jamming [351].

The existing paradigm for the softness of cancer cells has been challenged by Rowat and coworkers who have shown that stiff cancer cells can be more invasive than soft ones [330]. They have also shown that cells experience significant strain hardening. The precise role of it remains to be resolved [352]. Models such as the current one may be helpful in isolating and identifying the purely mechanical processes and their importance for a collection of cells and related them to other soft matter systems.

Chapter 5

The *CellSim3D* Model and Simulator

Based on: Madhikar, P., Åström, J., Westerholm, J. & Karttunen, M. CellSim3D: GPU accelerated software for simulations of cellular growth and division in three dimensions. Computer Physics Communications 232, 206213 (2018).

We explored multiple different models, and their associated software packages, in Section 3.4. As we noted there, those models can be well suited for studying various different cellular phenomena (e.g. cell migration packing topologies). Continuum models (Section 3.5) lack the resolution required to study intra- and intercellular interactions. Discrete cell models (Section 3.6) tend to approximate cell membranes by either straight edges, such as in vertex models [282–284, 339, 353], flat planes such as in Delaunay object dynamics [294, 340, 341, 354], or as a lattice boundaries as in the cellular Potts model [259, 261, 262, 270, 272]. These cannot accurately approximate intermembrane interactions as there are no actual membranes being simulated. Recently, Van Liedekerke *et al.* [355, 356] published a model that is able to simulate cells in 3D with proper terms for intermembrane interactions, but no freely available software that implements the model is available. The immersed boundary method of Rejniak *et al.* [188, 342] explicitly models intermembrane in-

teractions may be suited to such problems, however it is not clear if this method can be used on large systems of cells.

Apart from the problems described above, it is also surprising that despite the fundamental importance of cell division, and the influence of mechanics on it, there are very few software packages available to study it. This is drastically different from fields such as materials and biomaterials research. To the best of our knowledge, there are no freely or commercially available packages comparable to the one presented in this thesis. Current free software packages are mostly based on the cellular Potts model, such as CompuCell3D [357] and CompuCell [358]. There is also the two dimensional Cellular Potts Model Library called Tissue Simulation Toolkit based on the work of Graner and Glazier [261] (available at <https://sourceforge.net/projects/tst/>), and cellGPU by Sussman [353]. Other methods are also available, for example LBICell that uses elastic polygons and the immersed boundary method [181], and the agent-based package CellSys by Hoehme and Drasdo [359] that is available as a free binary executable for non-commercial use. Commercial software includes the so-called Cell Division Program based on the work of Pyshnov [360].

There is not only a need in the field for models that can describe inter-membrane interactions appropriately, with the flexibility required to simulate forces at the subcellular level, but also an efficient implementation into high performing software that can be used by researchers to complete their work faster. We shall discuss a new model, and associated software package, in this chapter, named *CellSim3D* [42], created with the goals of being

- flexible enough to eliminate the issues outlined above
- open source, encouraging improvements and additions, if there are missing features
- amenable to simulating large systems, with up to tens of thousands of cells, on a single workstation

The *CellSim3D* package meets all of the goals above by taking advantage of the maturity the methods and algorithms taken from the discipline of Molecular Dynamics (MD). MD has advanced significantly since its inception over 60 years ago [44, 45] (see full discussion Chapter 2) both

in terms of algorithmic flexibility and technical knowledge regarding efficient implementation in software. The algorithms and tools of MD are a good candidate for creating a model and software package that meets the above goals. MD has been demonstrated to be useful tool study all kinds of systems from simple systems such as inert gases [44, 361, 362], small molecules [48, 363], and even complex systems of interacting macromolecules [79, 84, 364–367]. The algorithms used for MD are relatively well documented and there is a whole host of software, with accompanying detailed documentation, that is available as a reference for implementing the models [51, 53, 55, 368]. It can also be used to study systems of up to millions of particles if care is taken during model development and implementation. It would allow us to study very large systems of cells. Details of MD were discussed in Chapter 2.

Cells are not molecules, but there is nothing in MD, per se, that limits its use to only molecular systems. The basic idea is based on Newtonian Mechanics, which is suitable to studying everything from molecules to planets — under the right circumstances. We can use the same to study cells, as long as we confine our studies to certain domains of length and time scales, and we approximate the interactions between them appropriately. The cell is the perfect example of a complex, multi-scale object. All of the processes that occur at the cellular level, have their roots in the molecular state transitions which occur at much smaller length and time scales. Atomic bonds vibrate in the femtosecond range, molecular conformational changes occur on the nanosecond to microsecond range, and macromolecular conformational changes may occur on very large timescales, up to seconds or minutes. Changes at the cellular level occur over minutes, hours, or even days. It is not possible to simulate all of these levels of scale atomistically — the computational cost is prohibitive. But there is a solution to this, and that is coarse graining.

Coarse-graining¹ is the process of taking known information of the underlying system, and using it to create new force fields that hide the interactions of the smaller time and length scales. We can define MD force fields by coarse-graining in a bottom up manner or in an top down manner. Bottom up would entail starting from the fundamental building blocks of our system (such as the atomic state changes), and taking in-

¹Coarse-graining is discussed in more detail in Section 2.2

formation from it up in time and length scale. One can alternatively take information from higher scales and bring it down to the desired scale. For example, the overall elasticity of the cell membrane can be deduced from the biochemical interactions between the actin filaments, and the myosin motors, that are part of the actomyosin cortex [19, 43] (bottom up); or from the mechanical measurements of the stiffness of cells carried out in the lab [369, 370] (top down).

The *CellSim3D* model is such a coarse-grained MD model for cell behaviour. We will first consider what the assumptions are in this model in Section 5.1, Section 5.2 will discuss the *CellSim3D* force field in detail, along with some details such as how to carry out cell division. Together these two sections lay out the basis for the coarse-graining process. In Section 5.5 we will see details of the *CellSim3D* software package, with how the different algorithms of the model are implemented, and explore some of the analysis tools available with the package. In addition to all of the algorithmic features of *CellSim3D* that we discuss in this chapter, it is implemented to run on Graphics Processing Units (GPUs). These are highly parallelized hardware devices that are known to accelerate MD simulations [55, 368, 371, 372].

5.1 *CellSim3D* Assumptions

In Section 3.2 the idea of the *mechanical* cell was laid out. It is not that the biological aspects which were ignored in this picture, for example the numerous organelles, are unimportant, but considering them in detail would make the whole endeavour intractable. The mechanical cell does make the system simpler, but we need some more assumptions to move on.

Let us first outline the goals that this new model should meet. We want to study cell behaviour, growth, and ultimately how tissues behave. What this means is that the model should contain terms that approximate the interactions pertaining to the needs below:

1. The model should be three-dimensional. Cells are three dimensional objects, so we should give them the full 3D treatment.
2. The model should contain terms which approximate the strength and the manner in which cells interact with each other or their en-

vironments (the extracellular matrix, liquid medium, or other cells). The physical origins of this are explained in Section 3.2.1.

3. A cell's growth and division, and its effect on the (new) cell's surroundings, should be approximated, with allowances for extensions or refinements for the interaction terms.
4. The mechanical response of the cell to external stimuli should be simulated, even if the stimulus itself is not mechanical.
5. It should be able to study cell migration
6. If possible, the interplay between the terms above.²

Even when ignoring the *biological* aspects of cell behaviour and only focusing on the *mechanical* (set aside for the moment the interplay between the two [18, 38]), there is a lot of complicated interactions one has to take into account if one wants to simulate the mechanical cell. To do this, we have to be clear about what assumptions we make, and what constraints apply to the *CellSim3D* model.

Cell surfaces can be treated as a viscous material.

The mechanical cell (Figure 3.3) is constructed of a cell membrane³ which contains two major components, the actomyosin cortex, and the lipid bilayer. These will be modelled as a flexible material. Since the membrane can also be viscous (the actin filaments can flow past each other), we *should* treat the material to be viscoelastic to capture this behaviour. However, we neglect the viscoelasticity for now and assume the membrane is a viscous fluid.

The extracellular matrix is a liquid.

Most tissues are not just a collection of cells. The extracellular matrix (ECM) plays an important role in the behaviour of cells, and it is constructed of many different types of proteins [11]. However, we do not explicitly model the ECM, but only approximate it as a fluid.

²We will see later that this in particular may not require explicit modelling, it will arise naturally from the system, see Section 6.2.

³In this thesis we use the term “cell membrane” to refer to the plasma membrane (lipid bilayer) plus the actomyosin cortex under it.

There are no long-range interactions between cells.

We assume that all cells in our simulations interact only through mechanical contact. Hormones, or synapses, are examples of long-range communication between cells. We ignore this long term interaction.

Cell death can be ignored.

There will be no terms in this model to include cell death. Cells can die in reality due to unfavourable environmental conditions, lack of nutrient, or some signal from the organism that they are a part of, such as programmed cell death [3, 373, 374].

All cells are spherical at mechanical equilibrium with themselves.

A cell, without a cell wall, will be more or less spherical when in liquid, due to the balance of forces between the cell membrane's contractility, and the incompressibility of the cell's contents [189, 375]. It has also been suggested that a high sphericity of parent cells is a necessary condition for cell division [193, 376, 377].

Cell-cell interactions are isotropic.

The mechanical properties of the cell are not necessarily uniform in all directions. The density of Cell Adhesion Molecules (CAMs) can vary from location to location in the cell membrane. We assume that they are isotropic for our model.

The cell type is determined by its mechanical properties.

We assume that each cell type is defined uniquely by its set of parameters.

Only symmetric cell division occurs.

Section 3.3.1 shows a variety of ways that cell division can occur. We assume that cells will only divide through their centre of mass and symmetrically.

The mechanical properties of all cells are uniform over their surface

The mechanical properties of the cells such as stiffness [179], and adhesion strength [378] can vary in real cells. However, we assume that they are uniform in this model.

5.2 The Force Field and Cell Structure

In Molecular Dynamics simulations the force field approximates the physical interactions of the particles in the system. These expressions of potential, or force as will be the case below, contain information about how the underlying system behaves physically — with the caveat that it is only applicable to certain time and length scales. Namely, the size of an average cell and the time required for one division cycle. Keeping this in mind, we will proceed to discuss the force field used in this thesis, the *CellSim3D* force field. All of the terms in the force field are related to the properties of the mechanical cell 3.2.

5.2.1 Cell Shape and Topology

As a starting point, we will use the CeDEM model introduced in Section 3.6.5 and in Refs. [43, 299], which describe a 2D for cells, that we will extend into 3D. Since CeDEM is a 2D model it can naturally not describe three dimensional tissues. Even the 2D systems that we do study with CeDEM only approximates the quasi-3D structure of their real counterparts, epithelia. It is therefore desirable to make a 3D package available.

Since cells can come in various shapes and sizes, we would need to accept the shape of the cell as input and triangulate its structure. This an unnecessary complication, and it involves the use of meshing algorithms that are out of the scope of this thesis. For simplicity we will make use of a simple, known geometry that can be easily coded into the simulator package. If needed there are libraries, such as the Computational Geometry Algorithms Library [379] (known commonly as CGAL), that can be used to create meshes of arbitrary shapes in the future. We have already assumed that the cells are spherical at mechanical equilibrium (Section 5.1), so we begin with a spherical shape of the cell surface, just as the one shown in Figure 5.1 (a). The intracellular portions of the force field will act between nodes on the surface of the cell, as shown in the zoomed in cutout of Figure 5.1 (a).

The locations of the nodes on the cell surface and the connectivity between them should be chosen such that:

The nodes are distributed uniformly

The distance between nearest neighbour nodes should be approximately the same, to simulate cells with an actomyosin cortex that is relatively uniform over the whole cell. Later, these same nodes will be used to stimulate the interaction between the cell adhesion molecules, and that interaction should be uniform over the surface of the cell as well.

Surface resolution is sufficiently high, but not too high

While it would be helpful for the number of nodes to be low, as the lower this number, the faster the simulation can be, it also needs to be high enough to allow for the spherical shape to be resolved sufficiently.

The number of nodes should close to a multiple of 16 or 32

This is a detail related to implementation on GPUs. Memory operations (read/write) on GPUs are more efficient if the number of particles is a multiple of 16 or 32 (depending on the GPU in question). If it is not close to this number, memory transfer can be hampered. This requirement arises from need to accelerate the software on GPUs.

These requirements for the cell geometry and topology can be difficult to comply with, so we look to the field of organic chemistry as inspiration. The C180 fullerene, shown in Figure 5.1(b), meets the criteria above. It is a carbon fullerene made of 180 carbon atoms, three times more than its more famous sibling the, C60 fullerene. Its geometry is readily available from various sources such as Ref. [380, 381]. The carbon atoms are the nodes in our cells, and the interactions between them will be approximated by the force field. This is where the commonality ends, this force field is not to be used when studying actual fullerenes, and the physical properties of the fullerene have no bearing on the *CellSim3D* force field. The mesh on the surface of the cell will contain 180 nodes, which is of sufficient resolution while still being manageable from a performance perspective. These nodes are also distributed uniformly over the surface of the fullerene, most being arranged in hexagons and a few in pentagonal shapes. The equilibrium bond length is also relatively similar for all of the bonded nodes. Lastly, the system is quite spherical at mechanical

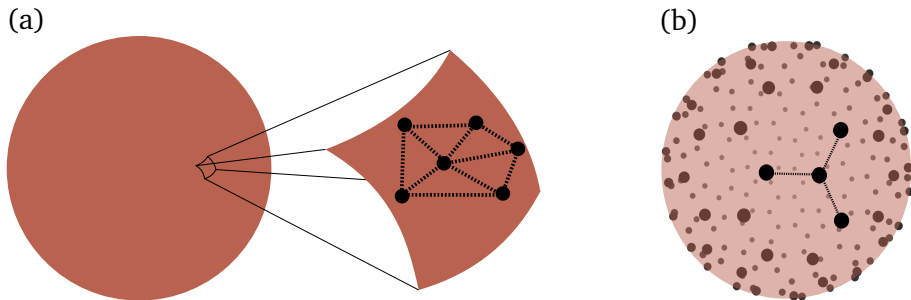


Figure 5.1: Cell structure in CellSim3D. As a starting point for our model, we assume that the cell is (a) a spherical object and that its mechanical properties are approximated by a viscoelastic sheet described by network of balls and spring between them. We use the geometry and topology of the C180 molecule (b) with the positions of the carbon atoms at equilibrium for the model. This image is in perspective, the closer nodes are drawn larger than further nodes.

equilibrium (with a sphericity of approximately 95%). There are multiple other fullerene geometries [380, 381] that can be used as replacements, but that is out of the scope of this thesis.

5.2.2 The Force Field

Intracellular forces are modelled with simple damped Hookean springs which themselves are a proxy for the cell membrane, and an internal pressure which drives cell growth. Inside the tissue, each node experiences forces that arise from intercellular interactions: adhesion and repulsion between cells, friction between cells, and friction between cells and the extracellular medium. The shapes of the simulated cells, beginning with the shape shown in Figure 5.1 (as explained in the previous section), evolve according to the competition between internal pressure, contractile forces along cell boundaries, and intercellular interactions. This allows for studying the dynamics of cell membranes, and their interactions, with higher spatial and temporal resolution. Figure 5.2 summarizes the terms in the force field.

Before describing the details of the force field, we describe the notation used in this chapter below:

- Indices of particles or cells are denoted by lower case subscripts gen-

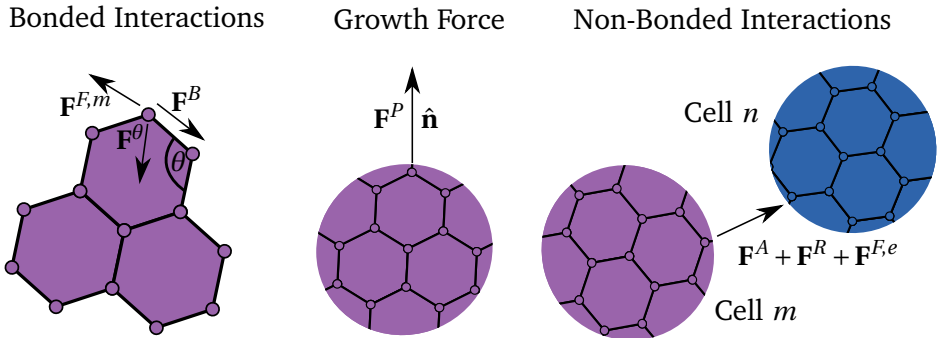


Figure 5.2: The CellSim3D force field is divided into three terms: bonded interactions (intracellular) between the nodes of the same cell i, j , the growth force within each cell acting on each node, and non-bonded (intercellular) interactions between two cells m and n . There are two intracellular forces, \mathbf{F}^B and \mathbf{F}^θ are due to deformation in bond length and angle respectively. Intercellular forces are divided into attractive (\mathbf{F}^A), repulsive (\mathbf{F}^R), and intermembrane friction ($\mathbf{F}^{F,e}$). The growth force (\mathbf{F}^P) acts isotropically on each node of the surface. Finally, the medium exerts a friction on each node ($\mathbf{F}^{F,m}$).

erally, such as i, j, k . Superscripts are never used for indices.

- Vectors in \mathbb{R}^3 are denoted with boldface and their magnitude in regular font. For example, $\|\mathbf{v}\| = v$, where $\|\cdot\|$ is the Euclidean norm.
- Constants or parameters of the force field are denoted with regular fonts.
- Position of particle i is denoted by \mathbf{x}_i
- Velocity of particle i is denoted by $\mathbf{v}_i = \frac{d}{dt} \mathbf{x}_i$, $t = \dot{\mathbf{x}}_i$.
- Force on particle i is denoted by $\mathbf{F}_i = m_i \ddot{\mathbf{r}}_i = m_i \mathbf{a}_i$.
- The difference between two scalars, or vectors, with indices j and i is denoted with subscript ij . E.g. $\mathbf{v}_{ij} = \mathbf{v}_j - \mathbf{v}_i$. If the scalars or vectors are positions ($\mathbf{x}_j, \mathbf{x}_i$), then their difference is additionally denoted with the letter “r”: $\mathbf{r}_{ij} = \mathbf{x}_j - \mathbf{x}_i$.

The force acting on node i , is given by

$$\mathbf{F} = m_i \ddot{\mathbf{r}} = \mathbf{F}^B + \mathbf{F}^\theta + \mathbf{F}^P + \mathbf{F}^R + \mathbf{F}^A + \mathbf{F}^F, \quad (5.1)$$

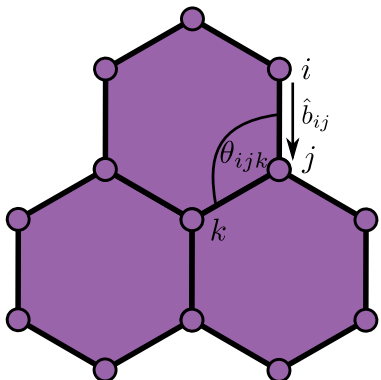


Figure 5.3: Schematic of the intracellular forces that will act on node i . This node has two first neighbours (j) which will contribute bond forces and each first neighbour has two other neighbours (k). Only one of the first and second neighbours are labelled for simplicity.

where \mathbf{F}^B is the force between two nodes that are bonded in a cell, \mathbf{F}^θ is the force due to the angles between the bonded nodes (together these two terms approximate the mechanical properties of cell membranes), \mathbf{F}^P is the force on each node i of each cell that is due to the osmotic pressure [189, 375] and growth of the cell, \mathbf{F}^A and \mathbf{F}^R are the attractive and repulsive terms between nodes of two different cells, and finally \mathbf{F} is composed of intercellular friction $\mathbf{F}^{F,e}$ and $\mathbf{F}^{F,m}$ the friction arising from the ECM. The three terms \mathbf{F}^A , \mathbf{F}^R , and $\mathbf{F}^{F,e}$ combined approximate intermembrane interactions.

Intracellular Forces

For intracellular forces, we denote the node that we are considering with i , bonded nodes with j , which we also name “first” neighbours, and the bonded neighbours of bonded neighbours (“second” neighbours) with k (with the condition that i and k refer to different nodes). Figure 5.3 shows one first neighbour and two second neighbour nodes, the rest are not labelled for simplicity, refer to this figure when considering the force definitions below. The nodes are laid out in hexagonal topologies, with the occasional pentagon that cap the corners of the C180 fullerene. Figure 5.3 shows a small portion of the cell surface, flattened for simplicity; the nodes within the same hexagon are in the same plane, but the different hexagons are not.

Wherever possible, harmonic forces are used to approximate internode forces. This simplifies the definition of the forces in Equation 5.1 and

makes them easier to implement. If needed these expressions may be replaced or extended to simulate more complicated situations. The force between the node i , and its bonded neighbours j , of the same cell is defined as

$$\mathbf{F}_i^B = \sum_{j=1}^3 \left[k_{ij}^B \hat{\mathbf{b}}_{ij} \left(R_{ij} - R_{ij}^0 \right) - \gamma_{\text{int}} \mathbf{v}_{ij} \right], \quad (5.2)$$

where k_{ij}^B is the bonding spring constant assumed to be the same for all bonds k^B , R_{ij}^0 is the equilibrium bond length between nodes i and j (taken from the data known about C180 fullerenes), $R_{ij} = \|\mathbf{x}_i - \mathbf{x}_j\|$ is the instantaneous bond length, and γ_{int} is the friction coefficient that dampens the oscillations of the bonds, and $\mathbf{v}_{ij} = \mathbf{v}_i - \mathbf{v}_j$ is the relative velocity of the nodes. k^B and γ_{int} are related to the elastic and viscous properties of cell membranes.

A three body angle term is also defined to resist the deformation of the angle θ_{ijk} between the three nodes i , j , and k with another harmonic force which is defined as

$$\mathbf{F}_i^\theta = \frac{1}{2} \sum_j \sum_{k \neq i} -k_{ijk}^\theta \nabla_{\mathbf{x}_i} \left(\theta_{ijk} - \theta_{ijk}^0 \right)^2, \quad (5.3)$$

where the force is summed over all first neighbours j (two for the C180 topology) and all second neighbours k (six in our case), θ_{ijk}^0 is the equilibrium angle between the three nodes calculated from the C180 geometry, and lastly k_{ijk}^θ is the angle spring constant which may vary over the cell surface, but for simplicity it is set to one value, k^θ , for all angles. Note that the gradient is taken with respect to the position of node i , \mathbf{x}_i .

Each node j in Figure 5.3 bonded to two nodes i and k will have an angle θ_{ijk} in between them. The nodes i and k will have forces \mathbf{F}_i^θ and \mathbf{F}_k^θ respectively acting on them (assuming θ_{ijk} is not at equilibrium). This would finally result in net force acting on j given by $\mathbf{F}^* = \mathbf{F}_i^\theta + \mathbf{F}_k^\theta$ causing unwanted acceleration through the middle of the angle. This counteracted by simply adding the force $-\mathbf{F}^*$ onto node j .

The Cell Growth Force

As we will be simulating cell growth and division, we have included a cell growth force in the force field. The simplest ways to simulate growth would be to increase volume, increase mass, or both. For simplicity, let us not worry about increasing mass for the moment. We induce the increase in volume with a simple pressure force. This pressure stems from the physical and chemical properties of the cytoplasm (the internal component of the cell cortex); its incompressibility and its tonicity. The effect of these two properties is the pressure that is exerted on the cell membrane, either due to the addition of matter in the cytoplasm, or due to its osmotic pressure. This internal hydrostatic pressure balances the compressive forces \mathbf{F}^B and \mathbf{F}^θ .

This pressure force is defined as

$$\mathbf{F}_i^P = (PS)\hat{\mathbf{n}}_i, \quad (5.4)$$

where PS is the force due to pressure P times a unit area element on the surface S , and $\hat{\mathbf{n}}$ is the normalized vector defining a family of planes that are parallel to the tangent to the surface of the sphere at the location of i (\mathbf{x}_i). How $\hat{\mathbf{n}}$ is calculated is shown in Figure 5.4. The plane shown in green can also be used to calculate $\hat{\mathbf{n}}$, and it is also the plane in which the three neighbour nodes of i , labelled 1, 2, 3 lie. The nodes' positions are exaggerated for clarity, they would be much smaller relative to the cell that what is depicted in the figure.

Let $\hat{\mathbf{b}}_1$, $\hat{\mathbf{b}}_2$, $\hat{\mathbf{b}}_3$ be the normalized vectors from i to the three bonded neighbours of i , and then the normal to surface at i , $\hat{\mathbf{n}}_i$ can be approximated as

$$\hat{\mathbf{n}} \approx (\hat{\mathbf{b}}_2 - \hat{\mathbf{b}}_1) \times (\hat{\mathbf{b}}_2 - \hat{\mathbf{b}}_3),$$

where $\hat{\mathbf{n}}$ defines the direction of the pressure force. The magnitude of the pressure force is set by specifying a value for $(PS)_o$ as initial pressure of the cell. Growth is then induced by increasing the pressure force by $\Delta(PS)$, the *growth rate* of the pressure force up to and including $(PS)_\infty$. Thus, the cells gain volume to simulate growth. The increase in pressure will induce an increase in volume $V = V_o + \Delta V$, V_o is the initial cell volume, and cells are divided upon reaching a threshold volume V^{div} , when cells are divided

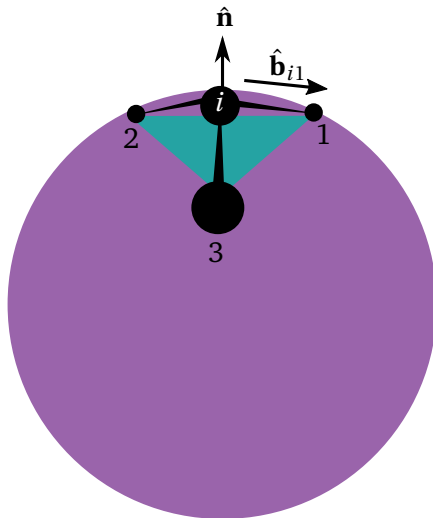


Figure 5.4: The direction of the growth force is determined by calculating the normal to the surface at node i , $\hat{\mathbf{n}}$, which is a function of the intracellular bond vectors to the first neighbours of i . $\hat{\mathbf{b}}_{i1}$ is the normalized bond vector between i and its first neighbour. Normalized bond vectors for the other two vectors are not shown. The green triangle depicts the plane used to calculate the normal $\hat{\mathbf{n}}$. The nodes are drawn in perspective, larger nodes are closer. The positioning of the nodes is exaggerated for clarity.

and mass is added via the creation of a new cell. The volume is calculated by dividing the cell into a number of tetrahedrons, using the centre of mass of each cell and the centres of each hexagonal or pentagonal facet of the C180 fullerene. The cell division algorithm is described in detail in Section 5.3.

This formulation of the pressure force is designed such that the resulting pressure force is approximately normal to the surface of the cells. Unfortunately, this approximation of the normal can fail if the cells are deformed to a concave shape, resulting in a normal to the surface of the cell pointing inwards. If the cells deform into irregular shapes, the growth force will be directed inwards, making their shapes even more irregular. To remedy this problem, a simpler formulation is also implemented defined as

$$\mathbf{F}_i^P = (PS)\hat{\mathbf{r}}_{\text{CoM}}, \quad (5.5)$$

where $\hat{\mathbf{r}}_{\text{CoM}}$ is the normalized vector pointing from cell m 's centre of mass to \mathbf{x}_i . This is recommended to be used with cells that have low intracellular stiffness values (k^B or k^θ).

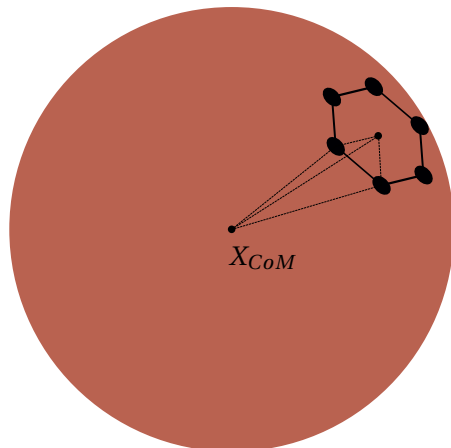


Figure 5.5: Tetrahedral subdivisions to calculate cell volume.

Intercellular (Non-Bonded) Forces

Cell-cell interaction is highly complex and varied. Mechanical cell-cell interactions are mediated through the cell membrane, and are therefore difficult to simulate as they involve many types of interactions between the molecules that constitute cell membrane. The type, strength, and even the directionality of these interactions can vary quite a bit from cell type to cell type, and between two cells of the same type with different pasts. These interactions should also be short-ranged as there is no direct long-range *mechanical* communication between cells. Long-range, that is, on the length scale of a typical cell, which is macroscopic (10-1000 μm [11]).

Short-range interactions need to be explicitly modelled as these interactions will govern the formation and strength of cellular tissues [306, 307, 313, 314]. These properties stem naturally from the formation and strength of intercellular junctions. The strength, density, and locations of the junctions are controlled by a number of biochemical factors, but from our point of view, we assume them to be uniform and constant. The morphology of tissues at different stages of development depend fundamentally on these junctions, which can vary in quantity and strength [305–307], between cell types and over time for the same cell. Using the mechanical cell approximation as a starting point, we will further assume that we can average the individual interactions of the various CAMs, including terms such as interprotein electrostatics interactions, chemical in-

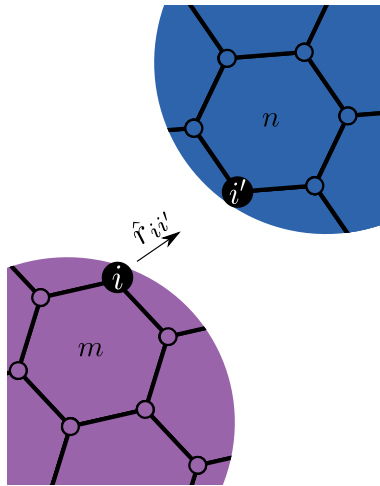


Figure 5.6: Figure showing the locations of two cells (m and n) that are close enough to trigger the intercellular forces. The attractive and repulsive forces will be between the two nodes i , i' and parallel to $\hat{\mathbf{r}}_{ii'}$, which is $\mathbf{x}_{i'} - \mathbf{x}_i$ normalized. They will also experience a friction force tangential to the relative velocity $\mathbf{v}_{ii'} = \mathbf{v}_{i'} - \mathbf{v}_i$.

teractions, and van der Waals' interactions, into a uniform interaction over the cell surface, and this uniform interaction will be broken down further into three parts: adhesion, repulsion, and (intermembrane) friction.

Figure 5.6 shows two cells m and n , the surfaces of which are within interaction range. The three short-range forces act between the nodes i , i' of the two cells m , n respectively.

The attractive, \mathbf{F}_i^A , and repulsive, \mathbf{F}_i^R forces on node i of cell m are defined as

$$\mathbf{F}_{i,m}^A = \sum_n \sum_{i'} \begin{cases} k^A(r_{ii',n} - R_o^A)\hat{\mathbf{r}}_{ii',n} & \text{if } r_{ii',n} < R_o^A, \\ 0 & \text{if } r_{ii',n} \geq R_o^A, \end{cases} \quad (5.6)$$

and

$$\mathbf{F}_{i,m}^R = \sum_n \sum_{i'} \begin{cases} -k^R(r_{ii',n} - R_o^R)\hat{\mathbf{r}}_{ii',n} & \text{if } r_{ii',n} < R_o^R, \\ 0 & \text{if } r_{ii',n} \geq R_o^R, \end{cases} \quad (5.7)$$

where k^A and k^R are the attractive and repulsive spring constants respectively, $\mathbf{r}_{ii',m}$ is the vector pointing from the node i to node i' in cell m , and R_o^A , R_o^R are the equilibrium bond lengths and cutoffs. $k^R \gg k^A$ and $R_o^R < R_o^A$, which results in forces which are the gradient of a potential $U(r_{ii',m})$ that looks similar to the Lennard-Jones potential with an equilibrium length slightly smaller than R_o^R . The adhesive part represents adhesion between adjacent cell membranes, and the repulsive part prevents

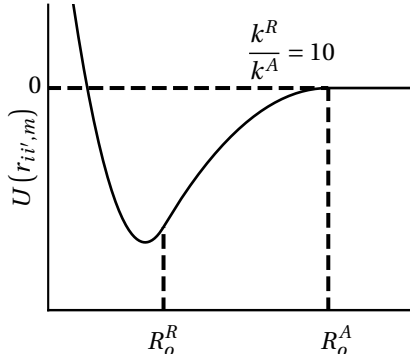


Figure 5.7: Intercellular potential. This is the integral of the forces defined in Equation 5.6 and Equation 5.7.

overlap of two membranes upon each other. The shape of the intercellular potential, shown in Figure 5.7, can be changed by modifying $\frac{k^R}{k^A}$.

The last intercellular force is intermembrane friction, this term is defined as

$$\mathbf{F}_{i,m}^{F,e} = \sum_n \sum_{i'} \begin{cases} -\gamma_{ext} \mathbf{v}_{ii'}^{\tau_m} & \text{if } r_{ii',n} < R_o^A \\ 0 & \text{if } r_{ii',n} > R_o^A, \end{cases} \quad (5.8)$$

where γ_{ext} is the intermembrane friction coefficient. The magnitude of γ_{ext} can be different depending on the cells that are interacting, however we assume that it is the same between all cells, and $\mathbf{v}_{ii'}^{\tau_m}$ is the component of the relative velocity $\mathbf{v}_{i'} - \mathbf{v}_i$ tangential to the surface of m at \mathbf{x}_i .

The final term in the *CellSim3D* force field accounts for the interactions between cells and the medium, which is just viscous drag due to the medium, $\mathbf{F}_{i,m}^{F,m}$, given by

$$\mathbf{F}_i^{F,m} = -\gamma_m \mathbf{v}_i \quad (5.9)$$

where γ_m is the drag coefficient due to the medium. The medium is assumed to be a simple fluid here. The extracellular medium is made of multiple proteins in addition to just liquid, known collectively as the ECM—see [200] for a discussion on ECM structure.

The term \mathbf{F}^F in Equation 5.1 is the sum of the two frictions $\mathbf{F}^{F,e}$ and $\mathbf{F}^{F,m}$.

5.2.3 The Integrator

Normally, in MD algorithms the velocity-Verlet integrator [382], that are appropriate for simulations of atomistic simulations are used. These integrators are not suitable for *CellSim3D*, however, as there are friction forces in the force field: intracellular force damping, intermembrane and medium friction. The first two depend on the relative velocities of particles, and the last one acts on all particles in the medium. These terms require the use of different methods. We take the approach used in the field of Dissipative Particle Dynamics (DPD) [154]. A review of DPD is out of the scope of this work. Suffice it to say the DPD velocity (DPD-VV) Verlet integrator [160] is known to be suitable for these systems, see Table 5.1. DPD-VV has been described and tested in detail in Refs. [160, 161]. The algorithm is listed in Table 5.1.

DPD-type systems have three kinds of forces:

- \mathbf{F}^C , the conservative forces.

These encompass the part of the force field that is not frictional, they approximate the attraction or repulsion between the different cell nodes. In our cases, these are the bonding forces \mathbf{F}^B from Equation 5.2 without the bond damping term, the angle forces \mathbf{F}^θ defined in Equation 5.3, the attractive and repulsive forces \mathbf{F}^A & \mathbf{F}^R (Equation 5.6 & Equation 5.7), and the pressure force \mathbf{F}^P , Equation 5.4 or Equation 5.5.

- \mathbf{F}^D , the dissipative forces.

These encompass all the frictional terms: the bond damping part of the bonded force in Equation 5.2, intermembrane friction $\mathbf{F}^{F,e}$ defined in Equation 5.8, and medium friction $\mathbf{F}^{F,m}$ defined in Equation 5.9.

- \mathbf{F}^R , the random forces.

This term arises from the stochastic processes that originate from the thermal motion that of the particles in the medium, which are not explicitly simulated. When this term is non-zero, the system becomes a DPD type system. This force is not used in the current version of *CellSim3D*, as we assume that there are no fluctuations in the system.

(1)	$\mathbf{v}_i \leftarrow \mathbf{v}_i + \frac{1}{2m_i} (\mathbf{F}_i^C \Delta t + \mathbf{F}_i^D \Delta t + \mathbf{F}_i^R \sqrt{\Delta t})$
(2)	$\mathbf{x}_i \leftarrow \mathbf{x}_i + \mathbf{v}_i \Delta t$
(3)	Calculate $\mathbf{F}_i^C\{\mathbf{x}\}$, $\mathbf{F}_i^D\{\mathbf{x}, \mathbf{v}\}$, $\mathbf{F}_i^R\{\mathbf{x}\}$
(4a)	$\mathbf{v}_i^o \leftarrow \mathbf{v}_i + \frac{1}{2m_i} (\mathbf{F}_i^C \Delta t + \mathbf{F}_i^R \sqrt{\Delta t})$
(4b)	$\mathbf{v}_i \leftarrow \mathbf{v}_i^o + \frac{1}{2m_i} \mathbf{F}_i^D \Delta t$
(5)	Calculate $\mathbf{F}_i^D\{\mathbf{x}, \mathbf{v}\}$

Table 5.1: DPD-VV integration algorithm [160]. \mathbf{F}^C are the conservative contributions to the force field, namely the intracellular and intercellular interactions, \mathbf{F}^D is the dissipative part — the friction part, and \mathbf{F}^R is the random component of the force field, which is zero in the current CellSim3D force field (Eq. 5.1). The positions and velocities of particle i , are given by \mathbf{x}_i and \mathbf{v}_i , respectively, m_i is the particle mass and Δt the time step. When the stochastic part is enabled, the steps (4a) and (4b) have to looped until the velocity converges.

Another advantage of this integrator is that it reverts back to regular Verlet when the friction coefficients and the random noise terms are reduced to zero. One may study a range of different regimes without altering the integrator.

5.3 Simulating Cell Division

We set out with the goal to simulate cell growth, and study tissue growth. A vital part of cell tissue growth is the division of cells into new cells. Faithfully simulating the actual cell division process, called cytokinesis [217, 383] is impossible. Cell division is a complex multi-step process as we saw in Section 3.3. It involves process that operate on everywhere from atomic scales all the way to the cellular scale as a whole. To simplify, we start with some simple observations of the cell cycle loop

Cell Cycle Loop:

1. The cell grows until it is big enough to divide
2. The cell divides into two cells somehow
3. Each of the two cells continue on from 1.

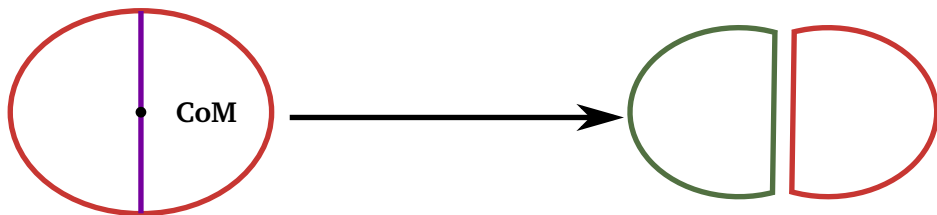


Figure 5.8: In symmetric cell division the cell division plane (or line) runs through the centre of mass and produces two identical daughter cells. Red and green cells on the right show the state of the daughter cells in the instant after division.

Each cell can be thought of as looping through individually during growth. The first portion of the cell cycle, growth, is being simulated explicitly, albeit in a very approximate manner, through the growth force (Section 5.2.2). The next step in the cycle is division (mitosis). A detailed description of mitosis and cytokinesis is out of the scope of this thesis, though an approximation of it was presented in Section 3.3.1.

Step 1. of the loop is simulated with MD, explained in Section 5.5.3.

We assume that cells can only divide symmetrically, and such that they produce two identical child cells. The final state of the child cells can be seen in Figure 5.8. Other types of division can occur as well, as was discussed in Section 3.3.1, and simulated in Chapter 4. Nevertheless we assume that this is the only way cells divide. Cell division division is achieved by making some simple geometrical arguments and creating an algorithm that will take a single parent cell that has been chosen.

After the cell has grown to a sufficient size, typically this means doubled in volume, it is set aside for division. The division algorithm, also shown in Figure 5.9, is as follows:

1. Select a random orientation (\mathbf{s}) for the cell division plane by sampling a unit sphere. The division plane passes through the centre of mass of the cell.
2. Copy all of the nodes of the parent cells such that there are 180 nodes representing each child cell at the same location as the parent cell
3. Project all of the nodes of one child cell onto another plane that is

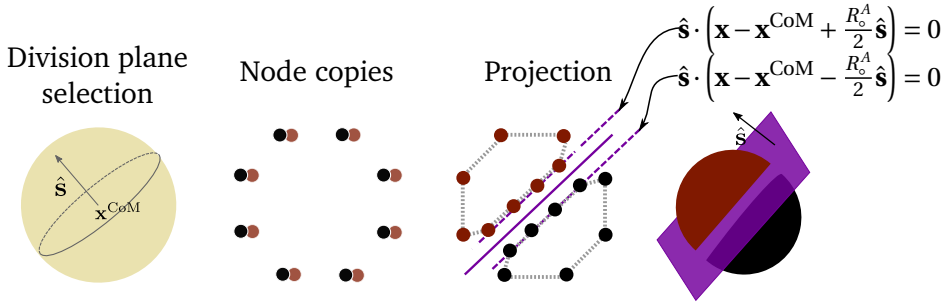


Figure 5.9: Sketch of the cell division algorithm. Left: The cell division algorithm shown in 2D for simplicity. A cell larger than threshold division volume is chosen, and its nodes are copied (black and red). Then, a randomly oriented division line is chosen (purple) such that it divides the cell in half. The corresponding nodes of the two new cells are projected such that their nodes are within interaction range. The two planes that the nodes are projected to are shown in dashed lines.

parallel to the division plane but a further by $0.5R_o^A$ to the right of the division plane, i.e. the plane $\hat{\mathbf{s}} \cdot (\mathbf{x} - \mathbf{x}^{CoM} + \frac{R_o^A}{2} \hat{\mathbf{s}}) = 0$. Do the same for the other child, but project the nodes to the left to a plane $0.5R_o^A$. The two planes are shown in Figure 5.9

In other words, the positions of the nodes of the first child cell m with respect to the centre of mass of the parent cell, shown in green in Figures 5.8 and 5.9, with parent cell n , is given by

$$\mathbf{x}_i^m = \begin{cases} \mathbf{x}_i^o - \mathbf{x}_i \cdot \hat{\mathbf{s}} - \frac{R_o^A}{2} \hat{\mathbf{s}} & \text{if } \mathbf{x}_i \cdot \hat{\mathbf{s}} \leq 0 \\ \mathbf{x}_i^o & \text{otherwise} \end{cases},$$

and the second child nodes are given by

$$\mathbf{x}_i^n = \begin{cases} \mathbf{x}_i^o - \mathbf{x}_i \cdot \hat{\mathbf{p}} - \frac{R_o^A}{2} \hat{\mathbf{p}} & \text{if } \mathbf{x}_i \cdot \hat{\mathbf{p}} \leq 0 \\ \mathbf{x}_i^o & \text{otherwise} \end{cases}$$

where $\hat{\mathbf{p}} = -\hat{\mathbf{s}}$.

From this point forward, the two cells continue their dynamics as separate entities, and the mass of the system has risen by $\sum_i^{180} m_i = 180m$, since we assume all nodes of each cell have the same mass m . This state is mechanically unstable since all of the nodes of the child cells are displaced

from their equilibrium positions, thankfully the MD simulation quickly remedies this problem. The whole process, along with the resulting three dimensional tissue, can be seen in Figure 5.10.

We also assume that there are two criteria for cell division. The first, is that the cell must be greater than a threshold volume to be divided. The threshold volume is typically double the starting volume. In principle, the actual threshold is not of great concern if it is the same for all cells. Changes in the threshold volume would only change how often the division would occur. Threshold division volume is double the starting volume in all of the simulations and results presented in this thesis.

The second criterion is that the parent cell must be sufficiently spherical to be divided. This is known from experimental measurements of the shapes of animal cells just before division cells [193, 376, 377, 383]. The sphericity ψ of an object is a measure of how close the shape is to that of a sphere. It was defined as a way to quantify the shapes of Quartz particles [384]. Sphericity (ψ) is a function of volume V and surface area A and it is defined as

$$\psi = \frac{\pi^{\frac{1}{3}} (6V)^{\frac{2}{3}}}{A}$$

Cells over a threshold sphericity $\psi_o > 0.95$ are divided. ψ_o is currently a fixed parameter in *CellSim3D*, though it can become an input threshold in the future. Sphericity is tested since cells may enter highly irregular, unfavourable conformations that have a volume that is high enough, but have an irregular shape that is not amenable to division.

5.3.1 Epithelia in *CellSim3D*

An epithelium is a quasi two-dimensional sheet of cellular tissue in which cells are coordinated in some plane, but not coordinated out of the plane. These tissues are vital for the functioning of many organs, and are vital components of all glands. Some examples of epithelial tissues include [11, 162, 385]:

- the retina; the light sensitive organ in the eye
- the epidermis; the outer layer of skin

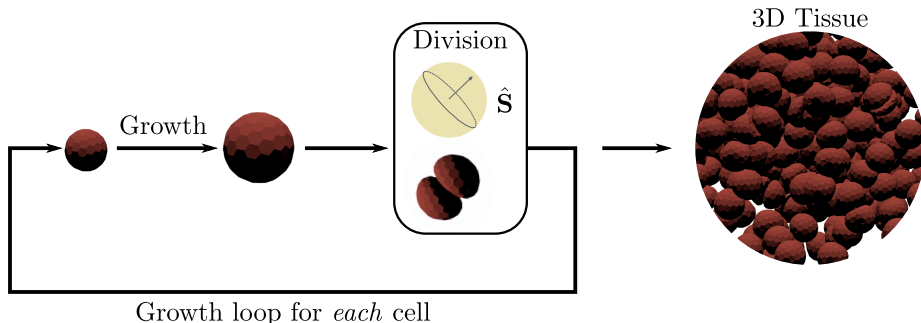
Growth loop for *each* cell

Figure 5.10: Figure showing how growth progresses in a typical simulation. The starting point is a single, or multiple cells, which each grow individually. The vector \hat{S} , is sampled from a sphere to define the division plane. This is repeated over simulation time to finally result in 3D tissue. The lag phase, was very short in this case.

- endothelia; the inner lining of blood vessels

We call epithelia *quasi* two-dimensional because even though epithelia themselves are relatively planar, at least locally, the cells that they are composed of are, of course, three dimensional. Moreover, as a single object, epithelia can be the surfaces of complex geometries, with varying curvatures. As a general model and package, *CellSim3D* should be able to simulate two dimensional tissues (i.e. epithelia) as well. When studied experimentally, since these tissues can be laid flat to have a planar structure, they are easier to characterize with conventional experimental methods, such as fluorescence microscopy, with a higher abundance of experimental data for them. Comparing to known data about epithelial systems is vital for validating *CellSim3D*. Furthermore, many of the models that exist in literature, some of which are summarized in Section 3.4, are two dimensional and used to study primarily two dimensional systems. Yet another reason to have a method to simulate epithelia since one would like to compare to existing methods. Fortunately, one can alter the *CellSim3D* cell division algorithm to produce such systems. We also gain the advantage of accurately portray such systems in 3D. This allows tackling further problems such as buckling, and how epithelia may interact with other objects.

CellSim3D simulations would create three dimensional tissues natu-

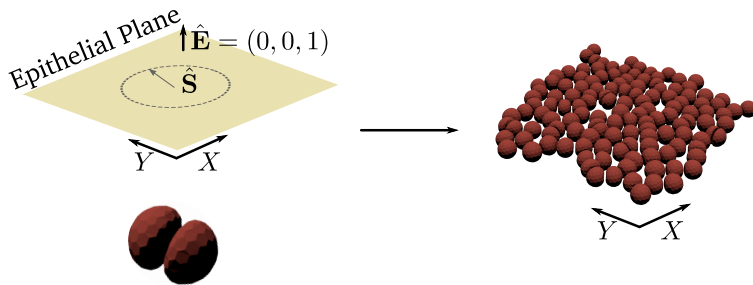


Figure 5.11: Alteration to division plane algorithm to produce a epithelial system. An epithelial plane is defined by the vector $\hat{\mathbf{E}}$, the XY-plane here, the division furrow plane is then sampled from a sphere in the plane defined by

rally with the division scheme shown in Figure 5.10 So some changes are needed to create epithelia. The simulator accepts an optional vector which defines the normal to the epithelial plane in space, \mathbf{E} in (Figure 5.11) that enables epithelium generation. One would normally also require a point in space to properly define the epithelial plane, however this is not needed since the cell division algorithm operates in the frame of reference of each cell and so the plane is assumed to be passing through the centre of each cell. Then, to simulate epithelial growth, \mathbf{s} is sampled from a unit circle in the plane defined by \mathbf{E} . This results in a configuration as shown in Figure 5.10. Epithelial cells are also confined between two plates, the bottom plate simulates basal tissue and the top plate is placed there to avoid excessive buckling.

5.4 Simulation Units

In this section we explain the units that are used in the *CellSim3D* system.

The length scale is chosen with regards to the average HeLa [386, 387]cell, which is the canonical biological model for human cells. HeLa cells have an approximate volume of $V \approx 10^3 \mu\text{m}^3$ [388, 389]. With that, we take the unit of volume in the simulation as $[V] \approx 10^3 \mu\text{m}^3$, therefore the unit of length $[L] \approx 10 \mu\text{m}$.

The internal pressure of cells has been measured experimentally by Stewart *et al.* [189] who found that it is roughly $10^{-8} \text{ N[L]}^{-2}$. We also

assume that the area of the average cell is approximately $A \approx 5 [L]^2$ (from $[L]$ and the average volume of a cell). The total force on the membrane due to the pressure is $\sum_i F_i^P \approx 5 \times 10^{-8} \text{ N}$. Each cell is made of approximately 200 nodes, then the average mass per node is 2.5×10^{-10} , The pressure in the system can grow, and there are other forces as well, so we set the unit of force to $[F] = 10^{-9} \text{ N} = 1 \text{ nN}$.

The Young's modulus of whole mitotic cells was also measured by Stewart *et al.* [189] to be $E \approx 1 \times 10^{-9} \text{ nN} \mu\text{m}^{-2} = 100 [F] [L]^2$. E is assumed to be related to k^B , the spring constant of the bonding springs in Equation 5.2, by $k^B = E \frac{A_o}{R_o}$, where A_o is the cross-section area of the cortex in the mechanical cell, R_o is the equilibrium bond length of the springs used to approximate the mechanical cell membrane. From the C180 structure this equilibrium length is $\approx 0.1 [L]$, so we rearrange to obtain a spring constant on the order of $10^3 [F] [L]^{-1}$.

We will borrow the analysis carried out in Ref. [43] for CeDEM to determine up with possible values of the adhesion and repulsion spring constants. They argued that that the repulsion forces should be stronger than internal pressure forces. This follows from the fact that a pressure force of $(PS)_o$ is pushing outwards against neighbouring cells, so more rigid cells require stronger repulsion between them. They begin by requiring that the two spring constants can be assumed to be defined as $k^R = R k^B$, and $k^A = A k^B$, with proportionality constants R and A . The force $F_i^P = (PS)$ will be pushing outwards on the surface of the cell, so the repulsive constant is set to (PS) which is on the order of 100; i.e. $k^R \approx 100 k^B$. The adhesion spring constant is set based upon an assumed energy density of cell membranes $U_{\text{adh}} = 2.5 \times 10^{-17} \text{ J} \mu\text{m}^{-2}$ which translates to $0.25 [F] [L] [L]^{-2}$. This same adhesion energy is related approximately to $U_{\text{adh}} \approx k^A (R_o^A - R_o^R)^2$, which results in a the scaling value $A = 0.5$ with $R_o^A \approx 2 R_o^R \approx 0.2$.

The mass is set by comparing to the mass of HeLa cells which is on the order of 10^{-12} kg [390]. Setting $[M] \approx 10^{-12} \text{ kg}$, and assuming a cell mass of 1 $[M]$ makes the mass of a single node $\sim 0.01 [M]$. Using this information the damping coefficient of the bonded intracellular force is set to $\gamma_{\text{int}} = 100$, which is well beyond the critical damping of the bond which is $\gamma_{\text{int}}^c = 2\sqrt{k^B m} \approx 10$ (allowing for some variation in k^B and m).

The unit for time is set such that it produces an epithelial system comparable to a *Drosophila* wing disc at 10 hours (see Ref. [43] for details),

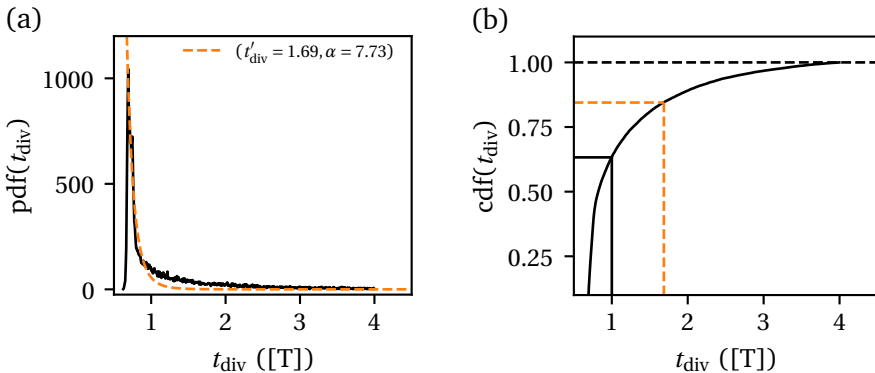


Figure 5.12: Measurement of average cell division time during a simulation run with the input parameters shown in Table 5.2. a) Probability density function of the time required a cell to divide, measured in number of time steps times Δt and over 25,900 division events resulting in approximately 26,000 cells. Most cells divide in the interval [0.75, 1.0]. The long tail indicates some minority of cells that divide very slowly. The dashed orange line shows a Pareto distribution fit with parameters $t'_{\text{div}} \approx 1.41$, $\alpha \approx 8.05$. (b) Cumulative distribution function of cell division times. Approximately 63% have divided by $t_{\text{div}} = 1$ (solid black line), and 83% by $t_{\text{div}} = 1.69$ (dashed orange line).

and time step $\Delta t = 10^{-4}[\text{T}]$. The viscosity of the cell cytoplasm, which is one of the causes of the drag force on the cell membrane, is 10^3 Pas [236, 391], we use values of $\sim 1 - 10$ in our simulations, which results in a speed up of approximately a factor of 10 in *CellSim3D*, compared to real time scales.

Cells can take anywhere from a few minutes in fruit flies [392], seven hours in hamsters [393] to 20 hours [394] in humans, to complete their cycle. A common time unit for all cell types would be inadequate. We solve this problem by scaling simulation time by the mean time for a cell to divide, t_{div} . This is measured by tracking the time required for each division event, and analyzing the resultant distribution of t_{div} . Figure 5.12(a) shows the probability density function (pdf) of t_{div} measured over roughly 25,900 division events resulting in approximately 26,000 cells with the parameters shown in Table 5.2 after a simulation lasting 150,000 steps. The mean division time can be quantified by fitting a Pareto distribution to the pdf in Figure 5.12(a). The Pareto distribution, also known colloquially as

the “80-20” rule, is defined as

$$Pr(T_{\text{div}} > t_{\text{div}}) = \begin{cases} \left(\frac{t'_{\text{div}}}{t_{\text{div}}}\right)^{\alpha} & \text{if } t_{\text{div}} \geq t'_{\text{div}} \\ 1 & \text{if } t_{\text{div}} < t'_{\text{div}}, \end{cases}$$

where t'_{div} would be the time below which approximately 80% of the divisions occur, and α is a shape parameter which describes how close, with respect to t_{div} , the rest of the data is. Fitting to the Pareto distribution reveals that most cells divide with a division time of $t_{\text{div}} \approx 1.69$, and large majority of cells divide with $0.75 \leq t_{\text{div}} \leq 1.69$. The cumulative distribution function (cdf) for this data is shown in Figure 5.12(b), which shows that approximately 63% of cells divide by $t_{\text{div}} = 1.0$. For simplicity, we shall use this value to set the scaling factor in our simulations $\tau = 1.0$ which we will refer to as the “mean time to division” in this thesis.

The pressure force increase rate, which is a proxy for the volumetric growth rate, is set as $\Delta(PS) \approx 1 - 10 \times 10^{-4} [F] [L]^{-2}$. The pressure varies in the range $(PS)_o \approx 65 - 85$ which keeps cellular volume at roughly 1 [V]. The maximum pressure $(PS)_{\infty}$ and the pressure growth rate $\Delta(PS)$, can be chosen to set the desired growth rate in a system.

Table 5.2 summarizes the parameters and their numerical values used typically in *CellSim3D* simulations. These can be set in the input configuration file that is passed to the simulator, as is explained in Section 5.5.5.

5.5 The *CellSim3D* Software Package

The model and the algorithms outlined above have been implemented into a open source software package. The software package has the same name, *CellSim3D*. The full source code is available under the GNU General Public License version 2 (GPLv2) [395] on github at <https://github.com/SoftSimu/CellSim3D>. The software is written in standard C/C++ and is accelerated with CUDA [396] to run on a single NVIDIA Graphics Processing Unit (GPU). Purely from a memory use standpoint, most modern mid-range GPUs can store up to 10^5 cells (such as the GTX 970 or the GTX 980) and high end GPUs (such as the GTX 1080Ti, GTX TITAN, or TESLA devices) can store up to 10^6 . Most modern laptops and workstations with NVIDIA GPUs have enough capacity for cell populations on the

Parameter Name	Notation	Value	Units
Nodes per cell	N_c	180	-
Node mass	m	0.02 to 0.04	20 to 40 fg
Bond stiffness	k^B	1000	100 nN/ μm
Bond damping coefficient	γ_{int}	100	0.01 g/s
Minimum pressure	$(PS)_o$	50	0.5 nN/ μm^2
Maximum pressure	$(PS)_\infty$	65	0.65 nN/ μm^2
Pressure growth rate	$\Delta(PS)$	0.002	2×10^{-5} nN/ μm^2
Attraction stiffness	k^A	500	50 nN/ μm
Attraction range	R_o^A	0.2	2 μm
Repulsion stiffness	k^R	1×10^5	1×10^4 nN/ μm
Repulsion range	R_o^R	0.3	3 μm
Growth count interval	-	1×10^3	[†]
Intermembrane friction	γ_{ext}	1 to 10	10 to 100 $\mu\text{g}/\text{s}$
Medium friction	γ_m	1 to 10	10 to 100 $\mu\text{g}/\text{s}$
Time step	Δt	0.0001	*
Mean time to division	τ	1.0	**
Threshold division volume	V^{div}	2.0	$2000 \mu\text{m}^3$

[†] In units of Δt

*,** In units of mean time to cell division, which varies between cell types

Table 5.2: Values of the parameters used for this work. The values shown here determine the mechanical properties of each cell. They are normally varied slightly to simulate cells of different type.

order of 10^{3-4} . As more and more global memory becomes available on hardware, even larger systems can be simulated in the future. 100,000 cells can be stored in the memory of a computer configured with the a GTX980 GPU (4GB of RAM); simulating a system of up to approximately 12,000 cells required approximately 2.5 hours.

CellSim3D has been tested on the following GPUs: GTX 760, GTX 780, GTX 980, GTX 1080Ti, GTX Titan Xp, GTX 960M, on systems configured with Intel CORE i7 and i5 CPUs (CPU architecture is of no consequence). The software has been successfully compiled with CUDA versions 5.5 to 9.1 — with the corresponding supported gcc versions (see the CUDA Toolkit Documentation [396]). Most of the performance of the simulator is from hardware design of GPUs, and not from complex compiler optimization, thus the software is agnostic of the compiler versions used.

Communication and synchronization are known to be bottlenecks when accelerating any kind of computations with GPUs due to the higher latency of communication between host RAM (Random Access Memory) and GPU RAM. In fact, this is a problem when parallelizing any code to run in a multi-threaded configuration. Therefore, as much of the computations as possible are done entirely on the GPU. The *CellSim3D* force field (Eq. 5.1) contains only short-range potentials. This allows us to write the software such that you allocate a single thread to compute all of the necessary calculations for each particle (or cell, depending on the computation), since no information regarding other particles is needed — apart from their positions and velocities of course. Thus, the entire potential and force calculations can be done on the GPU only, greatly minimizing the need for communication. Communication is only necessary for input and output to disk to produce trajectory files.

The use of atomic operations allows the simulator to generate neighbour node lists on the GPU itself. Neighbour lists are generated with a simple domain decomposition algorithm that subdivides the simulation box into sub-domains in parallel. The domain that each cell belongs to is also calculated in parallel. This information is then used to calculate a per-node neighbour list during force calculations.

Thanks to the above optimizations, most of the computations are done in CUDA only, with minor host code in C/C++ that controls execution and handles data input and output. Therefore, normal workstations with

modest mid-range CPUs may be used with *CellSim3D* without much degradation in performance.

5.5.1 Implementation

Full documentation for the simulator is not within the scope of this thesis. The most important parts of the code are summarized here. The documentation wiki on the github page (<https://github.com/SoftSimu-/CellSim3D>).

Core Simulator and system requirements

Since most of the heavy computations are carried out on the GPU, the requirements on the rest of the hardware configuration is not stringent. These modest hardware requirements allow the study of interesting systems with relative ease on a single node with a single GPU.

The memory use is constant over the simulation and can be configured with the input JSON file, see Fig. 5.13. This is to avoid repetitive allocation/deallocation of memory on the host and on the GPU. Memory is allocated for a maximum number of cells for the simulator. This number is typically much bigger than needed in the actual simulation, but a large allocation is needed since we simulate division in the simulations.

CellSim3D can be easily compiled with the `makefile` provided. Only Linux operating systems are supported at the moment. Any corresponding gcc compiler that is required by the CUDA version may be used. For example, CUDA 9.1 requires gcc 5.3.1 on Ubuntu 16.04 running on x86_64 systems. Refer to the CUDA Toolkit Documentation for details [396].

CellSim3D only depends on the jsoncpp [397] and HDF5 [398] libraries, the former is pre-packaged with *CellSim3D* for ease of use. No other libraries are needed by the simulator. Some Python libraries are required for the analysis tools, which are outlined in Section 5.5.5.

5.5.2 Minimum System Requirements:

- NVIDIA GPU of compute capability of 3.5 or higher
- 1 GB of GPU memory (4GB recommended)

- 4 GB of host memory (8GB recommended)
- CUDA 5.5 or higher (later versions recommended)
- Python 3.5, with required libraries (see [5.5.5](#))
- Blender 2.7 or higher (only needed for visualization)

5.5.3 The Simulation Loop

A sample input file `inp.json` is provided with default values of all of the simulation parameters for convenience. An example input file with an explanation of all the parameters is given in [Appendix A](#).

We will not dwell on syntax and the proper programming techniques used in the simulator here. For our purposes it is sufficient to understand the flow of information in the program, which is given below.

5.5.4 Program Summary:

1. Parse Arguments

The input arguments are the number of initial cells to be simulated, the path to the input JSON file, and the GPU id of the GPU to be assigned to the simulator. Recommendations:

- Users interested in developing for the simulator are recommended to do

```
1   export CUDA_DEBUGGER_SOFTWARE_PREEMPTION=1
```

for stable debugging. A recent version of the CUDA toolkit, GPU, and graphics driver is required for this. This allows one to debug on a GPU that is running a display server.

- A relatively modern GPU should be used, preferably one made after 2013.
- Only one instance of the simulator per GPU should be run. No other performance heavy program should be using the GPU in question. A display server (such as the X server) may share

the GPU, but we recommend a completely idle GPU for best performance.

- There should be adequate hard drive space. The program makes no checks or calculations of possible file size, as that would depend heavily on the cell growth rate $\Delta(PS)$, and the other parameters of the simulation. It is non-trivial to calculate space requirements beforehand. The simulator will terminate if space runs out without warning.

2. Allocate Memory

In the JSON file one can specify the maximum number of cells in the simulation this is used to allocate memory for all the data in the system. This value is set to 100,000 cells, which require approximately 4 GB of memory. Values of 10,000-50,000 are sufficient for most purposes. This memory is mirrored on the host as well. Both the GPU and the workstation should have sufficient memory. Once allocated, memory need not be managed again. This means that there will not be any other programs running that will required access to this allocated memory (this assumption is valid for most software). It also eliminates all memory management concerns, we allocate memory once and deallocate once at the end of the simulation. This makes the memory footprint of *CellSim3D* significantly higher compared to most MD software, but it is easily matched mid-range hardware.

3. Initialize the system

The initial conditions of this system include setting the node positions and their bonding, which are read from included data files. This data may also be provided with the input JSON file.

- The cells are placed on a uniform grid in 2D. Or randomly throughout the simulation box. This is determined by values in the JSON input file.
- A simulation box with closed boundaries is always assumed. An open boundary can be simulated by choosing a very large box size.
- While the nodes themselves have initial conditions, there are parameters that are properties of whole cells, such as initial

pressure $(PS)_o$, which are also set at this phase.

4. Find nearest neighbours

There are dedicated kernels that handle the finding of nearest neighbours in the system. This is performed every time step.

5. Set pressure (growth rate)

The growth rate of the cells must be set before the force calculations may proceed. Pressure increases from $(PS)_o$ to $(PS)_\infty$ at a rate of $\Delta(PS)$ per time step.

6. Force calculations and position updates

The force calculation is done for each particle in each cell. This part of the simulation is most susceptible to inefficiencies and may be the slowest step.

- Spring force calculation
- Pressure force calculation
- Internal Damping force calculation
- Intercellular Force calculations (adhesive, repulsive, and friction)
- Time propagation with the DPD-VV integrator, see Section 5.2.3

7. Analysis and cell division

Now some analysis of the cells is done which is needed to determine which cells are ready to divide. The volume of each cell is calculated by using the conformation of each cell. Those cells with high enough volumes are divided. The division is not spontaneous and is done by introducing new mass points and separating the mass points of the parent cell into two daughter cells. The division plane is chosen so that it divides the parent into two equal halves, see Section 5.3.

The simulation loop and the basic algorithm of the simulator is summarized in the form of a flow chart, shown in Figure 5.13.

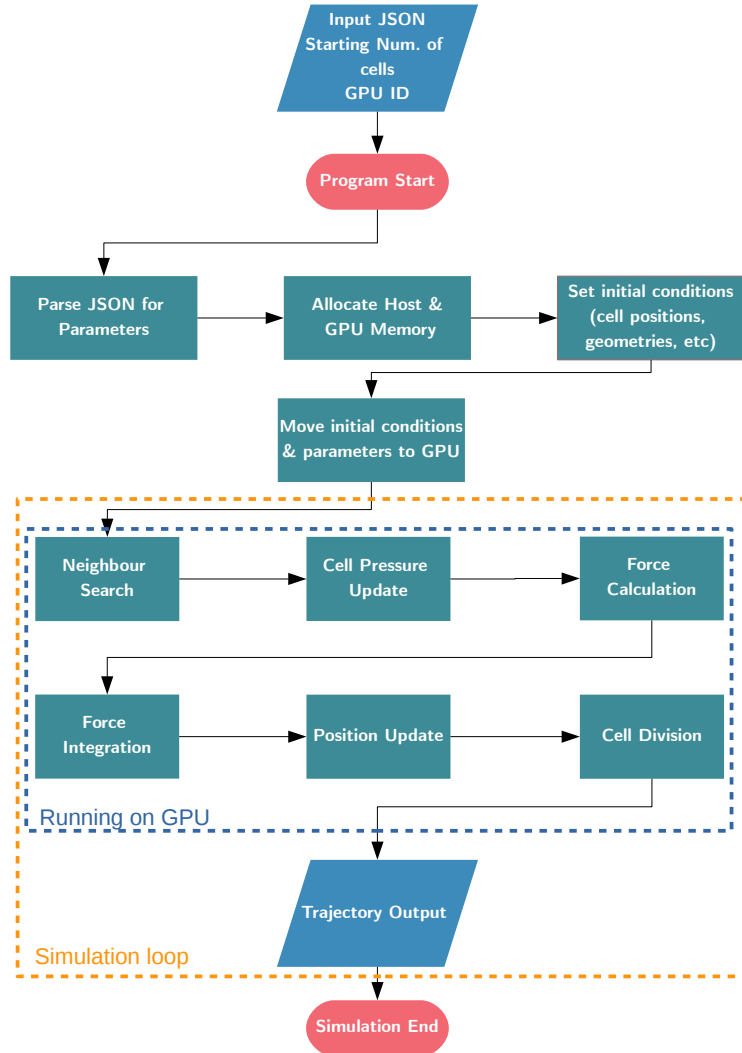


Figure 5.13: Simulation flowchart. All of the parameters used in the simulation are set in a JSON (JavaScript Object Notation) file that is given as an argument to the simulator (the program distribution includes a sample file). The GPU id (assigned by the system) and the initial number of cells are also program arguments. Flowchart reproduced from [42] with permission from Elsevier.

5.5.5 Source files

Here we discuss some of the source files that are in the software package here. There are two main types of files that the *CellSim3D* package. The first, and most vital, are the source files that contain all the code. The second are data files that contain information such as cell geometry and bonding. There is also an interface to the trajectory file that is output by the simulator, and a collection of scripts that can be used for analysis.

The list below summarizes some of the source code files in the *CellSim3D* package.

- `GPUBounce.cu` is the main source file that outlines the flow of the simulation. For all intents and purposes, it contains *all* of the simulator code, the rest of the files only contain function calls that must be linked with this file. GPU selection, memory allocation, variable initialization, simulation, and output is handled here.
- `propagate.cu` contains mostly GPU kernel code written in CUDA. All of the forces are calculated and integrated here.
- `propagatebound.cu` contains all of the routines for calculating the neighbour lists of each cell. The operation is broken down into two steps: 1) finding the *cells* which neighbour each other, 2) then, finding the nodes that neighbours each other.
- `volume.cu` calculates cell volumes in parallel on the GPU, and flags them for division if needed. The volume is calculated by subdividing each cell into tetrahedra, calculating the volume of each tetrahedron, and summing over all tetrahedra for an approximation of the volume. Cells above a threshold volume and with a high sphericity are chosen for division.
- `celldivision.cu` performs the actual cell division. Any cell that is greater than a threshold volume is divided, using the algorithm summarized in Figure 5.9.
- `pressurekernels.cu` contains GPU kernels that are used to track and update the internal cell pressure. Each cell starts at a value of (PS_o) , this pressure grows at the rate of $\Delta(PS)$ up to $(PS)_\infty$.

And the data files are:

- C180 contains the positions of the nodes (carbon atoms) from the C180 fullerene molecule, rescaled for *CellSim3D*.
- C180N contains topological (which node is bonded to which) information
- C180_pentahexa contains a listing of the node indices that are in each pentagon and hexagon in the C180 structure. This is used during volume calculation and in the visualization script.

Input/Output and Analysis Tools

Most of the data from the simulation is written to a HDF5 [398] formatted file. This format is a hierarchical platform independent binary format that will not be discussed here. All that matters to us is that it is a powerful and flexible format that is well suited for the needs of *CellSim3D*. It is very well documented and there are many tools and APIs available to read and manage HDF5 files. Some output is also written to ASCII files, though this is being phased out in favour for the HDF5 trajectory file. Other data formats that are commonly used with MD simulations are not suitable as they do not generally support variable number of particles. The number of cells in the simulation is variable, mostly increasing or constant, and the output format should support this. The trajectory file can be read and processed in python with a packaged module named `celldiv.TrajHandle`, the trajectory handler. This is a simple interface between the trajectory output from the simulator and NumPy [399] arrays in python3. python2 is not supported. In this way, all the power of the numerical libraries available through Python can be applied easily on any of the data. All the tools, including a movie rendering script, are wrappers around this interface. This file also serves as a checkpoint for the state of the simulator. There are many tools around the handler that can perform many analyses. Quantities such as density, mitotic index, density, radius of gyration can be calculated with these tools. The Python tools require the latest versions of the following python libraries: NumPy [399], Scipy [400], matplotlib [401], tqdm [402], and pandas[403]. A file called `requirements.txt` contain-

ing a detailed list of the needed libraries, along with compatible library versions, is provided for easily building a suitable python environment.

5.6 Measuring the Performance of the *CellSim3D* Simulator

The two main challenges, in our view, that face computational scientists are that simulations are either not sufficiently large, or if they are of appropriate size, then they take very long times and a high amount of computational resources. One needs to be able to run simulations efficiently as access to hardware is expensive (to purchase, setup and maintain), and to iterate upon computational experiments quickly. We rarely only need to test a single parameter set and would like to see how a system behaves over a regions of parameter space. Therefore, it is important to have an estimate of how performant this particular simulator is. The standard way to measure this would be to see how the wall clock time per time step ($t_s(t)$) varies with different number of particles. This measurement can then be compared between different parameter sets, different hardware configurations, or even between different software packages.

The number of *cells* in a *CellSim3D* simulation is dynamic as the cells grow and divide. In fact the number of cells, $N(t)$, is generally increasing non-linearly with increasing time, at a rate that is dependent on many parameters such as the cell stiffness (approximated by bonding spring constant k^B), cell growth rate (induced by the increase in internal pressure $\Delta(PS)$), and the evolving cellular environment. We discuss this growth behaviour in more detail in Chapter 6, but an example of it is shown in Figure 5.14 (a) via the rescaled number of cells defined as

$$\overline{N}(t) = \frac{N(t)}{\max N(t)}.$$

Since $N(t)$ is a function of time, $t_s(t)$ also becomes a function of time. This complication can be circumvented if we instead measure the wall time consumed per time step *as a function of $N(t)$* . Before we do this, however, we also rescale time consumed per integration step as

$$\overline{t_s}(t) = \frac{t_s(t)}{\max t_s(t)}.$$

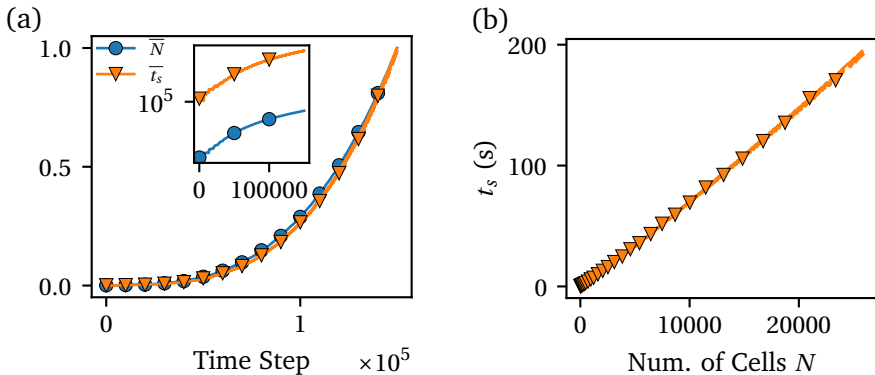


Figure 5.14: (a) The number of cells in the system \bar{N} , and the time it takes per integration time step \bar{t}_s . The two values have been rescaled so as to be compared easily, and to eliminate any effects of the hardware configuration. Note that the number of particles in the system is 180 times greater than N . Inset shows the number of cells N and time per integration step t_s . (b) Rescaled time per integration step \bar{t}_s against rescaled number of cells \bar{N} . The scaling is linear.

The rescaling is done for three reasons:

1. To make $N(t)$ and $t_s(t)$ comparable to each other by making them dimensionless.
2. To eliminate any effects of differences in hardware, driver and software configuration, and simulation parameters. All of these effect performance, but rescaling in this way cancels those factors out.
3. The number of particles per cell can, in principle, be different for different cell types, this rescaling eliminates that problem as well.

\bar{N} and \bar{t}_s will always increase monotonically over a simulation, if cell growth and division is enabled, as one can see in Figure 5.14 (a). The inset in Figure 5.14 (a) shows the unscaled versions of these measurements.

The next step, then, is to see how $t_s(N(t))$ behaves over time. This is done trivially plotting $t_s(t)$ versus $N(t)$ in Figure 5.14 (b). This graph shows that the simulator scales linearly with the number of cells in the system.

A more practical way to measure performance for the average user would be the time required to achieve a certain number of cells on a typi-

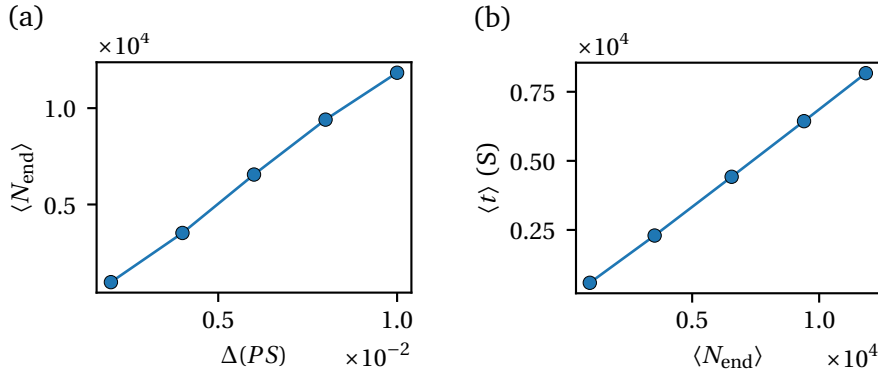


Figure 5.15: (a) The mean number of cells achieved for a typical simulation of CellSim3D time 150,000 integration steps (N_{end}). The final mean number of cells $\langle N_{\text{end}} \rangle$ increases linearly with the pressure growth rate $\Delta(PS)$. The error in the measurement is too small to show. The final number of cells increases linearly. (b) The average time needed to get to some final number of cells N_{end} , if using the parameters in Table 5.2,

cal workstation, assuming the parameters chosen in Table 5.2, with some changes in growth rate, over some number of integration steps. Exactly this is measured in Figure 5.15, which shows, for 5 simulation runs, the final number of cells after 150,000 time steps at different values of $\Delta(PS)$, $\langle N_{\text{end}} \rangle$. Linear scaling is achieved, which means that the growth rate simply increases the number of cells created in the simulation linearly. The error in the measurement is too small to plot here. Finally, the time taken to reach some number of cells N is plotted in Figure 5.15(b), which shows a linear increase the time required to reach some number of cells.

5.7 Conclusions

Our aim in this chapter was to design a model and software package with a model that was well suited to study the mechanics of cellular materials. In the introduction to this chapter we outlined two main issues with the models in this field: 1) Most of the models in literature, while well suited for the problems they were suited for (e.g. vertex models are good for reproducing the structure of tissues, but cannot be used for anything

else), are unable to simulate the dynamics of the interactions between cell membranes and extracellular medium accurately. 2) Even if we were to accept a model and use it for our research, there is a lack of open source implementation available into software that is highly performant to allow the study of thousands of cells simultaneously in 3D with high resolution.

We proposed the *CellSim3D* software package which implements the *CellSim3D* force field. The force field an extension of the 2D Cellular Discrete Element Model [43], a model that can be used to study the forces in the system as we saw in Chapter 4, into 3D. The force field contains terms that allow for the precise control of the mechanical properties of cells with great tunability. The package is a highly performant Graphics Processor Unit (GPU) accelerated software that is able to simulate up to tens of thousands of cells on a single workstation with an NVIDIA GPU. Since this software is open source and published on github (<https://github.com/-SoftSimu/CellSim3D>), researchers can also modify it to their needs if the force field is insufficient and share their improvements with others.

We will tackle the task of validating *CellSim3D* by reproducing various growth phenomena known from experiment, theoretical models, and other computational models in the next chapter.

Chapter 6

The Dynamics of Growth and The Cellular Mechanical Environment

6.1 Introduction

The growth of cells, or colonies of cells, has traditionally been an important area of study for biologists [232, 404–411]. The process of growth of cells into a colony, or organ, is called *proliferation*. The previous chapter discussed how the growth of a *single* cell can be simulated (Section 5.3). While vital, we recognize that the growth of a single cell is only *part* of the story. Growth has traditionally been studied from the biological perspective, focusing on the reactions of growing tissues to biochemical stimuli. Recently there has been a great interest in how *mechanics* can affect growth, and even vice versa. This *mechanobiology* of cellular systems is known to affect many facets of cellular behaviour including growth [412], stem cell differentiation [28, 31], and embryonic morphogenesis [413–415]. The latter is the differentiation of young embryonic cells into specialized collections that will ultimately become different organs.

Other elements of cell behaviour such as cell migration and taxis [22, 32], also contain biomechanical elements. Mechanotransduction has been studied experimentally quite extensively [21, 28–30, 38, 416, 417]. Com-

putational methods provide new insights into the processes occurring with resolutions that are not experimentally accessible. Simulations can provide detailed information about the underlying physical mechanisms and that information can be used to guide experimental explorations, or even suggest new experiments. Both theoretical [418, 419] and computational models [255, 261, 262, 294, 315, 353, 355, 356, 420, 421] (Section 3.4) have been created for this purpose.

This chapter will show how the *CellSim3D* model (Chapter 5), with its associated software package, can be used to study the growth of tissues of cells containing up to tens of thousands of cells. In Chapter 5, we discussed how to approximate the growth and division of a *cell*. Tissues consist of collection of cells. Their growth can be studied a variety of ways, some of which are discussed in Section 6.2 and compared to simulation results. It turns out that many of the growth characteristics of tissues emerge out of the *CellSim3D* algorithm organically. We will both demonstrate how this growth behaviour emerges and propose some possible physical reasons for it.

This chapter will serve three goals: 1) to validate the *CellSim3D* method and software implementation, which was discussed in Chapter 5, 2) to explain how growth can be measured with *CellSim3D*, we compare it to some known experimental and computational methods, and 3) to study the interaction between tissue growth and the mechanical environment of cells at the cellular level.

First in Section 6.2, we will explain how growth can be measured with *CellSim3D* and compare it to other experimental, computational, and theoretical results. Then in, Section 6.3, we will explore some mechanical explanations for this behaviour. The process of considering these questions, we validate our model as well.

6.2 How is Tissue Growth Studied?

We will consider only three methods of measuring growth: population trends, the rate of change of population trends, and system (cell colony) sizes. The results in this chapter were produced with the parameters shown in Table 5.2, over 150 000 steps of simulation which corresponds to approximately 15 cell cycle time intervals and $m = 0.04$, $\gamma_{\text{int}} = 1.0$, $\gamma_m = 1.0$.

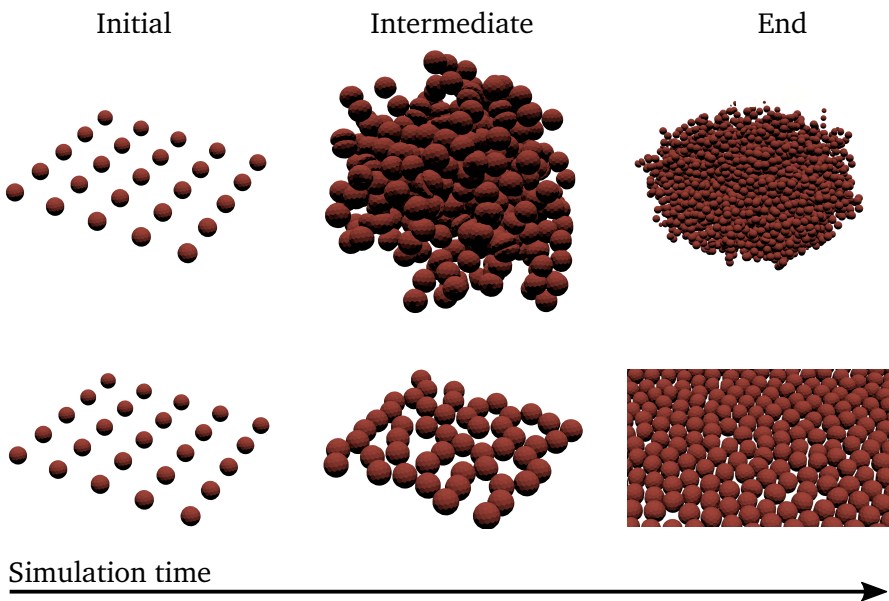


Figure 6.1: Images showing the progress of a simulation. Left: initial conditions, middle: an intermediate stage, and right: the end of the simulation using Cell-Sim3D [42] software. Top panels show the progression of system growth for 3D tissue, and the lower panels show growth of a 2D tissue (epithelia). Epithelia are created by confining them between two plates (not shown in this visualization) and by modifying the cell division algorithm. Confinement between plates avoids excessive buckling in the system. The bottom plate approximates the basal layer in epithelial tissues [11, 289]. A detailed description of how growth is simulated and how cells are divided is given in Section 5.3.

Visualizations of two simulation runs are shown in Figure 6.1. The top panel shows a simulation configured to produce 3D tissue, the bottom panel shows a system configured for epithelia. In both cases we start with 25 cells placed evenly on a grid. Over time the cells grow due to an increase in their internal pressure, as was described in Section 5.2.2. Once reaching threshold division volume, they are divided with the algorithm described in Section 5.3 configured for either 3D or epithelial tissue. Additionally, epithelial systems are confined between two plates to avoid excessive buckling in the system. The bottom plate represents the basal layer in epithelial tissues [11, 289].

Population trends are discussed in Section 6.2.1, population growth rate in Section 6.2.2, and cell tissue size in Section 6.2.3.

The reader should bear in mind that the cell growth force, and its strength, the growth rate ($\Delta(PS)$), are kept identical between all cells in all of the simulations run for this chapter. The details of this term in the force field were discussed in Section 5.2.2. Since it approximates the energy input into the cells, one can assume that the input of nutrient to all cells is identical. The growth rates discussed in this section are rates of increase of population number or system size, not of individual cells. The two are related, of course, since increasing the former would increase the rate of increase of population or system size.

6.2.1 Population Trends

In systems of cells that exist in uniform media, there is a known trend of cell population that is observed experimentally shown in Figure 6.2. Growth trends can be divided into four phases: lag, growth, stationary, and death/decay [11, 422]. The lag period, a time when nutrients and growth factor concentration is building up within cells, followed by a phase of exponential growth in the population of cells, which often asymptotically approaches a maximum that is determined by the quantity of nutrient in the system and the death rate of the cells. The stationary phase is when the death rate balances growth rate. Eventually, cell death overcomes growth and the population dies out due to the absence of nutrient. This idealized trend of cell growth is an approximation to the actual experimentally observed population trends. An experimental population trend of bacteria, carried out by Rolfe *et al.* [422], is shown for comparison in Figure 6.2 (b) with orange stars. These trends are also observed in animal cell systems that are not supported by vascular systems [237, 407]. Experimental measurement of population growth of mouse cancer cells is shown in Figure 6.2(b) (blue dots) for comparison, taken from measurements by Assanga *et al.* from Ref. [237]. The data is rescaled to make the two systems comparable; animal cells and bacteria have different sizes and growth dynamics.

Naturally, cells of different organisms will grow at different rates, and their population trends will be different, such as animal cells and bacterial cells. Anomalies in population trends can also be linked to illness [232],

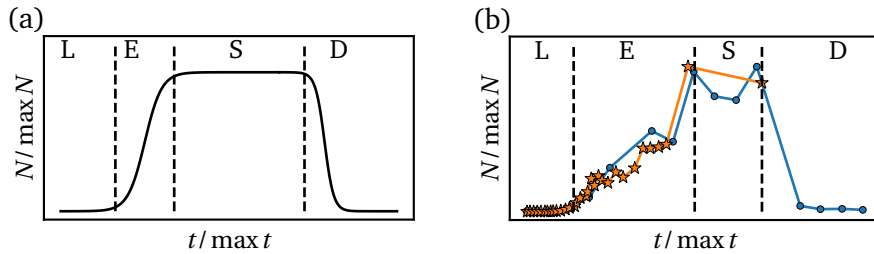


Figure 6.2: (a) Trend showing the population of cells over time for cells not supported by vascular systems. There is a lag phase (L), exponential growth phase (E), stationary phase (S), and death phase (D). (b) Example measurement of the population behaviour of mouse leukemic monocyte macrophage cell line, a type of mammalian cell (blue circles, $\tau \approx 20$ h), measured by Assanga et al. [237]. Measurement of the *S. typhimurium* growth curve extracted from the paper by Rolfe et al. [422] (orange stars, $\tau \approx 40$ min).

407]. Population trends can also be monitored to measure the response of cancer cells to treatment [423, 424]. Population curves can differ greatly within the same organism as well, depending on what stage of life that organism is in (development, reproduction, death, etc.).

All of the phases of the population trend curve are important markers of a biological system, but since we do not simulate death in *CellSim3D*, we shall ignore the death phase. The transition from lag, exponential, to stationary phase can be modelled mathematically with a number of sigmoidal functions such as those discussed in Section 3.5.1. We will use the generalized logistic function is defined as

$$N(t) = \frac{N_{\max}}{\left(1 + Qe^{-rt}\right)^{\frac{1}{v}}} \quad (6.1)$$

where $v > 0$ is a constant (most of the time $v \approx 1$), r is the growth rate and $Q = \left(\frac{N_{\max}}{N_0}\right)^v$, and $N_0 = N(t = 0)$. Note that the growth rates (r) in these functions are actually related to both the rate of increase in number of cells due to division, and decrease in the number of cells due to death. Furthermore, the growth and death rates are themselves functions of time. The stationary phase is when the two rates are balanced perfectly.

The logistic type functions will be used as a reference to validate the growth produced by simulations of *CellSim3D*. However one should bear

in mind that the generalized logistic function, and its relatives, apply to systems with a certain *carrying capacity*, which is the maximum number of cells at the saturation phase in Figure 6.2. Since we do not simulate cell death, we would not expect the output of *CellSim3D* simulations to saturate in population. However, one can still use these functions in the exponential growth region. The lag phase is immaterial, as it simply delays the onset of growth by some time interval, so we ignore it as well. Since cell death is not simulated in *CellSim3D*, one may expect to observe intrinsic growth, given by

$$N(t) = N_0 e^{rt} \quad (6.2)$$

where N_0 is the initial number of cells.

The growth loop (Figure 5.10) is the term we use for the process of cells growing and dividing. Each cell in the simulation grows by gaining volume due to an increase in its internal pressure. Once it is greater than or equal to the threshold division volume, it is divided into two child cells. The two new cells are symmetrical and oriented randomly. Each new cell then goes on to grow itself. The pressure force causing the growth was explained in Section 5.2.2 and the cell division algorithm was explained in Section 5.3.

The growth loop is repeated until a large system of cells is created. One such configuration of cells is shown in Figure 6.1. A simulation was run for 150,000 time steps, corresponding to 15 [T] with the parameters shown in Table 5.2, that resulted in system of 25,951 cells ($\approx 4.7 \times 10^6$ nodes). The population trend of cells over time produced from a single simulation run is shown and compared to exponential growth and logistic growth in Figure 6.3 (a). The fit to Equation 6.1 is

$$N(t) = \frac{25926}{(1 + 630e^{-5.56t})^{1/0.94}}$$

and the exponential fits are $N(t) = 30e^{0.695t}$ at the beginning of the simulation with 25 cells, $N(t) = 176.5e^{0.379t}$ in the middle of the simulation, and finally $N(t) = 725.5e^{0.240t}$ at the end, which stays constant, going past the stationary stage of the logistic fit.

The simulation population value, N , increases rapidly in the beginning since the cells are not in contact during the initial conditions, as shown

in Figure 6.1. The jumps in population number at the beginning of the simulation in Figure 6.3(a) indicate successive doubling of the population number due to the unrealistic initial conditions in the system. However, after two or three generations (each blue point in the plot corresponds to approximately one generation), a trend comparable to logistic is observed. Then the trend becomes exponential at the end, with a constant growth rate. The population trends produced by *CellSim3D* compare favourably to known analytic expressions used to model cell proliferation in the E phase, at least when proliferation is measured with population size. For comparison, we renormalize the population trends by the time to the end of the E phase and the population by the maximum population at the end of the E phase. We assume here that *CellSim3D* simulations *do* saturate for the comparison to be valid. This assumption should be kept in mind since cell growth never stops in *CellSim3D*, though the *growth rate* does decay to a constant (discussed further in Section 6.2.2).

To compare to experimental results, we first ignore all experimental data not pertaining to the E phase. Then we rescale the number of cell at each point in time with the maximum number of cells, which is at the end of the E phase, $N(t) = N(t)/\max(N(t))$, and we rescale time by the time at which E phase ends, $t = t/\max t$. The result is shown in Figure 6.3 (b), and compared to the population trends of mouse cells [237], lung cancer cells [237], and bacteria [422] (*S. typhimurium*). The trends are qualitatively similar for all measurements, though the bacterial trends matches more closely to *CellSim3D* results.

We have observed in this section that the population size in *CellSim3D* simulations compares well with the analytical approximations of growth in the exponential phase, even though there is no cell death modelled in *CellSim3D*. This comparison with experiment is not as favourable, but that is due to the unknown mechanical parameters of the experimental systems. Nevertheless, the comparison holds qualitatively. This is very surprising since all of the cells in the simulation are given the same growth parameters ($(PS)_o$, $(PS)_\infty$, and $\Delta(PS)$) and they have the same stiffness. Real cells must contend with spatial and temporal variations in biological factors such as variations in nutrient concentration, or chemical variations such as pH. The *CellSim3D* model does not account for such terms, so why are similar trends being produced? The answer to this question is explored

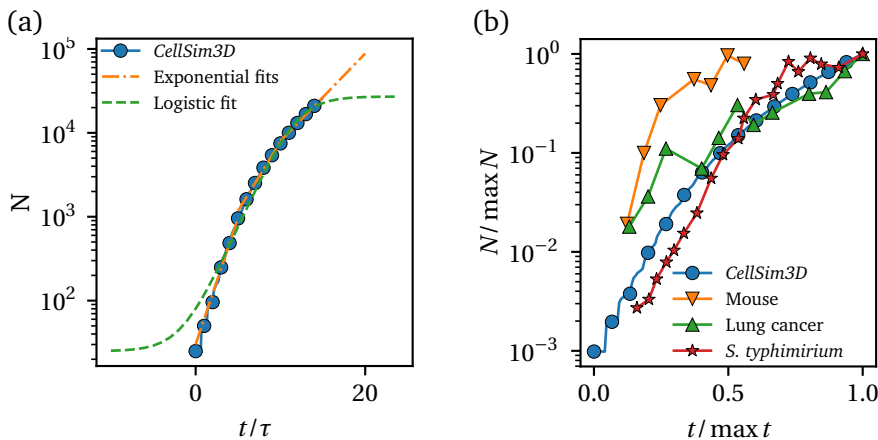


Figure 6.3: (a) Population trend measured with CellSim3D compared to logistic (Equation 6.1) and exponential (Equation 6.2) growth functions. The growth trend emerging from the simulation is not exponential for the whole period of simulation. It matches logistic growth more closely than exponential growth in the E phase. Though it eventually becomes exponential, with a constant growth rate, at the end. (b) The same trend compared to various experimental measurements, rescaled to cancel out differences in length and life cycle times. The comparison is quite favourable to the bacterium case. Data for mouse and lung cancer cells was taken from Ref. [237], and *S. typhimurium* from Ref. [422].

in Section 6.3 after considering two more ways to measure cell growth, system size via radius of gyration and mitotic index.

6.2.2 Mitotic Index

Observing the population trend in time, as we saw before, yields interesting results both theoretically and computationally, and sheds light on the growth dynamics of cellular tissues. Now, we would like to draw attention to the rate of change on the number of cells $N(t)$, the *slope* of the graphs that were shown in the previous section. In biological context, the derivative of N is generally named *mitotic index* [236, 409, 423–428].

The mitotic index, denoted by μ , can be measured over various variables to characterize the reproductive performance of cellular systems, most commonly position, and time. Spatiotemporal variations in mitotic index have been measured in reaction to treatment to cancer treatment [423, 425, 429, 430], presence or lack of growth factor [236, 431], and even in unaltered tissues [238, 432]. We will focus on the temporal derivative of population number

$$\frac{dN}{dt} = \mu(t). \quad (6.3)$$

We know that the derivative above varies with time from the varying slopes in the graphs from Section 6.2.1. It is calculated experimentally as

$$\mu|_{\Delta t_{\text{exp}}}(t) = \frac{N_{\text{mit}}}{N(t)}, \quad (6.4)$$

where Δt_{exp} is the experimental time interval over which the measurement occurs. Typically this corresponds to one cell cycle (τ in the *CellSim3D* algorithm), N_{mit} are the number of cells in some phase of mitosis (the phases are explained in Section 3.3) in that time interval, and $N(t)$ is the number of cells at time t . Wartlick *et al.* [236] measured this mitotic index in their study of the effects of a hormonal growth signal named the Dpp growth factor ¹. Their readings of unaltered mitotic index of a growing *Drosophila*

¹Details regarding this growth factor are not within the scope of this thesis. See Ref. [236]. Ultimately, it is not of significance to the results in this thesis.

(fruit fly) wing disk (an epithelial system) is shown in Figure 6.4 (a). The rate of change of the number of cells (i.e. growth rate) starts at approximately 10 % ($\mu = 0.1$), and decays over time. Ten simulations of *CellSim3D* were configured to simulate epithelia, as described in Section 5.3.1, and the resulting mitotic index average over all simulations is also plotted in Figure 6.4(a). However, since *CellSim3D* does not explicitly simulate all of the phases of cell division, the definition of mitotic index (Equation 6.4) is changed slightly to $\mu(t) = \frac{\Delta N(t)}{N(t)}$, where ΔN is simply the number of cells that are created in the time interval corresponding to τ —the mean time to cell division (Section 5.4).

The characteristic decay of mitotic index can be approximated [300] by

$$\mu(t) = \mu_0 e^{-t/\tau_\mu} + \mu_\infty, \quad (6.5)$$

where μ_0 is the initial mitotic index, μ_∞ is the final mitotic index of the tissue, and τ_μ is the half life time of μ . Thus, we postulate that in tissues where: (1) cell death can be ignored, and (2) the input of nutrients into cells is identical over all cells, the number of cells will change with a rate given by Equation 6.5. A fit to this formulation ($\mu(t) = 0.042e^{-t/0.119} + 0.0054$) is also shown in Figure 6.4(a), where we see good agreement between experiment, simulation, and theory. The same analysis is carried out for a 3D simulation, where cell division is not confined to a single plane. The results are shown in Figure 6.4 (b), and the fit obtained is $\mu(t) = 0.88e^{-t/0.155} + 0.0116$. In both systems, the rate of change of the number of cells remains positive, and decays exponentially to a constant over time.

Note that the first few generations of the system always have a very high mitotic index ($\mu \approx 1$), this is because most of the cells in the first few generations of a new cellular system divide, unimpaired with plenty of space. Hence, the first few generations of cells are ignored for the measurement of μ and fit to Equation 6.5.

It is not obvious, given the formulation of the *CellSim3D* model, why this decay in growth is seen. For real systems, there are myriad factors that can hinder cell growth (health, nutrient rarity, competition between cells, physiological parameters such as temperature, etc.). None are included in *CellSim3D*. This must mean that the observed mitotic index is a purely

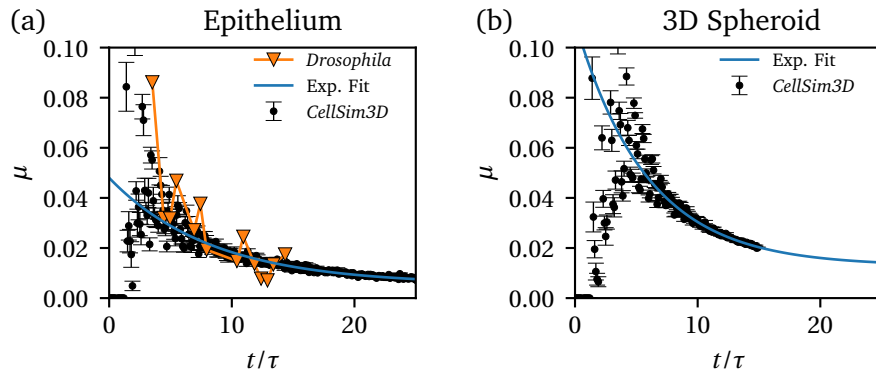


Figure 6.4: Mitotic index measurements for 10 simulations of CellSim3D averaged over ten simulations (black dots) for (a) epithelia, and (b) 3D tissue. (a) Epithelium CellSim3D simulation compared to mitotic index measured by Wartlick et al. [236] of a growing Drosophila wing disc, and fit to Equation 6.5, $\mu(t) = 0.042e^{-0.119t} + 0.0054$. The results from simulation match experimental measurements of Drosophila well. (b) Similar measurement of mitotic index from CellSim3D simulations with a fit of $\mu(t) = 0.88e^{-0.155t} + 0.0116$. An analogous experimental measurement was not found since counting the number of cells in 3D spheroids is difficult, though measurements of cell population at low resolution have been done [433].

mechanical effect as it occurs despite the drivers of growth in *CellSim3D* ($\Delta(PS)$, $(PS)_o$, and $(PS)_\infty$) being constant during simulation. This slowing down of tissue growth must be due to the evolving physical environment of the cells. This will be studied in more detail in Section 6.3.

6.2.3 System size

Thus far, the value used as a measurement of proliferation was the total number of cells in a system, the population. Another approach is the overall size of a system of cells, the radius or diameter of an aggregate of cells—assuming that the whole system is relatively spherical. *CellSim3D* simulations result in approximately spherical systems, unless they are confined to the shape of the simulation box. Studying the size of cellular systems is a standard protocol for assessing the growth [238, 292, 432] and/or health of a colony of cells. In some ways, it is not dissimilar to measuring the population, or mass, trend in cell colonies, but it is still relevant as “size” implies that we are considering a monolithic object that is a single whole such as a colony of interacting cells. Measuring size also takes into account the spatial density of the cells within the system, which is ignored by population models.

We shall compute the size of a system of cells using its radius of gyration, defined as

$$R_g^2(t) = \frac{1}{N} \sum_i^N (\mathbf{x}(t)_i - \bar{\mathbf{x}}(t))^2, \quad (6.6)$$

where N is the number of particles, \mathbf{x}_i is the position of particle i and $\bar{\mathbf{x}}$ is mean position of all of the particles in the system. In our case, we shall take \mathbf{x}_i to be the centre of mass of the i^{th} cell. This method of validation is taken from the work of Radszuweit *et al.* [292], who compared their own 2D and 3D cell model to measurements of radius of the gyration of mouse fibroblast cells carried out by Brú *et al.* [238, 432]. We in turn compare our results to those of Radszuweit *et al.* and Brú *et al.*. Figure 6.5 shows qualitative comparisons between a *CellSim3D* simulation, with parameters shown in the previous chapter in Table 5.2, the 3D model of Radszuweit *et al.*, and mouse fibroblasts. Figure 6.5(a) shows the R_g trend in time, which is qualitatively similar to the model by Radszuweit *et al.* and the

measurements Brú *et al.*. The simulations by Radszuweit are more accurately fitted to the fibroblasts, and they reproduce the most accurate radius of gyration trend. The *CellSim3D* results are not applicable to the exact same fibroblasts studied by Brú *et al.*, but they qualitatively produce similar results. A better match can be obtained when considering the rate of change of R_g with respect to time, \dot{R}_g , rescaled to dimensionless units, in other words the *growth rate* of R_g , which is shown in Figure 6.5(b). The growth rate of R_g matches the data produced by model of Radszuweit *et al.* more closely, although their measurements are offset by a time interval since they ignored the measurements at the start of their simulations [292]. Both measurements show a high \dot{R}_g at the beginning of growth, with a decay to a constant over time. This can also be seen in the slopes of the lines representing R_g measurements of mouse fibroblasts in Figure 6.5 (a). This same effect was seen earlier in Section 6.2.1, albeit with less clarity. The population trends produced by *CellSim3D* did not saturate over time, but its rate of change, \dot{N} , approaches a constant value. Once again, the constant \dot{R}_g over time is surprising since both the *CellSim3D* model and Voronoi-based model of Radszuweit *et al.* [292] do not contain terms for cell death, or any competition for cell growth. The fact that these models can reproduce this growth characteristics is interesting on its own, however there is an opportunity here to study how the *mechanics* of the system can cause this. We know this effect ought to be mechanical since *CellSim3D* does not account for any biochemical factors at all.

6.3 Why does growth rate slow down in a purely mechanical system?

We have observed in the previous sections that as a cell population grows, the ability of cells to reproduce changes. We first observed this in the changing growth rate of cell populations N in section Section 6.2.1, which is slow at the beginning (lag phase), grows to a constant (exponential phase) and decays to zero (saturation phase). Similarly, the rate of change of the radius of gyration, \dot{R}_g (Section 6.2.3), is low at the beginning and grows to a constant over time. The traditional biological notion as to why

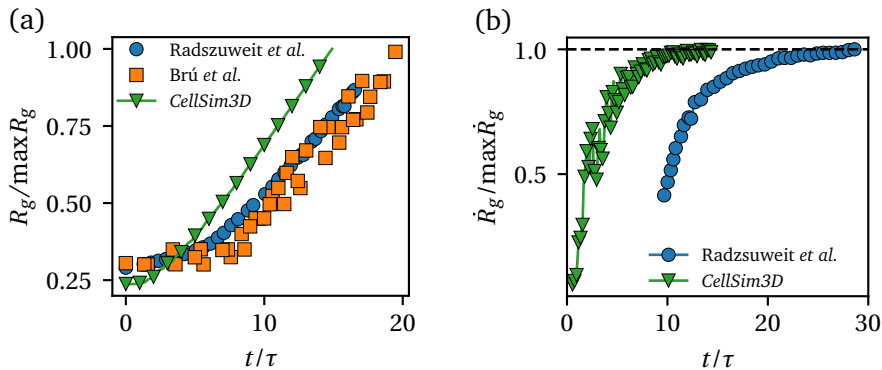


Figure 6.5: (a) Trends in radius of gyration R_g measured for a Voronoi based 3D cell model by Radzsuweit et al. [292], and samples of mouse fibroblasts measured by Brú et al. [238, 432], compared to the radius of gyration trend in a CellSim3D simulation with the parameters in Table 5.2. The graphs are qualitatively comparable between the three cases, though the model by Radzsuweit et al. is more tuned to the experiment. (b) Comparison of the slope of the measurements in (a) ($R'_g = \frac{dR_g}{dt/\tau}$)—an approximation of the growth rate of the system. The growth rates are comparable between the two systems, accounting for the offset in the data from extracted from the work of Radzsuweit et al. [292]. They chose to ignore the first few data points from their simulation.

this occurs is due to the rarefaction of nutrients over time [11, 410, 411]. But why do we see the same phenomenon in a purely mechanical model, such as *CellSim3D*? We pose that the evolving mechanical environment of the cells is what drives this decay in growth rate in *CellSim3D*, and it plays a vital role in the decay of growth rate in real cellular systems. We will investigate the mechanical environment of the cells by measuring the changes in density and number of nearest neighbours.

6.3.1 Density

At the beginning of the simulation, cells have space to be able to grow without any hindrance from their neighbours. Over time, however, their environment becomes crowded due to the increasing numbers of neighbouring cells. Growing cells have to push neighbouring cells away to be able to grow. This crowding can be quantified with a simple measurement that is meant to approximate the density of cells in the system. We shall estimate the density of the system, which evolves over time as the cells grow as

$$\rho(t) = \frac{N(t)}{(R_g(t))^3}$$

for 3D tissue and

$$\rho_{2D}(t) = \frac{N(t)}{(R_g(t))^2}$$

in epithelia. For easy comparison, and to remove all effects of length scales in the system, the density is renormalized with respect to the maximum density achieved in the system to

$$\rho_0 = \frac{\rho(t)}{\rho_{\max}}.$$

We then monitor how ρ_0 changes over the simulation as tissues grow. In both the 3D and epithelium cases (Figure 6.6), ρ_0 increases to 1 as μ decays to μ_∞ . As tissue grows, cells fill the space between each other and eventually crowd their neighbours. Over time this limits cell growth in the centre of the system until most of the growth is happening on the surface

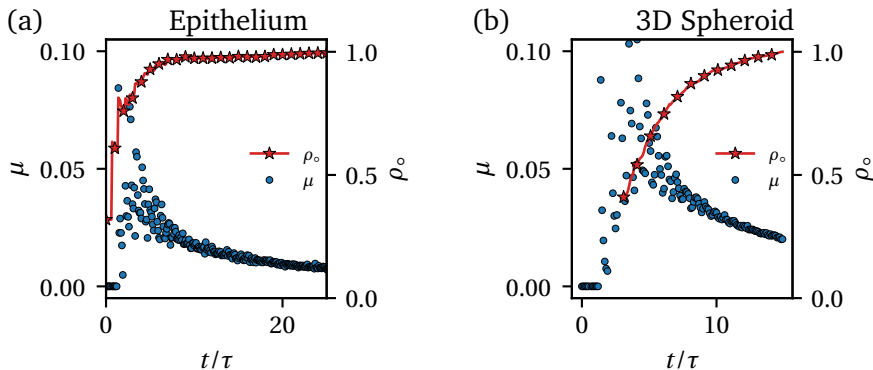


Figure 6.6: Rescaled density ρ_0 , compared to the mitotic index measurements from Section 6.2.2 for (a) an epithelium, and (b) a 3D spheroid. Mitotic index is strongly correlated with the density in the system.

(or the perimeter in epithelia). From this point on-wards, density and growth rate are more or less constant. The slowing down of growth due to an increase of density is well established in multiple cell cultures [308, 432, 434–438], though it is most often associated with reduction in biochemical factors related to cell-cell contacts [434–438]. This effect has also been demonstrated with other mechanical cell models [439, 440].

As density increases to its steady state ($\rho_0 = 1$), growth occurs near the edge of the sample. This is quantified in Figure 6.7 which shows histogram of the distance from the centre of the tissue (a disk in epithelia and a spheroid in 3D) versus simulation time. In both cases the distribution of division events is spread from the edge towards the centre at the beginning of the simulation. Over time, the local density in the vicinity of each cell increases and slows down cell growth. By the end of the simulation growth is mostly concentrated at the outer edge of the tissue, and halted in the centre. The location of growth being the outer edge of tissues is a well known biological fact [4, 11, 432]. The biological (and chemical) reasoning for *why* it occurs is that the nutrients in the interior of tissues are being depleted as new cells are created and more time is needed for nutrients to diffuse inwards. While that is certainly *one* of the factors for the slowing down of growth, it is clearly not the *only* factor. The evolving mechanics in the system play a crucial role alongside other biochemical

factors in slowing down cell growth in cellular systems.

6.3.2 Number of Nearest Neighbours

Evidence from the previous section suggests that the reduction in growth rate is purely due to increase in density. Here the number of neighbours is used as another way of measuring crowding. This also serves as further validation for the *CellSim3D* model as the number of nearest neighbours has been measured experimentally for epithelia [441].

Sandersius *et al.* [441] compiled a number of experimental measurements of nearest neighbours (N_n) in epithelial systems (shown in Figure 6.8). Note that the proportion of cells with each value of N_n is basically the same between species. This suggests that even if the epithelial tissue taken from different species are biologically very different, they may be mechanically quite similar. Sandersius *et al.* showed that this may be the case by comparing to the results of their own computational study with the topological model of Gibson *et al.* [278]. Here we do the same with *CellSim3D*. The number of nearest neighbours measured from simulation trajectories serves as: (1) another measurement for crowding, (2) more validation for the *CellSim3D* model.

Figure 6.8 shows the distribution of N_n in a variety of epithelia from various species compiled by Sandersius *et al.* [441]. The cells are biologically quite different as they come from different species. Why is a similar distribution seen for all of them? When considered from a mechanical perspective, most cells have approximately the same structure (explained in Section 3.2) from which they derive their mechanical properties [38, 442–444]. They are constructed of a cell membrane and cytoskeleton, which are themselves composed of three kinds of fibres material: microtubules, intermediate filaments, and actomyosin. The mechanical properties of the fibres have been measured experimentally and do not vary greatly between species [19, 198, 444, 445]. We hypothesize that the packing of cells in this system should be reproduced in a purely mechanical system. To test this hypothesis, ten simulations were run with *CellSim3D* that were set to simulate epithelia (as described in Section 5.3.1). Figure 6.1 shows one such simulation. The epithelial plane is assumed to be parallel to the XY plane. The number of nearest neighbours were measured by conducting a Delaunay triangulation [296] on all of the centres of mass of the

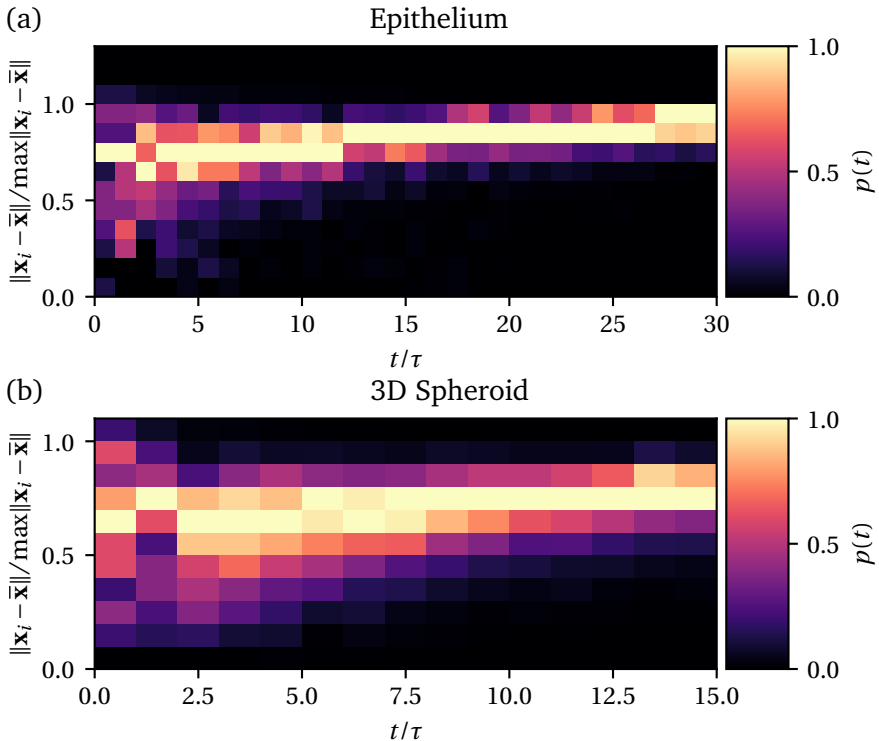


Figure 6.7: Evolution of the distribution of division events from the centre of the cellular masses to the edge. \mathbf{x}_i denotes centre of mass of cell i , and $\bar{\mathbf{x}}$ is the centre of mass of the whole system. (a) Epithelium (b) 3D spheroid. $p(t)$ is renormalized to be 1 at its maximum. In both cases, the growth is more spread out throughout the tissue at the beginning of the simulation and concentrates more at its edge over time.

cells. Delaunay triangulation is done as follows. Let the centres of mass of all of the cells in the system be considered as nodes in a plane—which is true for flat epithelia. Delaunay triangulation is an algorithm that places edges between the nearest neighbours of each node. This triangulation outputs a graph in which cells that are “first shell” neighbours are connected with an edge. Then, the neighbours of each cell are counted by counting the number of edges at each node. See Ref. [296] for a detailed description of Delaunay triangulation. The resultant graph of the triangulation is the dual of a Voronoi triangulation in 2D. The number of nearest neighbours additionally serves as measurement of crowding.

The results of Delaunay analysis for the output of a *CellSim3D* simulation is shown in cross-hatched bars in Figure 6.8. It compares the number of nearest neighbours (N_n) between simulation and experimental measurements of epithelia compiled by Sandersius *et al.* [441]. This was shown already by Mkrtchyan *et al.* [43] with a purely 2D model, and it is reproduced here as validation for, and a measure of the flexibility of, *CellSim3D*. As can be seen in Figure 6.8, N_n values that were measured experimentally have been reproduced here by a purely mechanical model, suggesting that this phenomenon is due to primarily the mechanics of the cellular system. This was already shown before by multiple other studies with the help of other 2D mechanical models [278, 279, 441, 446].

For comparison, the same analysis was done for points placed randomly and uniformly in a plane, with at least a distance of one unit between points. N_n measurement for the random case is also shown in Figure 6.8, lime green. The fractions of cells at $N_n = 5$ and $N_n = 7$ are the same for experimental measurement, *CellSim3D*, and for randomly distributed points, but different for other values of N_n . This is due to the attractive nature of the interaction between cells that favours a nearest neighbour count closer to 6, which is the same for maximizing density of hard spheres. The randomly distributed points do not attract each other, so the distribution of N_n in the random case distribution is not similar.

The obvious question to ask here is: What about in 3D? The same nearest neighbour measurement can be carried out for the 3D tissue, and another distribution of N_n emerges. Figure 6.9 shows N_n measured for 3D simulated tissue (green downward triangles). The number of neighbours are distributed approximately in a log-normal distribution, which is given

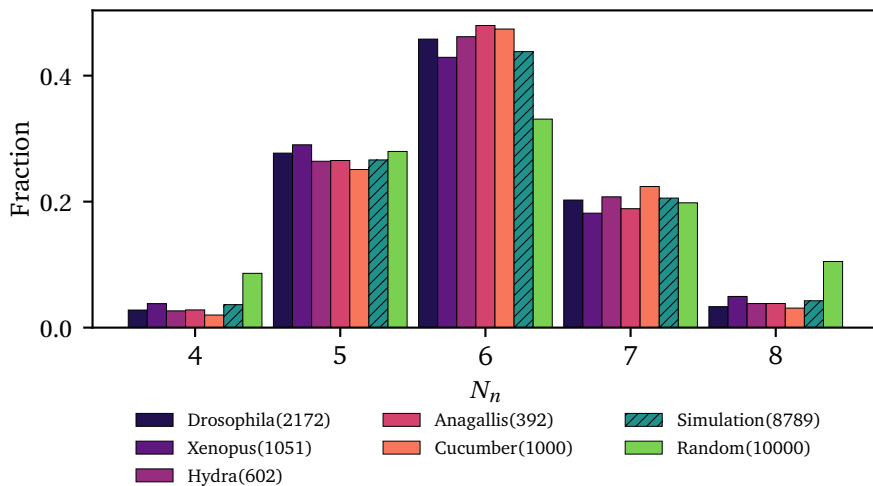


Figure 6.8: The number of nearest neighbours obtained after simulating an epithelium with CellSim3D compared to various experimental measurements compiled by Sandersius et al. [441]. The cross-hatched bars are from a CellSim3D simulation. The same distribution as experiment is produced. Finally, simulation and experimental data is compared to number of nearest neighbours of randomly generated points with a spacing of one unit between points. The type of distribution of the random system is perhaps comparable (with the same asymmetry at $N = 5$ and $N = 7$), but that is where the similarity ends.

by

$$p = \frac{1}{N_n \sigma \sqrt{2\pi}} \exp\left(-\frac{(\ln N_n - N^*)^2}{2\sigma^2}\right) \quad (6.7)$$

where p is the fraction of cells with number of nearest neighbours N_n , the mean number of neighbours is given by $\exp(N^* + \frac{\sigma^2}{2})$ and the variance is given by $[\exp(\sigma^2) - 1] \exp(2N^* + \sigma^2)$.

The number of nearest neighbours in Figure 6.9 is approximately log-normal with mean of approximately 15 neighbours, and variance of 3.63. The appearance of a log-normal distribution of N_n is an indication that the filling of space with new cells is a multiplicative process [447]. At any given time there is some percentage of cells that divide (as measured by the mitotic index in Section 6.2.2), all the new cells then occupy additional space and the overall average empty space around cells is reduced. This multiplicative reduction in space could be the reason why the log-normal distribution of N_n is observed. A simple way to verify this measurement would be to compare to experimental results, since experimental distributions of 2D systems (epithelia) are reproduced readily by *CellSim3D* (Figure 6.8). To the best of our knowledge, N_n has not been measured experimentally for 3D cellular systems. It can be measured trivially with computational methods such as *CellSim3D* since the Delaunay triangulation method can be applied in 3D as well. We instead compare our N_n results to N_n measurements in emulsions, since the *CellSim3D* cells at the end of the simulation can also be considered as a packing of soft spheres with friction between them. The packing of jammed emulsions in 3D was measured by Clusel *et al.* [448, 449] and their findings are compared to *CellSim3D* results in Figure 6.9 (purple dots). The distribution that was found by them is also approximately log-normal (Equation 6.7), though with different mean and variance (14 and 14.55 respectively). This measurement suggests that number of nearest neighbours distributions could be of the same family in systems of soft spheres, and for 3D cellular spheroids the distribution is narrower and higher. The emulsion in the work of Clusel *et al.* [448] does not have as much adhesion between the bodies, which could be reason behind the different distributions. Furthermore, the mechanical properties (e.g. stiffness) of the emulsion may also incomparable to the *CellSim3D* simulation. N_n for 3D cells is also

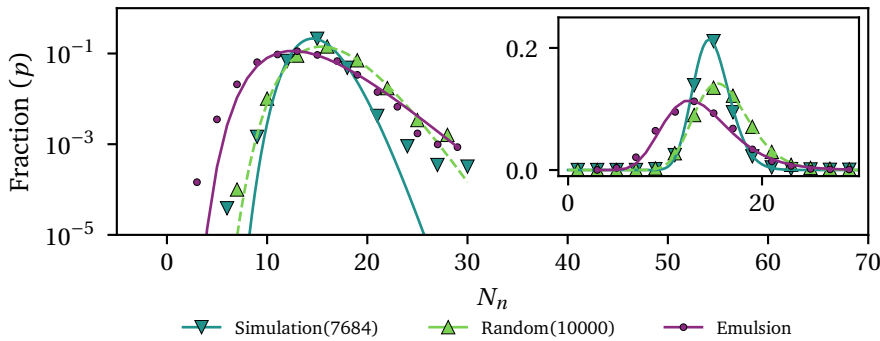


Figure 6.9: Number of nearest neighbours measured for a simulated 3D tissue of cells (downward triangles), randomly placed points (upward triangles), and experimental measurement of packing in an emulsion from Ref. [448] — though their systems are polydisperse (data extracted with WebPlotDigitizer [450]). Inset shows the distributions in linear scale y-axis. This distribution is log-normal (Equation 6.7) with mean of 15 neighbours, variance of 3.63. Comparison with experimental measurement of Clusel *et al.* [448] indicates that the approximately log-normal distribution of soft spheres in 3D is a multiplicative process.

compared against a random collection of points in 3D, placed such that a spacing of 1.0 is guaranteed between points. This is, again, a multiplicative process as the fraction of space being filled is reduced with the addition of each new point. Again an approximately log-normal distribution (mean 16, variance 8.6) is found suggesting a multiplicative space filling process may be valid for multiple types of systems of soft spheres. The difference is once again due to the interaction between the different cells and the medium. We hypothesize that a collection of measurements of N_n , similar to those compiled by Sandersius *et al.* [441] but for 3D tissue, will yield a similar distribution of nearest neighbours that is conserved between species. Experimental measurement of spheroidal tissues are needed to confirm this.

It has been shown before [43] that N_n approaches a steady state as tissue grows; it converges over the course of the simulation. A simple scalar value can be defined that quantifies how close the system of cells is to the final distribution of N_n , as follows. Assume that the number of neighbours is always some value between 1 to 25. Then vector \mathbf{N}_n can be defined with the components being the proportion of cells (p) with the

corresponding number of neighbours as

$$\mathbf{N}_n := (N_n(1), N_n(2), \dots, N_n(25)),$$

$\mathbf{N}_n \in \mathbb{R}^{25}$ in general. Neighbours counts higher and lower than the range of possible values for epithelia (3-8) are set to 0 for epithelial systems (in fact this is done automatically by the triangulation algorithm). The system of growing cells will have an evolving \mathbf{N}_n that converges to the vector \mathbf{N}_o over time, i.e. $\mathbf{N}_o = \lim_{t \rightarrow \infty} \mathbf{N}(t)$ and corresponds to the coordination measurements shown in Figure 6.8 and Figure 6.9.

The deviation, ε , from this \mathbf{N}_o distribution is defined as

$$\varepsilon(t) = 1 - \frac{\|\mathbf{N}(t) - \mathbf{N}_o\|}{\max\|\mathbf{N}(t) - \mathbf{N}_o\|}, \quad (6.8)$$

i.e., the maximum distance between instantaneous number of neighbour distribution $\mathbf{N}_N(t)$ is the highest at $t = 0$. The Euclidean norm is indicated by $\|\cdot\|$. ε approaches 1 as the system grows. The coordination is at a steady state when $\mathbf{N}(t) = \mathbf{N}_o$ and $\varepsilon = 1$ at the end of the simulation. Thus, ε is a way to measure the maturity of the system of cells and a simple number to quantify the difference between tissue structure when tissues are young (start of the simulations, little crowding) and old (end of the simulations, high crowding).

Figure 6.10(a) shows how ε changes for the two systems as a function of the effective density ρ_o . As density approaches its steady state, the distribution of N approaches its steady state ($\varepsilon = 1$). A sensible result as one would expect number of nearest neighbours to be correlated to an increase in density. The space around each cell is filled with the highest possible number of neighbours at highest density. The two are proportional to each other, but the constant of proportionality is higher for epithelia than for 3D tissue. This is because epithelia do not have as much freedom to grow and they necessarily react to increasing density more strongly than 3D tissue, which have more space to expand into.

We can now study how the *growth rate* (mitotic index) of the tissues varies with the *structure* of the tissues, or the increase in number of neighbours. Figure 6.10(b) shows how mitotic index varies with ε . At low coordination ($\varepsilon \approx 0$), growth occurs at its initial high value $\mu = \mu_0$. It then continues to decrease proportionally to the increase in ε (which indicates

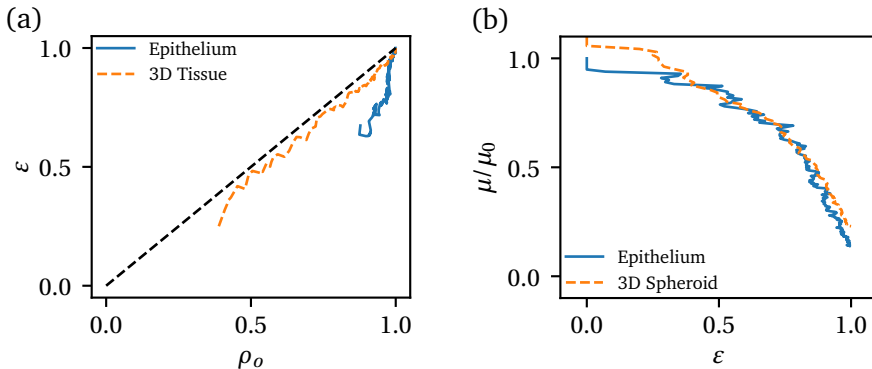


Figure 6.10: The trends of ϵ , the deviation of the measured number of nearest neighbours from its final distribution shown in Figures 6.8 and 6.9, and the relative change in mitotic index μ , the mitotic index as a function of ϵ . (a) The number of neighbours approaches its steady state as density increases to its steady state. In other words the nearest neighbour distribution approaches its steady-state distribution over time, since we know that density increases to its steady state from Figure 6.6. The undulations at the beginning of the data are due to the unhindered growth of cells at the beginning of simulations. (b) The mitotic index is highest when $\epsilon = 0$, before the system has reached its steady state nearest neighbour distribution. It then decreases to its minimum (μ_∞), where it remains, implying that cells with neighbours tend to grow less and the distribution of the number of neighbours converges to a constant distribution (see Figure 6.8 and Figure 6.9).

more crowding), until the critical value of $\epsilon \approx 0.8$. After this point, growth decays much faster and eventually converges to about 15 to 20% its original value ($\mu/\mu_0 \approx 0.2$).

The results in Figures 6.8, 6.9 and 6.10, combined with the results in Figure 6.4 from Section 6.2.2, provide ample evidence that cell growth and the physical environment of cells are directly related, and this relationship still persists even in a purely mechanical model where all biochemical factors are assumed to be constant between cells.

6.4 Effects of Friction on Tissue Growth and Structure

The connection between growth, structure, and density was described in the previous section with various measurements of growth rate (via mitotic index). In this section, we shall consider the effects of intermembrane friction and medium friction on the mitotic index and on the distribution of the number of nearest neighbours. Since the relationship between tissue structure, density and growth is qualitatively similar between epithelial and 3D tissues, we shall only consider three dimensional tissues in this section.

The two parameters γ_{ext} and γ_m set the strength of intermembrane friction and medium friction respectively in *CellSim3D*. An increase γ_{ext} would hinder the motion of cells past each other and could perhaps affect the number of neighbours, and therefore growth. Since γ_m slows all motion in the system, one would expect growth to slow down as well. An increase in γ_m simulates a more viscous medium or a medium that interacts more strongly with the adhesion molecules in the cell membranes (Section 3.2.1).

Let the fit to the mitotic index measured in Figure 6.4(b) be our reference, which we denote as $\mu'(t)$, measured with parameters shown in Table 5.2, and $\gamma_{\text{ext}} = 1$ and $\gamma_{\text{int}} = 1$. Its mitotic index function (Equation 6.5) is denoted $\mu(\gamma_{\text{ext}} = 1, \gamma_m = 1, t) = \mu'(t) = \mu'_0 e^{-t/\tau'_\mu} + \mu'_{\infty}$, with parameters $\mu'_0 = 0.088$ (reference starting mitotic index), $\tau'_\mu = 0.155$ (reference decay half-life), and $\mu'_{\infty} = 0.0116$ the reference final mitotic index. We then measure the resulting mitotic index at increasing values γ_m and γ_{ext} and then compare them to the reference mitotic index. With that we shall have an idea of which parameter has the stronger influence on growth and to what degree an increase in the parameter influences growth.

Ten simulations at γ_{ext} and γ_m values ranging from 1.0 to 10.0 were run, their mitotic indices measured, and compared to $\mu'(t)$. The results of this analysis are shown in Figure 6.11. All of the systems result in trends of mitotic index of the same form shown in Equation 6.5, but with different dynamics in each case. The dashed line in the figure is the $\mu = \mu'$ line ($\gamma_{\text{ext}} = 1$, and $\gamma_m = 1$). The coloured bars beside the graphs show increasing γ_{ext} (violet to yellow) and γ_m (dark red to white). Intermembrane

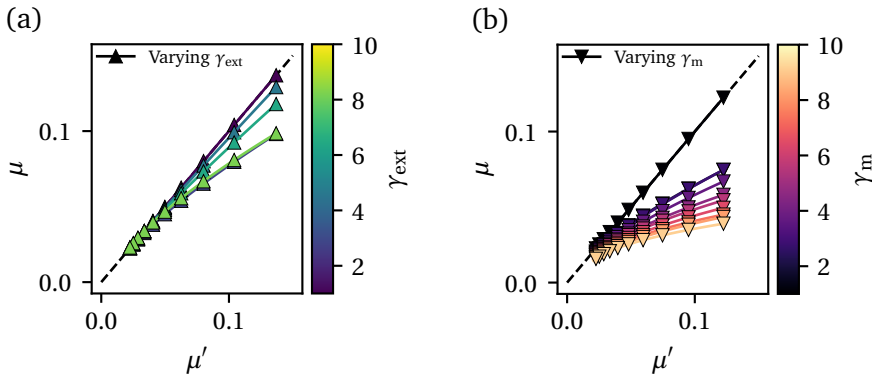


Figure 6.11: Mitotic index of systems with varying (a) γ_{ext} (intermembrane friction) and (b) γ_m (medium friction) plotted against the reference case of $\mu' = \mu(\gamma_{\text{ext}} = 1, \gamma_m = 1, t)$. The dashed line indicates $\mu = \mu'$. The two colour bars are for (a) increasing γ_{int} and (b) γ_m respectively. Mitotic index does not vary much over changes in γ_{ext} , the intercellular friction coefficient. In contrast, γ_m , the medium viscosity, has a profound effect.

friction has a smaller influence than medium friction, though both slow growth significantly. The effect is quantified further in Figure 6.12(a), where we plot how the initial (μ_0) and final (μ_∞) mitotic index changes with respect to the reference at different values of γ_{ext} and γ_m . Higher friction always results in slower initial and final growth, but increase in medium friction, again, has a greater effect. Medium friction acts on all nodes in the simulations, i.e. all parts of the cell membrane, equivalently and simultaneously since viscous drag acts on all points with the same coefficient (γ_m), whereas intermembrane friction is only between those membranes that are within attraction range (intermembrane distance smaller than the attraction range R_0^A). The term for intermembrane friction in the force field (Section 5.2.2) arises from averaging the interactions between Cell Adhesion Molecules (CAM) between cells. We know from experimental measurements [182, 378, 451] that these interactions can be dynamic and variable in strength. The dynamic nature of these interactions may play a vital role, but they are not captured by *CellSim3D*.

On the other hand, the decay from μ_0 to μ_∞ , quantified by the mitotic index half-life τ_μ in Figure 6.12(b), is *slower* at higher friction coefficients. While the mitotic indices are lower over all at higher friction, they remain

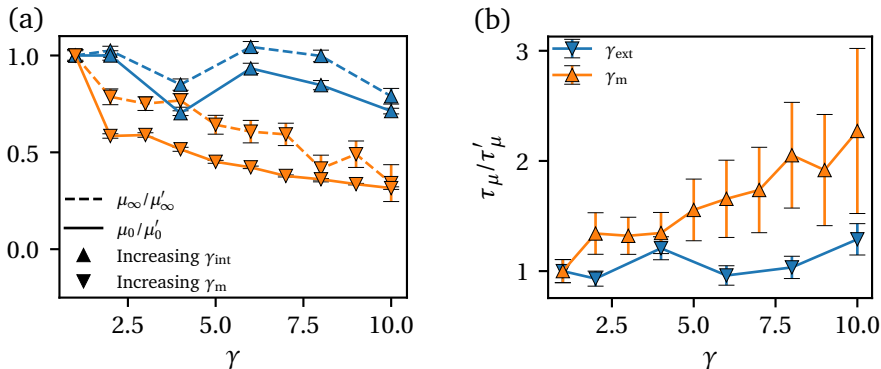


Figure 6.12: (a) Change in initial mitotic index relative to reference (μ_0/μ'_0), and final mitotic index relative to reference (μ_∞/μ'_∞) (b) Change half life of mitotic index decay (τ_μ/τ'_μ). In both cases, γ_{ext} does have an affect, but it is lower than γ_m , which hinders growth much more.

above their steady state values for longer. This could be because μ_0 is already quite close to the final steady state, so there is smaller driving force towards a lower mitotic index. The error bars in Figure 6.12(b) are higher at higher friction coefficients, hinting at insufficient statistics in this case.

With the same simulation data as before, we also have all the tools to analyze the effects of friction on the final structures of tissues. It stands to reason that the level of interaction between cell membranes of different cells would affect how the cells are placed near each other. We begin by defining another measure for the deviation of nearest neighbour distributions from the reference state at $\mathbf{N}_n(\gamma_{ext} = 1, \gamma_m = 1) = \mathbf{N}'_n$ as

$$\varepsilon_\gamma = 1 - \frac{\|\mathbf{N}_n(\gamma_{ext}, \gamma_m) - \mathbf{N}'_n\|}{\|\mathbf{N}'_n\|},$$

where the vectors \mathbf{N}_n are the steady state of $N_n(t)$ at the corresponding γ_{ext} and γ_m . $\varepsilon_\gamma = 1$ means no change from reference. Figure 6.13 shows ε_γ measured at increasing levels of γ_{ext} and γ_m . Dashed lines are simulation results, and solid lines are linear fits to the data. Both γ_{ext} and γ_m alter the N_n attained by the cells, but medium friction has a greater effect (by a factor of approximately 3). This is due to the short-range transient nature

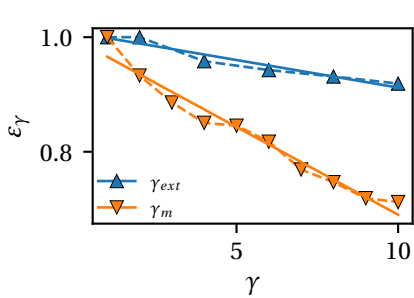


Figure 6.13: $\varepsilon_\gamma = 1$ indicates a perfect match with the distribution of number of neighbours (N) at $\gamma_{ext} = 1$ and $\gamma_m = 1$. Dashed lines mark simulation data, and solid lines linear fits to them. The fits are $\varepsilon_\gamma = -0.01\gamma_{ext} + 1$ and $\varepsilon_\gamma = -0.03\gamma_m + 1$. Both intermembrane friction (γ_{ext}) and medium friction (γ_m) alter the coordination levels attained by the cells, but medium friction has a greater effect.

of intermembrane friction (as it is currently approximated in our model). Ultimately, altering the degree to which cells interact does affect their nearest number distribution, and therefore tissue structure, provided the medium is kept the same.

This disruption of structure could perhaps be alleviated by an active driving force in the cells that rearranges and deforms the cytoskeleton to optimize the contact with other cells—something that is missing in the *CellSim3D* model. The most straightforward way to implement this would be to introduce a random term in the force field, akin to a Langevin type system. Adding a term that simulates the active reshaping and rearrangement that cells exhibit, such as those that cells use to migrate (Figure 1.1), could lead to different and more preferred distributions of nearest neighbours. More details of such a random force are discussed in Chapter 7.

6.5 Conclusions

In this chapter we showed how *CellSim3D* can be used to measure growth in cellular systems. We compared the growth produced by *CellSim3D* against three methods of measuring growth: population trends, population growth rate (mitotic index), and finally system size. In all of the three cases, we showed that trends comparable to known results were produced. *CellSim3D* was created to be a general purpose and flexible model that can be used to study various aspects of cell behaviour simultaneously. We demonstrated we are able to reproduce various types of growth data without modifications of *CellSim3D*.

We went even further by making connections between the slowing down of growth in cells, and tissue density and structure. Real biological cells are known to slow their growth over time, which was thought to be due to the higher scarcity of nutrients as the tissue grows. The same behaviour is observed with *CellSim3D*. We later observed that the reduction in growth rate is due to the evolving mechanical environment of cells. Both the evolving structure of tissue and the lack of available space to grow play major roles in the growth rates of tissues in addition to nutrient scarcity.

We also demonstrated the connection between cell growth and the mechanical properties of cells by seeing how increasing intermembrane friction between cells reduces overall growth rate and how it is slowed down more severely when the friction with the medium is stronger. Although the strength of interaction between cells is crucial in determining their proliferation, the strength of interactions between cells and their environment is the dominant factor.

In pursuing the answers to the questions summarized above, we have also validated the *CellSim3D* model, as a flexible method that can be used to study cell behaviour from a multitude of perspectives. We are convinced that it will be a useful tool in probing other questions of mechanobiology.

Chapter 7

Summary and Outlook

In this thesis, we considered the problem of mechanotransduction: the interplay between the biochemical processes within cells (e.g. metabolism), the mechanical properties of cells, the medium that they are in, or physical stimuli acting on the cells. Experimental techniques often can only measure macroscopic properties. They offer a zoomed out view that makes it difficult to draw conclusions regarding the underlying physics. Furthermore, ensuring controlled experimental conditions, such as identical cell stiffness or equal provision of nutrition is impossible in experiments. Computational methods that aim to bridge the underlying biophysics to experimental observables are vital tools in gaining insight about mechanotransduction. The work described in this thesis aims to introduce such a model with *CellSim3D* [42].

CellSim3D uses the algorithms developed for molecular dynamics (MD) to simulate cells in 3D in a coarse grained (CG) model. We briefly summarized the basics of atomistic MD, and how it can be extended to study larger systems with CG methods in Chapter 2. Of particular interest was the discussion of the degrees of freedom used in MD, which inspired the *CellSim3D* force field.

We provided a short general introduction to cell biology in Chapter 3 and focused on the *mechanical cell* as well to describe the mechanical properties of cells, and how they can be simulated. The mechanical cell is then used to develop our model. For context, we reviewed a few cell models available in the literature in Section 3.4. Many of the models available

currently either make too many simplifications of cell structure such that they obscure the dynamics of cell membranes, or do not have efficient implementations in fast software. One of the models we introduced, named CeDEM (Section 3.6.5), is able to simulate growth, membrane dynamics, and growth of cells with different stiffness and intermembrane friction in 2D. We used CeDEM to study the morphology of different 2D tissues in Chapter 4. In that chapter, we saw that cell growth was slowed down at higher intermembrane friction and that softer cells constrict stiff cells into unfavourable conformations. We also noted that the forces are highest in the system at the boundary between stiff and soft cells. CeDEM is, however, a 2D method so it can only be applied to 2D systems of cells. There was a need in the field of a 3D model for cells with the ability to simulate forces at subcellular length scale, while describing the correlations between growth, cell mechanics and structure. Additionally, since the aim was to study large collections of cells and their properties, the model would have to be implemented in an efficient software package that can be used on the average workstation.

The desire to meet the two goals above resulted in the creation of the *CellSim3D* [42] package and simulator. *CellSim3D*, extends the 2D CeDEM model into 3D, is a new flexible models for cells with an open source software package released on github <https://github.com/SoftSimu/Cell-Sim3D>. The details of the force field and the software package were discussed in Chapter 5.

CellSim3D was then used to reproduce a number of results known from literature in Chapter 6. We were able to correctly predict the growth trends in population, population growth rate, and system size with the same model for both epithelia and 3D systems. We also analyzed *why* growth slows in such systems. The biological argument for the reduction in growth over time is that the level of nutrition available for the cells is depleted over time, due to either diffusion or competition with other cells. Our results showed that even in systems where cells are given identical growth potentials (approximated in *CellSim3D* with the rate of increase in internal pressure), the growth slows down due to mechanical effects. We later showed in Section 6.3 that the crowding of the cellular system drives the decay in growth rate. We measured the crowding by measuring the distribution of density and the number of nearest neighbours in

Section 6.3.1 and Section 6.3.2.

Since the distribution of number of nearest neighbours is known for epithelial systems, we used *CellSim3D* to reproduce the distribution for those systems. We also used it to make a prediction about the nearest neighbour distributions of 3D tissues which has not been measured experimentally yet. Then we showed that the evolving mechanical properties (density and structure) of the cellular systems play a key role in determining the growth dynamics, even if all cells are given identical growth forces. Finally, we also demonstrated how the model can be used to study the growth trends and nearest neighbour distributions of tissues with different intermembrane and medium friction coefficients.

In the process of comparing data produced from *CellSim3D* to known experimental and theoretical results, we also validated the model and implementation of the software. However, recall that we made several assumptions during the development of the model, see Section 5.1 for details. Some of these assumptions could be lifted to add features to *CellSim3D*, and we describe such extensions here. Since the simulator is based on CG MD, we can use its framework and add new potentials and/or degrees of freedom to extend the model. Additionally, the software implementation is such that new terms can be added to the force field.

Below, we discuss three possible extensions to *CellSim3D* to simulate heterogeneous cell mechanical properties, asymmetric cell division, and directed migration. The state of a cell in *CellSim3D* is determined by its position. We first propose that another parameter be added to the cells: cell polarity. Polarity can then be used to add terms in the force field for cell heterogeneity, which would make cell-cell interactions and mechanical properties non-isotropic. Next, we reuse the cell polarity defined before to propose a framework for directed cell migration. The notation from Chapter 5 and definitions of the parameters of *CellSim3D* are taken from Table 5.2. Finally, we discuss possible extensions to simulate asymmetric cell division.

Heterogeneity in the Mechanical Properties of Cells

We have assumed before that the distribution of the Cell Adhesion Molecules (CAMs) is always uniform over the surface of cells. However, this is not always the case, the distribution of CAMs on cell surfaces need not be uniform. The heterogeneity of the distribution of CAMs, structure, and functionality of cells is dependent upon cell polarity [452–454]. A cell is considered to be polarized when there is an asymmetric distribution of proteins or structures that span the cell. As a result the mechanical properties of polarized cells, and their interaction with other cells, can change depending on direction. Many phenomena, such as cell migration [455], cell differentiation [456], and even division [457] by cell polarity.

The simplest way to introduce polarity in *CellSim3D* is to define a polarity vector $\hat{\mathbf{p}}_m$, for cell m . The properties of m can then depend on this vector. This is a common approach to introduce polarity in cell models such as Vertex models [284] or the Cellular Potts Models [458].

For example, consider the intermembrane force terms in the *CellSim3D* force field as described in Section 5.2.2. These terms aims to describe the adhesion, repulsion, and friction between cell membranes. A simple spring force was used to model the attraction of the nodes of different cells to each other. The adhesive spring force acting on particle i in cell m , due to some other particle j in another cell is given by

$$\mathbf{F}_i^A = \begin{cases} k^A(r_{ij} - R_o^A)\hat{\mathbf{r}}_{ij} & \text{if } r_{ij} < R_o^A, \\ 0 & \text{if } r_{ij} \geq R_o^A. \end{cases} \quad (7.1)$$

where k^A is the adhesion spring constant, R_o^A is the spring equilibrium and cut off length, and \mathbf{r} is the vector pointing from i to j . So far we have assumed k^A to be a constant in our simulations for all nodes i . Instead, we can make it depend on the orientation of node i in the cell. Let $\mathbf{r}_i = \mathbf{x}_i - \bar{\mathbf{x}}_m$, $\bar{\mathbf{x}}_m$ being the centre of mass of m , then we can replace the spring constant k^A with $k^{\text{inter}} = k^A(\hat{\mathbf{r}}_i \cdot \hat{\mathbf{p}}_m)$. The result will be an adhesive or repulsive spring that varies over the surface of the cells augmenting it with a polarity, see Figure 7.1. The formulation for the adhesion terms described above would make intermembrane forces attractive if operating along the polarity vector, or repulsive if operating opposite to it, with a smooth transition between the two regimes.

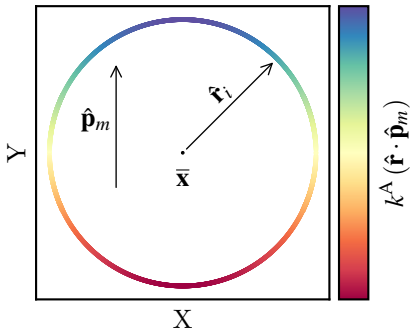


Figure 7.1: An approximation for cell polarity. The spring becomes attractive (blue) or repulsive (red) over the surface of cells. The quantity $\hat{\mathbf{r}}_i \cdot \hat{\mathbf{p}}_m$, can be used to vary many other mechanical properties such as intracellular bond stiffness and friction coefficients.

The introduction of a new polarity vector above would induce heterogeneity that is linear along the vector, as shown in Figure 7.1. One can introduce non-linear heterogeneity by instead proposing a more complex dependence on the polarity vector ($k^{\text{inter}} = k^A f(\hat{\mathbf{r}}_i \cdot \hat{\mathbf{p}}_m)$), or even introduce two polarity vectors $k^{\text{inter}} = k_1^A f_1(\hat{\mathbf{r}}_i \cdot \hat{\mathbf{p}}_m^1) + k_2^A f_2(\hat{\mathbf{r}}_i \cdot \hat{\mathbf{p}}_m^2)$, where the adhesion term is a linear combination of two functions of the orientation of each cell node with respect to the polarity vector. This would allow the study of cells with different distributions of adhesion molecules in 3D.

This same extension can be applied to the other parameters as well, such as the intermembrane (γ_{ext}) and medium friction coefficients (γ_m), or the stiffness in the other parts of the force fields such as bond stiffness k^B .

Directed Cell Migration with *CellSim3D*

The *CellSim3D* simulator makes use of the DPD-VV (Section 5.2.3) algorithm to calculate the motion and growth of the cells in the system. However, we assumed that there are no random displacements in *CellSim3D*. Once a cell is created, it is static as the medium and intermembrane friction terms damp all motion in the system. However, it has been shown that certain cell types exhibit migration [459–461] and which plays a vital role in the development of disease [461] and the invasion of cancer into surrounding tissues [460].

Another aspect of cell behaviour that was neglected by *CellSim3D* is the stochastic nature of cell membrane interactions [284], recall that we

assumed that cell membranes do not undergo Brownian motion. We propose an augmentation to the *CellSim3D* model here to include a random term for Brownian motion, and combine it with cell polarity to model directed cell migration. This relies on the Dissipative Particle Dynamics method described in Section 2.2.2 and the intermembrane friction term defined in Section 5.2.2. We repeat their definitions here with the variable names and notation from Chapter 5 for clarity.

Let i be a node in cell m with polarity \mathbf{p}_m . Then the intermembrane friction force acting on i due to node i' at a distance $r_{ii'} = \|\mathbf{x}_i - \mathbf{x}_{i'}\|$ in some other cell n , can be set to

$$\mathbf{F}_i^{\text{F,e}} = \begin{cases} -\gamma_{\text{ext}}\omega^D(r_{ii'})\mathbf{v}_{ii'}^{\tau_m} & \text{if } r_{ii',n} < R_o^A \\ 0 & \text{if } r_{ii',n} > R_o^A, \end{cases} \quad (7.2)$$

where γ_{ext} is the intermembrane friction coefficient. The magnitude of γ_{ext} can be different depending on the cells that are interacting, however assume that it is the same between all cells, and $\mathbf{v}_{ii'}^{\tau_m}$ is the component of the relative velocity $\mathbf{v}_{i'} - \mathbf{v}_i$ tangential to the surface of m at \mathbf{x}_i . This equation is almost identical to Equation 5.8 in the current *CellSim3D* force field, with the addition of a new term $\omega^D(r_{ii'})$ which is a weight on the strength of intermembrane friction depending on the distance between i and i' . The random force would then be set to

$$\mathbf{F}^R(\mathbf{r}_{ij}) = \sigma\omega^R(r_{ij})\xi_{ij}\hat{\mathbf{r}}_{ij}, \quad (7.3)$$

where σ is the random force coefficient, ξ_{ij} is a random variable distributed normally with unit variance, and $\omega^R(r_{ij})$ is a weight on the random force strength. The intermembrane friction weight and this random term are related [159] by

$$\omega^D(r_{ij}) = [\omega^R(r_{ij})]^2 = 1. \quad (7.4)$$

Furthermore the random force and intermembrane friction coefficients would be related by

$$\sigma^2 = T_m\gamma_{\text{ext}}, \quad (7.5)$$

where T_m is a measure for the oscillations possible in the membrane for cell m . It is not related to the temperature of the system, rather it is a parameter that approximates how dynamic the membrane of cell m is.

Above, we have defined a formulation for the stochastic motion of cell membranes in the context of DPD. We can use the definition of the polarity vector $\hat{\mathbf{p}}_n$ to add an additional random force to the *CellSim3D* force field given by,

$$\mathbf{F}_{\text{mig}}^R = \begin{cases} \sigma_{\text{mig}} \zeta_{ij} \hat{\mathbf{r}}_i & \text{if } (\hat{\mathbf{r}}_i \cdot \hat{\mathbf{p}}) \geq 0 \\ 0 & \text{if } (\hat{\mathbf{r}}_i \cdot \hat{\mathbf{p}}) < 0 \end{cases} \quad (7.6)$$

where $\mathbf{r}_i = \mathbf{x}_i - \mathbf{x}_m$, x_m is the centre of mass of cell m , and σ_{mig} represents the strength of the migratory force, and ζ_{ij} is a uniformly distributed number between zero and one. This would result in a random migratory force that is parallel to the cell polarity.

Asymmetric Cell Division

Only symmetric random division is implemented in the current version of *CellSim3D*. In this regime, both new simulated cells are identical in every way to their parent cell. Asymmetric division is a kind of cell division in which the two daughters are not identical [462]. This form of cell division is vital in the differentiation of stem cells into different cells with different mechanical properties, structure, and biological function [213–215] (e.g. neurons versus liver cells).

Asymmetric division, from the perspective of the *CellSim3D* model, would result in child cells that are different from their siblings in several properties such as size, shape, mass, stiffness, and friction. Since each cell can be defined by a set of mechanical properties in *CellSim3D*, different cell types can be simulated by simply ascribing different values to the parameters for them. This was done for 2D systems with cells of different stiffness with the CeDEM method in Chapter 4, but without asymmetric division. The same can be done in 3D with the addition of a chance for either cell to be given different mechanical properties compared to the parent.

For example, consider differences in cell size. Difference in child cell size can be implemented by scaling the equilibrium bond lengths (R_{ij}^0 in Equation 5.2) between bonded nodes relative to the parent cell's equilibrium bond length. Consequently the child cells' volumes would be scaled

as well. The threshold division volume (V^{div}) for the child cells would have to be scaled as well.

References

1. Villareal, L. Are Viruses Alive? *Sci. Amer.* **291**, 100–105 (2004).
2. Forterre, P. Defining Life: The Virus Viewpoint. *Orig. Life. Evol. Biosph.* **40**, 151–160 (2010).
3. Elmore, S. Apoptosis: A Review of Programmed Cell Death. *Toxicol. Pathol.* **35**, 495–516 (2007).
4. Cheng, X. & Ferrell, J. E. Apoptosis Propagates through the Cytoplasm as Trigger Waves. *Science* **361**, 607–612 (2018).
5. Henson, P. M., Vandivier, R. W. & Douglas, I. S. Cell Death, Remodeling, and Repair in Chronic Obstructive Pulmonary Disease? *Proc. Am. Thorac. Soc.* **3**, 713–717 (2006).
6. Gest, H. The Discovery of Microorganisms by Robert Hooke and Antoni van Leeuwenhoek, Fellows of The Royal Society. *Notes and Records of the Royal Society of London* **58**, 187–201 (2004).
7. Singer, C. A History of Biology. (1950).
8. Cameron, D. E., Bashor, C. J. & Collins, J. J. A Brief History of Synthetic Biology. *Nat. Rev. Microbiol.* **12**, 381–390 (2014).
9. Frank, S. A. & Nowak, M. A. Cell Biology: Developmental Predisposition to Cancer. *Nature* **422**, 494 (2003).
10. Chen, Z., Li, S., Subramaniam, S., Shyy, J. Y.-J. & Chien, S. Epigenetic Regulation: A New Frontier for Biomedical Engineers. *Annu. Rev. Biomed. Eng.* **19**, 195–219 (2017).

11. Pollard, T. D., Earnshaw, W. C., Lippincott-Schwartz, J. & Johnson, G. T. *Cell Biology* (2008).
12. Voet, D., Voet, J. G. & W. Pratt, C. *Fundamentals of Biochemistry: Life at the Molecular Level* (Wiley, 2008).
13. Geudens, I. & Gerhardt, H. Coordinating Cell Behaviour during Blood Vessel Formation. *Development* **138**, 4569–4583 (2011).
14. Riento, K. & Ridley, A. J. ROCKs: Multifunctional Kinases in Cell Behaviour. *Nat. Rev. Mol. Cell Biol.* **4**, 446–456 (2003).
15. Frame, M. C. Src in Cancer: Deregulation and Consequences for Cell Behaviour. *Biochimica et Biophysica Acta (BBA) - Reviews on Cancer* **1602**, 114–130 (2002).
16. Brownlee, M. Biochemistry and Molecular Cell Biology of Diabetic Complications. *Nature* **414**, 813–820 (2001).
17. Kelly, D. P. Cell Biology: Ageing Theories Unified. *Nature* **470**, 342–343 (2011).
18. Rosowski, K. Introduction to Cell Mechanics and Mechanobiology. *Yale J. Biol. Med.* **86**, 436–437 (2013).
19. Boal, D. *Mechanics of the Cell* (Cambridge University Press, 2001).
20. Wang, N., Butler, J. & Ingber, D. Mechanotransduction across the Cell Surface and through the Cytoskeleton. *Science* **260**, 1124–1127 (1993).
21. Paluch, E. K. *et al.* Mechanotransduction: Use the Force(S). *BMC Biol.* **13** (2015).
22. Lauffenburger, D. A. & Horwitz, A. F. Cell Migration: A Physically Integrated Molecular Process. *Cell* **84**, 359–369 (1996).
23. Oakes, P. W. Balancing Forces in Migration. *Curr. Opin. Cell Biol.* **54**, 43–49 (2018).
24. Fung, Y. C. *Biomechanics: Mechanical Properties of Living Tissues* 2nd ed. (Springer-Verlag, New York, 1993).
25. Hill, M. A. & Meininger, G. A. in *Muscle* (eds Hill, J. A. & Olson, E. N.) 1243–1257 (Academic Press, Boston/Waltham, 2012).

26. Mattila, P. K. & Lappalainen, P. Filopodia: Molecular Architecture and Cellular Functions. *Nat. Rev. Mol. Cell Biol.* **9**, 446–454 (2008).
27. Gardel, M. L. *et al.* Traction Stress in Focal Adhesions Correlates Biphasically with Actin Retrograde Flow Speed. *J. Cell Biol.* **183**, 999–1005 (2008).
28. Lee, D. A., Knight, M. M., Campbell, J. J. & Bader, D. L. Stem Cell Mechanobiology. *J. Cell. Biochem.* **112**, 1–9 (2010).
29. Votteler, M., Kluger, P. J., Walles, H. & Schenke-Layland, K. Stem Cell Microenvironments - Unveiling the Secret of How Stem Cell Fate Is Defined. *Macromol. Biosci.* **10**, 1302–1315 (2010).
30. Murphy, W. L., McDevitt, T. C. & Engler, A. J. Materials as Stem Cell Regulators. *Nat. Mater.* **13**, 547–557 (2014).
31. Battista, S. *et al.* The Effect of Matrix Composition of 3D Constructs on Embryonic Stem Cell Differentiation. *Biomaterials* **26**, 6194–6207 (2005).
32. Farge, E. Mechanotransduction in Development. *Curr. Top. Dev. Biol.* **95**, 243–265 (2011).
33. Paszek, M. J. & Weaver, V. M. The Tension Mounts: Mechanics Meets Morphogenesis and Malignancy. *J. Mammary Gland Biol. Neoplasia* **9**, 325–342 (2004).
34. Salbreux, G., Charras, G. & Paluch, E. Actin Cortex Mechanics and Cellular Morphogenesis. *Trends Cell Biol.* **22**, 536–545 (2012).
35. Broders-Bondon, F., Ho-Boulloires, T. H. N., Fernandez-Sanchez, M.-E. & Farge, E. Mechanotransduction in Tumor Progression: The Dark Side of the Force. *J. Cell Biol.* **217**, 1571–1587 (2018).
36. Chin, L., Xia, Y., Discher, D. E. & Janmey, P. A. Mechanotransduction in Cancer. *Curr. Opin. Chem. Eng.* **11**, 77–84 (2016).
37. Wei, S. C. & Yang, J. Forcing through Tumor Metastasis: The Interplay between Tissue Rigidity and EpithelialMesenchymal Transition. *Trends Cell Biol.* **26**, 111–120 (2016).
38. Huang, H. Cell Mechanics and Mechanotransduction: Pathways, Probes, and Physiology. *AJP: Cell Physiology* **287**, C1–C11 (2004).

39. Cohen, N., Sarkar, S., Hondroulis, E., Sabhachandani, P. & Konry, T. Quantification of Intercellular Adhesion Forces Measured by Fluid Force Microscopy. *Talanta* **174**, 409–413 (2017).
40. Benoit, M. & Selhuber-Unkel, C. Measuring Cell Adhesion Forces: Theory and Principles. *Methods Mol. Biol.* **736**, 355–377 (2011).
41. Zheng, X. R. & Zhang, X. Microsystems for Cellular Force Measurement: A Review. *J. Micromech. Microeng.* **21**, 054003 (2011).
42. Madhikar, P., Åström, J., Westerholm, J. & Karttunen, M. CellSim3D: GPU Accelerated Software for Simulations of Cellular Growth and Division in Three Dimensions. *Comput. Phys. Commun.* **232**, 206–213 (2018).
43. Mkrtchyan, A., Åström, J. & Karttunen, M. A New Model for Cell Division and Migration with Spontaneous Topology Changes. *Soft Mat.* **10**, 4332–4339 (2014).
44. Alder, B. J. & Wainwright, T. E. Phase Transition for a Hard Sphere System. *J. Chem. Phys.* **27**, 1208–1209 (1957).
45. Alder, B. J. & Wainwright, T. E. Studies in Molecular Dynamics. I. General Method. *J. Chem. Phys.* **31**, 459–466 (1959).
46. Rahman, A. Correlations in the Motion of Atoms in Liquid Argon. *Phys. Rev.* **136**, A405–A411 (2A 1964).
47. Rahman, A. & Stillinger, F. H. Molecular Dynamics Study of Liquid Water. *J. Chem. Phys.* **55**, 3336 (1971).
48. Khalak, Y., Baumeier, B. & Karttunen, M. Improved General-Purpose Five-Point Model for Water: TIP5P/2018. *J. Chem. Phys.* **149**, 224507 (2018).
49. Vega, C. & Abascal, J. L. F. Simulating Water with Rigid Non-Polarizable Models: A General Perspective. *Phys. Chem. Chem. Phys.* **13**, 19663 (2011).
50. McCammon, J. A., Gelin, B. R. & Karplus, M. Dynamics of Folded Proteins. *Nature* **267**, 585 (1977).
51. Abraham, M. J. *et al.* GROMACS: High Performance Molecular Simulations through Multi-Level Parallelism from Laptops to Supercomputers. *SoftwareX* **1-2**, 19–25 (2015).

52. Acun, B. *et al.* Scalable Molecular Dynamics with NAMD on the Summit System. *IBM J. Res. Dev.* **62**, 4:1–4:9 (2018).
53. Plimpton, S. Fast Parallel Algorithms for Short-Range Molecular Dynamics. *J. Comput. Phys.* **117**, 1–19 (1995).
54. Phillips, J. C. *et al.* Scalable Molecular Dynamics with NAMD. *J. Comput. Chem.* **26**, 1781–1802 (2005).
55. Glaser, J. *et al.* Strong Scaling of General-Purpose Molecular Dynamics Simulations on GPUs. *Comput. Phys. Commun.* **192**, 97–107 (2015).
56. Freddolino, P. L., Arkhipov, A. S., Larson, S. B., McPherson, A. & Schulten, K. Molecular Dynamics Simulations of the Complete Satellite Tobacco Mosaic Virus. *Structure* **14**, 437–449 (2006).
57. Zhao, G. *et al.* Mature HIV-1 Capsid Structure by Cryo-Electron Microscopy and All-Atom Molecular Dynamics. *Nature* **497**, 643–646 (2013).
58. Sanbonmatsu, K. Y., Joseph, S. & Tung, C.-S. Simulating Movement of tRNA into the Ribosome during Decoding. *Proc. Natl. Acad. Sci. U.S.A.* **102**, 15854–15859 (2005).
59. Götz, A. W. *et al.* Routine Microsecond Molecular Dynamics Simulations with AMBER on GPUs. 1. Generalized Born. *J. Chem. Theory Comput.* **8**, 1542–1555 (2012).
60. Swope, W. C. & Andersen, H. C. $\hat{10}\{6\}$ -Particle Molecular-Dynamics Study of Homogeneous Nucleation of Crystals in a Supercooled Atomic Liquid. *Phys. Rev. B* **41**, 7042–7054 (1990).
61. Duan, Y. & Kollman, P. A. Pathways to a Protein Folding Intermediate Observed in a 1-Microsecond Simulation in Aqueous Solution. *Science* **282**, 740–744 (1998).
62. Yeh, I.-C. & Hummer, G. Peptide Loop-Closure Kinetics from Microsecond Molecular Dynamics Simulations in Explicit Solvent. *J. Am. Chem. Soc.* **124**, 6563–6568 (2002).
63. Klepeis, J. L., Lindorff-Larsen, K., Dror, R. O. & Shaw, D. E. Long-Timescale Molecular Dynamics Simulations of Protein Structure and Function. *Curr. Opin. Struct. Biol.* **19**, 120–127 (2009).

64. Schlick, T., Colleardo-Guevara, R., Halvorsen, L. A., Jung, S. & Xiao, X. Biomolecular Modeling and Simulation: A Field Coming of Age. *Q. Rev. Biophys.* **44**, 191–228 (2011).
65. Hospital, A., Goñi, J. R., Orozco, M. & Gelpí, J. L. Molecular Dynamics Simulations: Advances and Applications. *Adv Appl Bioinform Chem* **8**, 37–47 (2015).
66. Tieleman, D. P., Marrink, S. J. & Berendsen, H. J. A Computer Perspective of Membranes: Molecular Dynamics Studies of Lipid Bilayer Systems. *Biochim. Biophys. Acta* **1331**, 235–270 (1997).
67. Patra, M. *et al.* Molecular Dynamics Simulations of Lipid Bilayers: Major Artifacts Due to Truncating Electrostatic Interactions. *Bioophys. J.* **84**, 3636–3645 (2003).
68. Marrink, S. J. *et al.* Computational Modeling of Realistic Cell Membranes. *Chem. Rev.* (2019).
69. Marrink, S. J., Risselada, H. J., Yefimov, S., Tieleman, D. P. & de Vries, A. H. The MARTINI Force Field: Coarse Grained Model for Biomolecular Simulations. *J. Phys. Chem. B* **111**, 7812–7824 (2007).
70. MacKerell, A. D. *et al.* All-Atom Empirical Potential for Molecular Modeling and Dynamics Studies of Proteins. *J. Phys. Chem. B* **102**, 3586–3616 (1998).
71. Bernardi, R. C., Melo, M. C. & Schulten, K. Enhanced Sampling Techniques in Molecular Dynamics Simulations of Biological Systems. *Biochim. Biophys. Acta, Gen. Subj.* **1850**, 872–877 (2015).
72. Adcock, S. A. & McCammon, J. A. Molecular Dynamics: Survey of Methods for Simulating the Activity of Proteins. *Chem. Rev.* **106**, 1589–1615 (2006).
73. Pérez, A., Luque, F. J. & Orozco, M. Frontiers in Molecular Dynamics Simulations of DNA. *Acc. Chem. Res.* **45**, 196–205 (2012).
74. Cino, E. A., Wong-ekkabut, J., Karttunen, M. & Choy, W.-Y. Microsecond Molecular Dynamics Simulations of Intrinsically Disordered Proteins Involved in the Oxidative Stress Response. *PLoS One* **6**, e27371 (2011).

75. Gartner, T. E. & Jayaraman, A. Modeling and Simulations of Polymers: A Roadmap. *Macromolecules* **52**, 755–786 (2019).
76. Barrat, J.-L., Baschnagel, J. & Lyulin, A. Molecular Dynamics Simulations of Glassy Polymers. *Soft Matter* **6**, 3430–3446 (2010).
77. Bochicchio, D., Salvalaglio, M. & Pavan, G. M. Into the Dynamics of a Supramolecular Polymer at Submolecular Resolution. *Nat. Commun.* **8**, 147 (2017).
78. Bochicchio, D. & Pavan, G. M. Molecular Modelling of Supramolecular Polymers. *Advances in Physics: X* **3**, 1436408 (2018).
79. MacKerell, A. D. & Banavali, N. K. All-Atom Empirical Force Field for Nucleic Acids: II. Application to Molecular Dynamics Simulations of DNA and RNA in Solution. *J. Comput. Chem.* **21**, 105–120 (2000).
80. Cheatham III, T. E. & Kollman, P. A. Molecular Dynamics Simulation of Nucleic Acids. *Annu. Rev. Phys. Chem.* **51**, 435–471 (2000).
81. Parrinello, M. Polymorphic Transitions in Single Crystals: A New Molecular Dynamics Method. *J. Appl. Phys.* **52**, 7182 (1981).
82. Parrinello, M. & Rahman, A. Crystal Structure and Pair Potentials: A Molecular-Dynamics Study. *Phys. Rev. Lett.* **45**, 1196–1199 (1980).
83. Janowski, P. A. *Molecular Dynamics of Crystals* (Rutgers University - Graduate School - New Brunswick, 2015).
84. Wong-ekkabut, J. & Karttunen, M. The Good, the Bad and the User in Soft Matter Simulations. *Biochimica et Biophysica Acta (BBA) - Biomembranes* (2016).
85. Brini, E. *et al.* Systematic Coarse-Graining Methods for Soft Matter Simulations a Review. *Soft Matter* **9**, 2108 (2013).
86. Allen, M. P. & Tildesley, D. J. *Computer Simulation of Liquids (Oxford Science Publications)* (Clarendon Press, 1989).
87. Frenkel, D. & Smit, B. *Understanding Molecular Simulation: From Algorithms to Applications (Computational Science Series, Vol 1)* (Academic Press, 2001).
88. Rapaport, D. C. *The Art of Molecular Dynamics Simulation by D. C. Rapaport*

89. Schlacken, H. Molecular-Dynamics Simulation of Statistical-Mechanical Systems. *Acta Polym.* **39**, 151–152 (1988).
90. Hollingsworth, S. A. & Dror, R. O. Molecular Dynamics Simulation for All. *Neuron* **99**, 1129–1143 (2018).
91. Karplus, M. & Lavery, R. Significance of Molecular Dynamics Simulations for Life Sciences. *Isr. J. Chem.* **54**, 1042–1051 (2014).
92. Born, M. & Oppenheimer, R. Zur Quantentheorie Der Molekeln. *Ann. Phys.* **389**, 457–484 (1927).
93. Sutcliffe, B. T. & Woolley, R. G. On the Quantum Theory of Molecules. *J. Chem. Phys.* **137**, 22A544 (2012).
94. Feller, S. E., Yin, D., Pastor, R. W. & MacKerell, A. D. Molecular Dynamics Simulation of Unsaturated Lipid Bilayers at Low Hydration: Parameterization and Comparison with Diffraction Studies. *Biophys. J.* **73**, 2269–2279 (1997).
95. Feller, S. E. & MacKerell, A. D. An Improved Empirical Potential Energy Function for Molecular Simulations of Phospholipids. *J. Phys. Chem. B* **104**, 7510–7515 (2000).
96. Cornell, W. D. *et al.* A Second Generation Force Field for the Simulation of Proteins, Nucleic Acids, and Organic Molecules. *J. Am. Chem. Soc.* **117**, 5179–5197 (1995).
97. Dickson, C. J. *et al.* Lipid14: The Amber Lipid Force Field. *J. Chem. Theory Comput.* **10**, 865–879 (2014).
98. Oostenbrink, C., Villa, A., Mark, A. E. & Gunsteren, W. F. V. A Biomolecular Force Field Based on the Free Enthalpy of Hydration and Solvation: The GROMOS Force-Field Parameter Sets 53A5 and 53A6. *J. Comput. Chem.* **25**, 1656–1676 (2004).
99. Jorgensen, W. L. & Tirado-Rives, J. The OPLS [Optimized Potentials for Liquid Simulations] Potential Functions for Proteins, Energy Minimizations for Crystals of Cyclic Peptides and Crambin. *J. Am. Chem. Soc.* **110**, 1657–1666 (1988).

100. Jorgensen, W. L., Maxwell, D. S. & Tirado-Rives, J. Development and Testing of the OPLS All-Atom Force Field on Conformational Energetics and Properties of Organic Liquids. *J. Am. Chem. Soc.* **118**, 11225–11236 (1996).
101. Kristyán, S. & Pulay, P. Can (Semi)Local Density Functional Theory Account for the London Dispersion Forces? *Chem. Phys. Lett.* **229**, 175–180 (1994).
102. Reed, T. M. & Gubbins, K. E. *Applied Statistical Mechanics;: Thermodynamic and Transport Properties of Fluids (Chemical Engineering Series)* (McGraw-Hill, 1973).
103. Castro-Román, F., Benz, R. W., White, S. H. & Tobias, D. J. Investigation of Finite System-Size Effects in Molecular Dynamics Simulations of Lipid Bilayers. *J. Phys. Chem. B* **110**, 24157–24164 (2006).
104. Horbach, J., Kob, W., Binder, K. & Angell, C. A. Finite Size Effects in Simulations of Glass Dynamics. *Phys. Rev. E* **54**, R5897–R5900 (1996).
105. Salacuse, J. J., Denton, A. R. & Egelstaff, P. A. Finite-Size Effects in Molecular Dynamics Simulations: Static Structure Factor and Compressibility. I. Theoretical Method. *Phys. Rev. E* **53**, 2382–2389 (1996).
106. Darden, T., York, D. & Pedersen, L. Particle Mesh Ewald: An Nlog(N) Method for Ewald Sums in Large Systems. *The Journal of Chemical Physics* **98**, 10089 (1993).
107. Ewald, P. P. Die Berechnung Optischer Und Elektrostatischer Gitterpotentiale. *Ann. Phys. (Berl.)* **369**, 253–287 (1921).
108. Brown, W. M., Kohlmeyer, A., Plimpton, S. J. & Tharrington, A. N. Implementing Molecular Dynamics on Hybrid High Performance Computers—Particle-Particle-Particle-Mesh. *Comput. Phys. Commun.* **183**, 449–459 (2012).
109. De Leeuw, S., Perram, J., Smith, E. & Shipley, R. J. Simulation of Electrostatic Systems in Periodic Boundary Conditions. I. Lattice Sums and Dielectric Constants. *Proc. Royal Soc. Lond. A.* **373**, 27–56 (1980).

110. De Leeuw, S., Perram, J. & Smith, E. Simulation of Electrostatic Systems in Periodic Boundary Conditions. II. Equivalence of Boundary Conditions. *Proc. Royal Soc. Lond. A.* **373**, 57–66 (1980).
111. De Leeuw, S., Perram, J. & Smith, E. Simulation of Electrostatic Systems in Periodic Boundary Conditions. III. Further Theory and Applications. *Proc. Royal Soc. Lond. A.* **388**, 177–193 (1983).
112. Feng, K. & Qin, M. *Symplectic Geometric Algorithms for Hamiltonian Systems* (Springer, 2010).
113. Verlet, L. Computer “Experiments” on Classical Fluids. I. Thermodynamical Properties of Lennard-Jones Molecules. *Phys. Rev.* **159**, 98–103 (1967).
114. Hairer, E., Lubich, C. & Wanner, G. Geometric Numerical Integration Illustrated by the Störmer/Verlet Method. *Acta Numerica* **12**, 399–450 (2003).
115. Berendsen, H. & van Gunsteren, W. F. in *Molecular Dynamics Simulations of Statistical Mechanics Systems* 97, 43–65 (Amsterdam, 1986).
116. Tuckerman, M. E. *Statistical Mechanics: Theory and Molecular Simulation* 1 edition. 720 pp. (Oxford University Press, Oxford ; New York, 2010).
117. Noid, W. G. Perspective: Coarse-Grained Models for Biomolecular Systems. *J. Chem. Phys.* **139**, 090901 (2013).
118. Andersen, H. C. Molecular Dynamics Simulations at Constant Pressure and/or Temperature. *J. Chem. Phys.* **72**, 2384–2393 (1980).
119. Hoover, W. Canonical Dynamics: Equilibrium Phase-Space Distributions. *Phys. Rev. A: At., Mol., Opt. Phys.* **31**, 1695 (1985).
120. Nosé, S. A Molecular Dynamics Method for Simulations in the Canonical Ensemble. *Mol. Phys.* **52**, 255–268 (1984).
121. Nosé, S. A Unified Formulation of the Constant Temperature Molecular Dynamics Methods. *J. Chem. Phys.* **81**, 511–519 (1984).
122. Elder, R. M., Emrick, T. & Jayaraman, A. Understanding the Effect of Polylysine Architecture on DNA Binding Using Molecular Dynamics Simulations. *Biomacromolecules* **12**, 3870–3879 (2011).

123. Murtola, T., Bunker, A., Vattulainen, I., Deserno, M. & Karttunen, M. Multiscale Modeling of Emergent Materials: Biological and Soft Matter. *Phys. Chem. Chem. Phys.* **11**, 1869 (2009).
124. Onuchic, J. N. & Wolynes, P. G. Theory of Protein Folding. *Curr. Opin. Struct. Biol.* **14**, 70–75 (2004).
125. Fersht, A. R. From the First Protein Structures to Our Current Knowledge of Protein Folding: Delights and Scepticisms. *Nat. Rev. Mol. Cell Biol.* **9**, 650–654 (2008).
126. Cooper, G. M. The Eukaryotic Cell Cycle. *The Cell: A Molecular Approach.* 2nd edition (2000).
127. Margolin, W. & Bernander, R. How Do Prokaryotic Cells Cycle? *Curr. Biol.* **14**, R768–R770 (2004).
128. Wang, J. D. & Levin, P. A. Metabolism, Cell Growth and the Bacterial Cell Cycle. *Nat. Rev. Microbiol.* **7**, 822–827 (2009).
129. Merchant, B. A. & Madura, J. D. in *Annual Reports in Computational Chemistry* (ed Wheeler, R. A.) 67–87 (Elsevier, 2011).
130. Nielsen, S. O., Lopez, C. F., Srinivas, G. & Klein, M. L. Coarse Grain Models and the Computer Simulation of Soft Materials. *J. Phys.: Condens. Matter* **16**, R481–R512 (2004).
131. Marrink, S. J., de Vries, A. H. & Tieleman, D. P. Lipids on the Move: Simulations of Membrane Pores, Domains, Stalks and Curves. *Biochim. Biophys. Acta - Biomembranes* **1788**, 149–168 (2009).
132. Ingólfsson, H. I. et al. The Power of Coarse Graining in Biomolecular Simulations. *WIREs Comput. Mol. Sci.* **4**, 225–248 (2014).
133. Marrink, S. J. & Tieleman, D. P. Perspective on the Martini Model. *Chem. Soc. Rev.* **42**, 6801–6822 (2013).
134. Bradley, R. & Radhakrishnan, R. Coarse-Grained Models for Protein-Cell Membrane Interactions. *Polymers (Basel)* **5**, 890–936 (2013).
135. Monticelli, L. et al. The MARTINI Coarse-Grained Force Field: Extension to Proteins. *J. Chem. Theory Comput.* **4**, 819–834 (2008).
136. López, C. A. et al. Martini Coarse-Grained Force Field: Extension to Carbohydrates. *J. Chem. Theory Comput.* **5**, 3195–3210 (2009).

137. Yesylevskyy, S. O., Schäfer, L. V., Sengupta, D. & Marrink, S. J. Polarizable Water Model for the Coarse-Grained MARTINI Force Field. *PLoS Comput. Biol.* **6**, e1000810 (2010).
138. Ayton, G. S. & Voth, G. A. Multiscale Simulation of Transmembrane Proteins. *J. Struct. Biol.* **157**, 570–578 (2007).
139. Liew, C. C. & Mikami, M. A Coarse-Grained Model for Particle Dynamics Simulations of Complex Fluids. *Chem. Phys. Lett.* **368**, 346–351 (2003).
140. Peter, C., Site, L. D. & Kremer, K. Classical Simulations from the Atomistic to the Mesoscale and Back: Coarse Graining an Azobenzene Liquid Crystal. *Soft Matter* **4**, 859–869 (2008).
141. Provatas, N. & Elder, K. *Phase-Field Methods in Materials Science and Engineering* (Wiley, 2010).
142. Schmid, F. Toy Amphiphiles on the Computer: What Can We Learn from Generic Models? *Macromol. Rapid Commun.* **30**, 741–751 (2009).
143. Arnarez, C. *et al.* Dry Martini, a Coarse-Grained Force Field for Lipid Membrane Simulations with Implicit Solvent. *J. Chem. Theory Comput.* **11**, 260–275 (2015).
144. Schmidt, M. & Denton, A. R. Demixing of Colloid-Polymer Mixtures in Poor Solvents. *Phys. Rev. E* **65**, 061410 (2002).
145. Israelachvili, J. N., Mitchell, D. J. & Ninham, B. W. Theory of Self-Assembly of Lipid Bilayers and Vesicles. *Biochimica et Biophysica Acta (BBA) - Biomembranes* **470**, 185–201 (1977).
146. Brunsved, L., Folmer, B. J. B., Meijer, E. W. & Sijbesma, R. P. Supramolecular Polymers. *Chem. Rev.* **101**, 4071–4098 (2001).
147. Onufriev, A. in *Annual Reports in Computational Chemistry* (eds Wheeler, R. A. & Spellmeyer, D. C.) 125–137 (Elsevier, 2008).
148. Kleinjung, J. & Fraternali, F. Design and Application of Implicit Solvent Models in Biomolecular Simulations. *Curr. Opin. Struct. Biol.* **25**, 126–134 (2014).
149. Still, W. C., Tempczyk, A., Hawley, R. C. & Hendrickson, T. Semi-analytical Treatment of Solvation for Molecular Mechanics and Dynamics. *J. Am. Chem. Soc.* **112**, 6127–6129 (1990).

150. Tan, B. H. & Tam, K. C. Review on the Dynamics and Micro-Structure of pH-Responsive Nano-Colloidal Systems. *Adv. Colloid Interface Sci.* **136**, 25–44 (2008).
151. Mishra, B., Patel, B. B. & Tiwari, S. Colloidal Nanocarriers: A Review on Formulation Technology, Types and Applications toward Targeted Drug Delivery. *Nanomed. Nanotechnol. Biol. Med.* **6**, 9–24 (2010).
152. Janes, K. A., Calvo, P. & Alonso, M. J. Polysaccharide Colloidal Particles as Delivery Systems for Macromolecules. *Adv. Drug Delivery Rev.* **47**, 83–97 (2001).
153. Kubitschek, H. E. Growth During the Bacterial Cell Cycle: Analysis of Cell Size Distribution. *Biophys. J.* **9**, 792–809 (1969).
154. Groot, R. D. & Warren, P. B. Dissipative Particle Dynamics: Bridging the Gap between Atomistic and Mesoscopic Simulation. *J. Chem. Phys.* **107**, 4423–4435 (1997).
155. Hoogerbrugge, P. J. & Koelman, J. M. V. A. Simulating Microscopic Hydrodynamic Phenomena with Dissipative Particle Dynamics. *EPL* **19**, 155–160 (1992).
156. Koelman, J. M. V. A. & Hoogerbrugge, P. J. Dynamic Simulations of Hard-Sphere Suspensions Under Steady Shear. *EPL* **21**, 363–368 (1993).
157. Gonnella, G., Orlandini, E. & Yeomans, J. M. Spinodal Decomposition to a Lamellar Phase: Effects of Hydrodynamic Flow. *Phys. Rev. Lett.* **78**, 1695–1698 (1997).
158. Chen, S. & Doolen, G. D. Lattice Boltzmann Method for Fluid Flows. *Annu. Rev. Fluid Mech.* **30**, 329–364 (1998).
159. Español, P. & Warren, P. Statistical Mechanics of Dissipative Particle Dynamics. *EPL* **30**, 191–196 (1995).
160. Besold, G., Vattulainen, I., Karttunen, M. & Polson, J. Towards Better Integrators for Dissipative Particle Dynamics Simulations. *Phys. Rev. E* **62**, R7611–R7614 (2000).

161. Nikunen, P., Karttunen, M. & Vattulainen, I. How Would You Integrate the Equations of Motion in Dissipative Particle Dynamics Simulations? *Comput. Phys. Commun.* **153**, 407–423 (2003).
162. Alberts, B. *et al.* *Molecular Biology of the Cell (Sixth Edition)* (W. W. Norton & Company, 2014).
163. Hausman, G. M. C. & E., R. *Cell: A Molecular Approach, 7Th Edn* (Sinauer, 2016).
164. Sender, R., Fuchs, S. & Milo, R. Revised Estimates for the Number of Human and Bacteria Cells in the Body. *bioRxiv*, 036103 (2016).
165. Lombard, J. Once upon a Time the Cell Membranes: 175 Years of Cell Boundary Research. *Biology Direct* **9**, 32 (2014).
166. Goñi, F. M. The Basic Structure and Dynamics of Cell Membranes: An Update of the SingerNicolson Model. *Biochim. Biophys. Acta - Biomembranes* **1838**, 1467–1476 (2014).
167. Burton, N. M. & Bruce, L. J. Modelling the Structure of the Red Cell membrane. *Biochem. Cell Biol.* **89**, 200–215 (2011).
168. Vereb, G. *et al.* Dynamic, yet Structured: The Cell Membrane Three Decades after the Singer-Nicolson Model. *Proc. Natl. Acad. Sci. U.S.A.* **100**, 8053–8058 (2003).
169. Harayama, T. & Riezman, H. Understanding the Diversity of Membrane Lipid Composition. *Nat. Rev. Mol. Cell Biol.* **19**, 281–296 (2018).
170. Singer, S. J. & Nicolson, G. L. The Fluid Mosaic Model of the Structure of Cell Membranes. *Science* **175**, 720–731 (1972).
171. Zachowski, A. Phospholipids in Animal Eukaryotic Membranes: Transverse Asymmetry and Movement. *Biochem. J.* **294**, 1–14 (Pt 1 1993).
172. Gennis, R. B. *Biomembranes: Molecular Structure and Function* (ed Gennis, R. B.) (Springer-Verlag, New York, 1989).
173. Herrmann, H., Bär, H., Kreplak, L., Strelkov, S. V. & Aebi, U. Intermediate Filaments: From Cell Architecture to Nanomechanics. *Nat. Rev. Mol. Cell Biol.* **8**, 562–573 (2007).
174. Pollard, T. D., Earnshaw, W. C., Lippincott-Schwartz, J. & Johnson, G. *Cell Biology* OCLC: 969674619 (2017).

175. Murrell, M. P. & Gardel, M. L. F-Actin Buckling Coordinates Contractility and Severing in a Biomimetic Actomyosin Cortex. *Proc. Natl. Acad. Sci. U.S.A.* **109**, 20820–20825 (2012).
176. Wen, Q. & Janmey, P. A. Polymer Physics of the Cytoskeleton. *Curr. Opin. Solid State Mater. Sci.* **15**, 177–182 (2011).
177. Stricker, J., Falzone, T. & Gardel, M. L. Mechanics of the F-Actin Cytoskeleton. *J. Biomech.* **43**, 9–14 (2010).
178. Korn, E. D. Biochemistry of Actomyosin-Dependent Cell Motility (a Review). *Proc. Natl. Acad. Sci. U.S.A.* **75**, 588–599 (1978).
179. Dos Remedios, C. G. & Moens, P. D. J. Actin and the Actomyosin Interface: A Review. *Biochimica et Biophysica Acta (BBA) - Bioenergetics* **1228**, 99–124 (1995).
180. Marin-Riera, M., Brun-Usan, M., Zimm, R., Välikangas, T. & Salazar-Ciudad, I. Computational Modeling of Development by Epithelia, Mesenchyme and Their Interactions: A Unified Model. *Bioinformatics* **32**, 219–225 (2016).
181. Tanaka, S., Sichau, D. & Iber, D. LBIBCell: A Cell-Based Simulation Environment for Morphogenetic Problems. *Bioinformatics* **31**, 2340–2347 (2015).
182. Murray, P., Frampton, G. & Nelson, P. Cell Adhesion Molecules. *BMJ* **319**, 332–334 (1999).
183. Wozniak, M. A., Modzelewska, K., Kwong, L. & Keely, P. J. Focal Adhesion Regulation of Cell Behavior. *Biochim. Biophys. Acta* **1692**, 103–119 (2004).
184. Chugh, P. & Paluch, E. K. The Actin Cortex at a Glance. *J. Cell Sci.* **131**, jcs186254 (2018).
185. Buckley, C. D., Rainger, G. E., Bradfield, P. F., Nash, G. B. & Simmons, D. L. Cell Adhesion: More than Just Glue (Review). *Mol. Membr. Biol.* **15**, 167–176 (1998 Oct-Dec).
186. Gumbiner, B. M. Cell Adhesion: The Molecular Basis of Tissue Architecture and Morphogenesis. *Cell* **84**, 345–357 (1996).

187. Bezanilla, M., Gladfelter, A. S., Kovar, D. R. & Lee, W.-L. Cytoskeletal Dynamics: A View from the Membrane. *J. Cell Biol.* **209**, 329–337 (2015).
188. Rejniak, K. A. An Immersed Boundary Framework for Modelling the Growth of Individual Cells: An Application to the Early Tumour Development. *J. Theor. Biol.* **247**, 186–204 (2007).
189. Stewart, M. P. *et al.* Hydrostatic Pressure and the Actomyosin Cortex Drive Mitotic Cell Rounding. *Nature* **469**, 226–230 (2011).
190. Roubinet, C., Tran, P. T. & Piel, M. Common Mechanisms Regulating Cell Cortex Properties during Cell Division and Cell Migration. *Cytoskeleton* **69**, 957–972 (2012).
191. Strangeways, T. S. P. Observations on the Changes Seen in Living Cells during Growth and Division. *Proc. Roy. Soc. London* **94**, 137–141 (1922).
192. Cramer, L. P. & Mitchison, T. J. Investigation of the Mechanism of Retraction of the Cell Margin and Rearward Flow of Nodules during Mitotic Cell Rounding. *Mol. Biol. Cell* **8**, 109–119 (1997).
193. Kunda, P., Pelling, A. E., Liu, T. & Baum, B. Moesin Controls Cortical Rigidity, Cell Rounding, and Spindle Morphogenesis during Mitosis. *Curr. Biol.* **18**, 91–101 (2008).
194. Herrmann, H., Bär, H., Kreplak, L., Strelkov, S. V. & Aebi, U. Intermediate Filaments: From Cell Architecture to Nanomechanics. *Nat. Rev. Mol. Cell Biol.* **8**, 562–573 (2007).
195. Steinberg, G. & Fuchs, U. The Role of Microtubules in Cellular Organization and Endocytosis in the Plant Pathogen *Ustilago Maydis*. *J. Microsc.* **214**, 114–123 (Pt 2 2004).
196. Idilli, A. I. *et al.* Microtubule Depolymerization Affects Endocytosis and Exocytosis in the Tip and Influences Endosome Movement in Tobacco Pollen Tubes. *Molecular Plant* **6**, 1109–1130 (2013).
197. Oda, H. *et al.* Interaction of the Microtubule Cytoskeleton with Endocytic Vesicles and Cytoplasmic Dynein in Cultured Rat Hepatocytes. *J. Biol. Chem.* **270**, 15242–15249 (1995).

198. Fletcher, D. A. & Mullins, R. D. Cell Mechanics and the Cytoskeleton. *Nature* **463**, 485–492 (2010).
199. Nogales, E. Cytoskeleton in High Resolution. *Nat. Rev. Mol. Cell Biol.* **19**, 142 (2018).
200. Theocharis, A. D., Skandalis, S. S., Gialeli, C. & Karamanos, N. K. Extracellular Matrix Structure. *Adv. Drug Delivery Rev.* **97**, 4–27 (2016).
201. Humphrey, J. D., Dufresne, E. R. & Schwartz, M. A. Mechanotransduction and Extracellular Matrix Homeostasis. *Nat. Rev. Mol. Cell Biol.* **15**, 802–812 (2014).
202. Jahed, Z., Shams, H., Mehrbod, M. & Mofrad, M. R. K. Mechanotransduction Pathways Linking the Extracellular Matrix to the Nucleus. *Int. Rev. Cell Mol. Biol.* **310**, 171–220 (2014).
203. Jansen, K. A., Atherton, P. & Ballestrem, C. Mechanotransduction at the Cell-Matrix Interface. *Semin. Cell Dev. Biol.* **71**, 75–83 (2017).
204. Pickup, M. W., Mouw, J. K. & Weaver, V. M. The Extracellular Matrix Modulates the Hallmarks of Cancer. *EMBO Rep.* **15**, 1243–1253 (2014).
205. Ateshian, G. A., Morrison, B., Holmes, J. W. & Hung, C. T. Mechanics of Cell Growth. *Mech. Res. Commun.* **42**, 118–125 (2012).
206. Alberts, B. *et al.* *Molecular Biology of the Cell* 4th (Garland Science, 2002).
207. Blagosklonny, M. V. & Pardee, A. B. *The Restriction Point of the Cell Cycle* (Landes Bioscience, 2013).
208. Taber, L. A. Biomechanics of Growth, Remodeling, and Morphogenesis. *Appl. Mech. Rev.* **48**, 487–545 (1995).
209. Campbell, N. *Biology : Concepts & Connections* (Pearson/Benjamin Cummings, San Francisco, 2009).
210. Kleckner, N. Meiosis: How Could It Work? *Proc. Natl. Acad. Sci. U.S.A.* **93**, 8167–8174 (1996).
211. Angert, E. R. Alternatives to Binary Fission in Bacteria. *Nat. Rev. Microbiol.* **3**, 214–224 (2005).

212. Satterwhite, L. L. & Pollard, T. D. Cytokinesis. *Curr. Opin. Cell Biol.* **4**, 43–52 (1992).
213. Caussinus, E. & Gonzalez, C. Induction of Tumor Growth by Altered Stem-Cell Asymmetric Division in *Drosophila Melanogaster*. *Nat. Genet.* **37**, 1125–1129 (2005).
214. Chen, C., Fingerhut, J. M. & Yamashita, Y. M. The Ins(Ide) and Outs(Ide) of Asymmetric Stem Cell Division. *Curr. Opin. Cell Biol.* **43**, 1–6 (2016).
215. Morrison, S. J. & Kimble, J. Asymmetric and Symmetric Stem-Cell Divisions in Development and Cancer. *Nature* **441**, 1068–1074 (2006).
216. Rappaport, R. *Cytokinesis in Animal Cells* (Cambridge University Press, 1996).
217. Canman, J. C. *et al.* Determining the Position of the Cell Division Plane. *Nature* **424**, 1074–1078 (2003).
218. Pillitteri, L. J., Sloan, D. B., Bogenschutz, N. L. & Torii, K. U. Termination of Asymmetric Cell Division and Differentiation of Stomata. *Nature* **445**, 501–505 (2007).
219. Bosveld, F. *et al.* Epithelial Tricellular Junctions Act as Interphase Cell Shape Sensors to Orient Mitosis. *Nature* **530**, 495–498 (2016).
220. Sahlin, P. & Jönsson, H. A Modeling Study on How Cell Division Affects Properties of Epithelial Tissues Under Isotropic Growth. *PLoS One* **5**, e11750 (2010).
221. Falkenberg, M., Larsson, N.-G. & Gustafsson, C. M. DNA Replication and Transcription in Mammalian Mitochondria. *Annu. Rev. Biochem.* **76**, 679–699 (2007).
222. Porrua, O. & Libri, D. Transcription Termination and the Control of the Transcriptome: Why, Where and How to Stop. *Nat. Rev. Mol. Cell Biol.* **16**, 190–202 (2015).
223. Rejniak, K. A. & Anderson, A. R. A. Hybrid Models of Tumor Growth. *Wiley Interdiscip. Rev. Syst. Biol. Med.* **3**, 115–125 (2011).
224. Brodland, G. W. Computational Modeling of Cell Sorting, Tissue Engulfment, and Related Phenomena: A Review. *Appl. Mech. Rev.* **57**, 47–76 (2004).

225. Baltazar, D. A. & Friedman, A. *Models of Cellular Regulation* (Oxford University Press (OUP), 2008).
226. Sible, J. C. & Tyson, J. J. Mathematical Modeling as a Tool for Investigating Cell Cycle Control Networks. *Methods* **41**, 238–247 (2007).
227. Bellomo, N. & Carbonaro, B. Toward a Mathematical Theory of Living Systems Focusing on Developmental Biology and Evolution: A Review and Perspectives. *Phys. Life Rev.* **8**, 1–18 (2011).
228. Wattis, J. A. D. *et al.* Mathematical Model for Low Density Lipoprotein (LDL) Endocytosis by Hepatocytes. *Bull. Math. Biol.* **70**, 2303 (2008).
229. Britton, N. F. *Essential Mathematical Biology* (Springer, 2003).
230. Araujo, R. P. & McElwain, D. L. S. A History of the Study of Solid Tumour Growth: The Contribution of Mathematical Modelling. *Bull. Math. Biol.* **66**, 1039 (2004).
231. Gerber, G. B. & Léonard, A. Mutat. Res. *Mutation Research/Fundamental and Molecular Mechanisms of Mutagenesis* **12**, 175–182 (1971).
232. Schnute, J. A Versatile Growth Model with Statistically Stable Parameters. *Can. J. Fish. Aquat. Sci.* **38**, 1128–1140 (1981).
233. Litchfield, J. T. & Wilcoxon, F. A Simplified Method of Evaluating Dose-Effect Experiments. *J. Pharmacol. Exp. Ther.* **96**, 99–113 (1949).
234. Chou, T.-C. & Talalay, P. Quantitative Analysis of Dose-Effect Relationships: The Combined Effects of Multiple Drugs or Enzyme Inhibitors. *Adv. Enzyme Regul.* **22**, 27–55 (1984).
235. Aspridou, Z. & Koutsoumanis, K. P. Individual Cell Heterogeneity as Variability Source in Population Dynamics of Microbial Inactivation. *Food Microbiol.* **45**, 216–221 (2015).
236. Wartlick, O. *et al.* Dynamics of Dpp Signaling and Proliferation Control. *Science* **331**, 1154–1159 (2011).
237. Assanga, I. *et al.* Cell growth curves for different cell lines and their relationship with biological activities. *Int. J. Biotechnol. Mol. Biol. Res.* **4**, 60–70 (2013).

238. Brú, A. *et al.* Super-Rough Dynamics on Tumor Growth. *Phys. Rev. Lett.* **81**, 4008–4011 (1998).
239. Montague, P. R. & Friedlander, M. J. Expression of an Intrinsic Growth Strategy by Mammalian Retinal Neurons. *Proc. Natl. Acad. Sci. U.S.A.* **86**, 7223–7227 (1989).
240. Bryant, P. J. & Levinson, P. Intrinsic Growth Control in the Imaginal Primordia of *Drosophila*, and the Autonomous Action of a Lethal Mutation Causing Overgrowth. *Dev. Biol.* **107**, 355–363 (1985).
241. Kozusko, F. & Bourdeau, M. A Unified Model of Sigmoid Tumour Growth Based on Cell Proliferation and Quiescence. *Cell Prolif.* **40**, 824–834 (2007).
242. Zwietering, M. H., Jongenburger, I., Rombouts, F. M. & van 't Riet, K. Modeling of the Bacterial Growth Curve. *Appl. Environ. Microbiol.* **56**, 1875–1881 (1990).
243. Richards, F. J. A Flexible Growth Function for Empirical Use. *J. Exp. Bot.* **10**, 290–301 (1959).
244. Gompertz, B. On the Nature of the Function Expressive of the Law of Human Mortality, and on a New Mode of Determining the Value of Life Contingencies. *Philos. Trans. Roy. Soc. London*, 513–583 (1825).
245. Ranft, J. *et al.* Fluidization of Tissues by Cell Division and Apoptosis. *Proc. Natl. Acad. Sci. U.S.A.* **107**, 20863–20868 (2010).
246. N'Dri, N., Shyy, W. & Tran-Son-Tay, R. Computational Modeling of Cell Adhesion and Movement Using a Continuum-Kinetics Approach. *Biophys. J.* **85**, 2273–2286 (2003).
247. Schaller, G. & Meyer-Hermann, M. Multicellular Tumor Spheroid in an Off-Lattice Voronoi-Delaunay Cell Model. *Phys. Rev. E* **71**, 051910 (2005).
248. Murray, J. D. *Mathematical Biology: I. An Introduction: Pt. 1 (Interdisciplinary Applied Mathematics)* (Springer New York, 2008).
249. Bell, G., Dembo, M. & Bongrand, P. Cell Adhesion. Competition between Nonspecific Repulsion and Specific Bonding. *Biophys. J.* **45**, 1051–1064 (1984).

250. Ben Amar, M., Chatelain, C. & Ciarletta, P. Contour Instabilities in Early Tumor Growth Models. *Phys. Rev. Lett.* **106**, 148101 (2011).
251. Bittig, T., Wartlick, O., Kicheva, A., González-Gaitán, M. & Jülicher, F. Dynamics of Anisotropic Tissue Growth. *New J. Phys.* **10**, 063001 (2008).
252. Hategan, A., Law, R., Kahn, S. & Discher, D. E. Adhesively-Tensed Cell Membranes: Lysis Kinetics and Atomic Force Microscopy Probing. *Biophys. J.* **85**, 2746–2759 (2003).
253. Mahmoud, H. S., Pierre, S. & Farshid, M.-R. Regulation of the Membrane Wrapping Transition of a Cylindrical Target by Cytoskeleton Adhesion. *J. Royal Soc. Interface* **11**, 20140769 (2014).
254. Banerjee, S. & Marchetti, M. C. Continuum Models of Collective Cell Migration. *arXiv* (2018).
255. Palmieri, B., Bresler, Y., Wirtz, D. & Grant, M. Multiple Scale Model for Cell Migration in Monolayers: Elastic Mismatch between Cells Enhances Motility. *Sci. Rep.* **5**, 11745 (2015).
256. Van Roy, F. & Berx, G. The Cell-Cell Adhesion Molecule E-Cadherin. *Cell. Mol. Life Sci.* **65**, 3756–3788 (2008).
257. Stemmler, M. P. Cadherins in Development and Cancer. *Mol. Biosyst.* **4**, 835–850 (2008).
258. Parsons, J. T., Horwitz, A. R. & Schwartz, M. A. Cell Adhesion: Integrating Cytoskeletal Dynamics and Cellular Tension. *Nat. Rev. Mol. Cell Biol.* **11**, 633–643 (2010).
259. Szabó, A. & Merks, R. M. H. Cellular Potts Modeling of Tumor Growth, Tumor Invasion, and Tumor Evolution. *Front. Oncol.* **3**, 87 (2013).
260. Voss-Böhme, A. Multi-Scale Modeling in Morphogenesis: A Critical Analysis of the Cellular Potts Model. *PLoS One* **7** (ed Aegeerter, C. M.) e42852 (2012).
261. Graner, F. & Glazier, J. Simulation of Biological Cell Sorting Using a Two-Dimensional Extended Potts Model. *Phys. Rev. Lett.* **69**, 2013–2016 (1992).

262. Glazier, J. & Graner, F. Simulation of the Differential Adhesion Driven Rearrangement of Biological Cells. *Phys. Rev. E* **47**, 2128–2154 (1993).
263. Ising, E. Beitrag Zur Theorie Des Ferromagnetismus. *Zeitschrift für Physik A Hadrons and Nuclei* **31**, 253–258 (1925).
264. Wu, F. Y. The Potts Model. *Rev. Mod. Phys.* **54**, 235–268 (1982).
265. Kabla, A. J. Collective Cell Migration: Leadership, Invasion and Segregation. *J. Royal Soc. Interface* **9**, 3268–3278 (2012).
266. Chen, N., Glazier, J. A., Izaguirre, J. A. & Alber, M. S. A Parallel Implementation of the Cellular Potts Model for Simulation of Cell-Based Morphogenesis. *Comput. Phys. Commun.* **176**, 670–681 (2007).
267. Metropolis, N., Rosenbluth, A. W., Rosenbluth, M. N., Teller, A. H. & Teller, E. Equation of State Calculations by Fast Computing Machines. *J. Chem. Phys.* **21**, 1087–1092 (1953).
268. Käfer, J., Hayashi, T., Marée, A. F. M., Carthew, R. W. & Graner, F. Cell Adhesion and Cortex Contractility Determine Cell Patterning in the Drosophilaretina. *Proceedings of the National Academy of Sciences* **104**, 18549–18554 (2007).
269. Oates, A. C., Gorfinkiel, N., González-Gaitán, M. & Heisenberg, C.-P. Quantitative Approaches in Developmental Biology. *Nat. Rev. Genet.* **10**, 517–530 (2009).
270. Merks, R. M. H. & Glazier, J. A. A Cell-Centered Approach to Developmental Biology. *Physica A* **352**, 113–130 (2005).
271. Scianna, M., Preziosi, L. & Wolf, K. A Cellular Potts Model Simulating Cell Migration on and in Matrix Environments. *Math Biosci Eng* **10**, 235–261 (2013).
272. Shirinifard, A. *et al.* 3D Multi-Cell Simulation of Tumor Growth and Angiogenesis. *PLoS One* **4** (ed Hotchin, N. A.) e7190 (2009).
273. Chen, N., Glazier, J. A., Izaguirre, J. A. & Alber, M. S. A Parallel Implementation of the Cellular Potts Model for Simulation of Cell-Based Morphogenesis. *Comput. Phys. Commun.* **176**, 670–681 (2007).

274. Scianna, M. & Preziosi, L. Multiscale Developments of the Cellular Potts Model. *Multiscale Model. Simul.* **10**, 342–382 (2012).
275. Matela, R. J. & Fletterick, R. J. Computer Simulation of Cellular Self-Sorting: A Topological Exchange Model. *J. Theor. Biol.* **84**, 673–690 (1980).
276. Matela, R. J. & Fletterick, R. J. A Topological Exchange Model for Cell Self-Sorting. *J. Theor. Biol.* **76**, 403–414 (1979).
277. Duvdevani-Bar, S. & Segel, L. On Topological Simulations in Developmental Biology. *J. Theor. Biol.* **166**, 33–50 (1994).
278. Gibson, M. C., Patel, A. B., Nagpal, R. & Perrimon, N. The Emergence of Geometric Order in Proliferating Metazoan Epithelia. *Nature* **442**, 1038–1041 (2006).
279. Nagpal, R., Patel, A. & Gibson, M. C. Epithelial Topology. *Bioessays* **30**, 260–266 (2008).
280. Gibson, W. T. *et al.* On the Origins of the Mitotic Shift in Proliferating Cell Layers. *Theor. Biol. Med. Model.* **11**, 26 (2014).
281. Patel, A. B., Gibson, W. T., Gibson, M. C. & Nagpal, R. Modeling and Inferring Cleavage Patterns in Proliferating Epithelia. *PLoS Comput. Biol.* **5** (ed Axelrod, J.) e1000412 (2009).
282. Honda, H., Tanemura, M. & Nagai, T. A Three-Dimensional Vertex Dynamics Cell Model of Space-Filling Polyhedra Simulating Cell Behavior in a Cell Aggregate. *J. Theor. Biol.* **226**, 439–453 (2004).
283. Farhadifar, R., Röper, J.-C., Aigouy, B., Eaton, S. & Jülicher, F. The Influence of Cell Mechanics, Cell-Cell Interactions, and Proliferation on Epithelial Packing. *Curr. Biol.* **17**, 2095–2104 (2007).
284. Fletcher, A. G., Osterfield, M., Baker, R. E. & Shvartsman, S. Y. Vertex Models of Epithelial Morphogenesis. *Biophys. J.* **106**, 2291–2304 (2014).
285. Marder, M. Soap-Bubble Growth. *Phys. Rev. A* **36**, 438–440 (1987).
286. Okuzono, T. & Kawasaki, K. Intermittent Flow Behavior of Random Foams: A Computer Experiment on Foam Rheology. *Phys. Rev. E* **51**, 1246–1253 (1995).

287. Kawasaki, K., Nagai, T. & Nakashima, K. Vertex Models for Two-Dimensional Grain Growth. *Philos. Mag. B* **60**, 399–421 (1989).
288. Honda, H. & Eguchi, G. How Much Does the Cell Boundary Contract in a Monolayered Cell Sheet? *J. Theor. Biol.* **84**, 575–588 (1980).
289. Alt, S., Ganguly, P. & Salbreux, G. Vertex Models: From Cell Mechanics to Tissue Morphogenesis. *Philos. Trans. R. Soc. Lond. B. Biol. Sci.* **372** (2017).
290. Honda, H., Yamanaka, H. & Eguchi, G. Transformation of a Polygonal Cellular Pattern during Sexual Maturation of the Avian Oviduct Epithelium: Computer Simulation. *J. Embryol. Exp. Morphol.* **98**, 1–19 (1986).
291. Staple, D. B. *et al.* Mechanics and Remodelling of Cell Packings in Epithelia. *Eur Phys J E Soft Matter* **33**, 117–127 (2010).
292. Radszuweit, M., Block, M., Hengstler, J. G., Schöll, E. & Drasdo, D. Comparing the Growth Kinetics of Cell Populations in Two and Three Dimensions. *Phys. Rev. E Stat. Nonlin. Soft Matter Phys.* **79**, 051907 (5 Pt 1 2009).
293. Schaller, G. & Meyer-Hermann, M. Kinetic and Dynamic Delaunay Tetrahedralizations in Three Dimensions. *Comput. Phys. Commun.* **162**, 9–23 (2004).
294. Meyer-Hermann, M. Delaunay-Object-Dynamics: Cell Mechanics with a 3D Kinetic and Dynamic Weighted Delaunay-Triangulation. *Curr. Top. Dev. Biol.* 373–399 (2008).
295. Madhikar, P., Åström, J., Baumeier, B. & Karttunen, M. Morphology of Proliferating Epithelial Cellular Tissue. *arXiv* (2018).
296. Lee, D. T. & Schachter, B. J. Two Algorithms for Constructing a Delaunay Triangulation. *International Journal of Computer & Information Science* **9**, 219–242 (1980).
297. Paul Chew, L. Constrained Delaunay Triangulations. *Algorithmica* **4**, 97–108 (1989).
298. Edelsbrunner, H. & Shah, N. R. Incremental Topological Flipping Works for Regular Triangulations. *Algorithmica* **15**, 223–241 (1996).

299. Åström, J. A. & Karttunen, M. Cell Aggregation: Packing Soft Grains. *Phys. Rev. E* **73**, 062301 (2006).
300. Mkrtchyan, A. *A Single Cell Based Model for Cell Divisions with Spontaneous Topology Changes* (University of Western Ontario, 2013).
301. Paluch, E. & Heisenberg, C.-P. Biology and Physics of Cell Shape Changes in Development. *Curr. Biol.* **19**, R790–R799 (2009).
302. Li, Y., Naveed, H., Kachalo, S., Xu, L. X. & Liang, J. Mechanisms of Regulating Cell Topology in Proliferating Epithelia: Impact of Division Plane, Mechanical Forces, and Cell Memory. *PLoS One* **7** (ed Connolly, C. J.) e43108 (2012).
303. Heisenberg, C.-P. & Bellaïche, Y. Forces in Tissue Morphogenesis and Patterning. *Cell* **153**, 948–962 (2013).
304. Ragkousi, K. & Gibson, M. C. Cell Division and the Maintenance of Epithelial Order. *J. Cell Biol.* **207**, 181–188 (2014).
305. Sanchez-Gutierrez, D. *et al.* Fundamental Physical Cellular Constraints Drive Self-Organization of Tissues. *EMBO J.* **35**, 77–88 (2015).
306. Rauzi, M., Verant, P., Lecuit, T. & Lenne, P.-F. Nature and Anisotropy of Cortical Forces Orienting Drosophila Tissue Morphogenesis. *Nat. Cell Biol.* **10**, 1401–1410 (2008).
307. Tambe, D. T. *et al.* Collective Cell Guidance by Cooperative Intercellular Forces. *Nat. Mater.* **10**, 469–475 (2011).
308. Helmlinger, G., Netti, P. A., Lichtenbeld, H. C., Melder, R. J. & Jain, R. K. Solid Stress Inhibits the Growth of Multicellular Tumor Spheroids. *Nat. Biotechnol.* **15**, 778–783 (1997).
309. Kumar, S. & Weaver, V. M. Mechanics, Malignancy, and Metastasis: The Force Journey of a Tumor Cell. *Cancer Metastasis Rev.* **28**, 113–127 (2009).
310. Fötty, R. A., Pfleger, C. M., Forgacs, G. & Steinberg, M. S. Surface Tensions of Embryonic Tissues Predict Their Mutual Envelopment Behavior. *Development (Cambridge, England)* **122**, 1611–1620 (1996).
311. Lecuit, T. Adhesion Remodeling Underlying Tissue Morphogenesis. *Trends Cell Biol.* **15**, 34–42 (2005).

312. Guillot, C. & Lecuit, T. Mechanics of Epithelial Tissue Homeostasis and Morphogenesis. *Science* **340**, 1185–1189 (2013).
313. Liu, Z. *et al.* Mechanical Tugging Force Regulates the Size of Cell-Cell Junctions. *Proc. Natl. Acad. Sci. USA* **107**, 9944–9949 (2010).
314. Pontani, L.-L., Jorjadze, I., Viasnoff, V. & Brujic, J. Biomimetic Emulsions Reveal the Effect of Mechanical Forces on Cell-Cell Adhesion. *Proc. Natl. Acad. Sci. USA* **109**, 9839–9844 (2012).
315. Jones, G. W. & Chapman, S. J. Modeling Growth in Biological Materials. *SIAM Rev.* **54**, 52–118 (2012).
316. Gonzalez-Rodriguez, D., Guevorkian, K., Douezan, S. & Brochard-Wyart, F. Soft Matter Models of Developing Tissues and Tumors. *Science* **338**, 910–917 (2012).
317. Kursawe, J., Baker, R. E. & Fletcher, A. G. Approximate Bayesian Computation Reveals the Importance of Repeated Measurements for Parameterising Cell-Based Models of Growing Tissues. *J. Theor. Biol.* **443**, 66–81 (2018).
318. Fernández, L. A., Martín-Mayor, V. & Verrocchio, P. Phase Diagram of a Polydisperse Soft-Spheres Model for Liquids and Colloids. *Phys. Rev. Lett.* **98**, 085702 (2007).
319. Frenkel, D. & Wales, D. J. Designed to Yield. *Nat. Mater.* **10**, 410–411 (2011).
320. Charnley, M., Anderegg, F., Holtackers, R., Textor, M. & Meraldi, P. Effect of Cell Shape and Dimensionality on Spindle Orientation and Mitotic Timing. *PLoS One* **8** (ed Hotchin, N. A.) e66918 (2013).
321. Hernández-Hernández, V., Rueda, D., Caballero, L., Alvarez-Buylla, E. R. & Benítez, M. Mechanical Forces as Information: An Integrated Approach to Plant and Animal Development. *Front. Plant Sci.* **5**, 265 (2014).
322. Lesman, A., Notbohm, J., Tirrell, D. A. & Ravichandran, G. Contractile Forces Regulate Cell Division in Three-Dimensional Environments. *J. Cell. Biol.* **205**, 155–162 (2014).

323. Osterfield, M., Berg, C. A. & Shvartsman, S. Y. Epithelial Patterning, Morphogenesis, and Evolution: *Drosophila* Eggshell as a Model. *Dev. Cell* **41**, 337–348 (2017).
324. Owen, L. M. *et al.* A Cytoskeletal Clutch Mediates Cellular Force Transmission in a Soft, Three-Dimensional Extracellular Matrix. *Mol. Biol. Cell* **28** (ed Théry, M.) 1959–1974 (2017).
325. Gibson, W. T. & Gibson, M. C. in *Cur. Top. Dev. Biol.* 87–114 (Elsevier BV, 2009).
326. Sadati, M., Qazvini, N. T., Krishnan, R., Park, C. Y. & Fredberg, J. J. Collective Migration and Cell Jamming. *Differentiation* **86**, 121–125 (2013).
327. Reichhardt, C. & Olson Reichhardt, C. J. Active Matter Transport and Jamming on Disordered Landscapes. *Phys. Rev. E* **90**, 012701 (2014).
328. Alibert, C., Goud, B. & Manneville, J.-B. Are Cancer Cells Really Softer than Normal Cells? *Biol. Cell* **109**, 167–189 (2017).
329. Suresh, S. Biomechanics and Biophysics of Cancer Cells. *Acta Biomater.* **3**, 413–438 (2007).
330. Nguyen, A. V. *et al.* Stiffness of Pancreatic Cancer Cells Is Associated with Increased Invasive Potential. *Integr. Biol.* **8**, 1232–1245 (2016).
331. Luo, Q., Kuang, D., Zhang, B. & Song, G. Cell Stiffness Determined by Atomic Force Microscopy and Its Correlation with Cell Motility. *Biochim. Biophys. Acta - General Subjects* **1860**, 1953–1960 (2016).
332. Pilot, F. & Lecuit, T. Compartmentalized Morphogenesis in Epithelia: From Cell to Tissue Shape. *Dev. Dyn.* **232**, 685–694 (2005).
333. Herrero, A., Stavans, J. & Flores, E. The Multicellular Nature of Filamentous Heterocyst-Forming Cyanobacteria. *FEMS Microbiol. Rev.* **40** (ed Margolin, W.) 831–854 (2016).
334. Zhang, J.-Y., Lin, G.-M., Xing, W.-Y. & Zhang, C.-C. Diversity of Growth Patterns Probed in Live Cyanobacterial Cells Using a Fluorescent Analog of a Peptidoglycan Precursor. *Frontiers Microbiol.* **9**, 791 (2018).

335. Znachor, P. *Anabaena Planctonica* 2004.
336. Josef, J. & Braun, A. *Anabaena Laxa* 1991.
337. Kudela, R. *Anabaena Circinalis* 2018.
338. Demarteau, M. *Anabaena Flos-Aquae* 2011.
339. Sussman, D. M., Schwarz, J., Marchetti, M. C. & Manning, M. L. Soft yet Sharp Interfaces in a Vertex Model of Confluent Tissue. *Phys. Rev. Lett.* **120**, 058001 (2018).
340. Schaller, G. & Meyer-Hermann, M. Kinetic and Dynamic Delaunay Tetrahedralizations in Three Dimensions. *Comput. Phys. Commun.* **162**, 9–23 (2004).
341. Beyer, T. & Meyer-Hermann, M. Multiscale Modeling of Cell Mechanics and Tissue Organization. *IEEE Eng. Med. Biol. Mag.* **28**, 38–45 (2009).
342. Rejniak, K. A. & Anderson, A. R. A. A Computational Study of the Development of Epithelial Acini: I. Sufficient Conditions for the Formation of a Hollow Structure. *Bull. Math. Biol.* **70**, 677–712 (2008).
343. Nonomura, M. Study on Multicellular Systems Using a Phase Field Model. *PLoS One* **7** (ed Xu, Y.) e33501 (2012).
344. Angelini, T. E. *et al.* Cell Friction. *Faraday Disc.* **156**, 31 (2012).
345. Wang, Y., Lo, W.-C. & Chou, C.-S. A Modeling Study of Budding Yeast Colony Formation and Its Relationship to Budding Pattern and Aging. *PLoS Comput. Biol.* **13** (ed Komarova, N. L.) e1005843 (2017).
346. Flores, E., Herrero, A., Forchhammer, K. & Maldener, I. Septal Junctions in Filamentous Heterocyst-Forming Cyanobacteria. *Trends Microbiol.* **24**, 79–82 (2016).
347. Eisenhoffer, G. T. *et al.* Crowding Induces Live Cell Extrusion to Maintain Homeostatic Cell Numbers in Epithelia. *Nature* **484**, 546–549 (2012).
348. Erikson, M. J., Mueggenburg, N. W., Jaeger, H. M. & Nagel, S. R. Force Distributions in Three-Dimensional Compressible Granular Packs. *Phys. Rev. E* **66**, 2093707 (2002).

349. Jose, J., van Blaaderen, A. & Imhof, A. Random Three-Dimensional Jammed Packings of Elastic Shells Acting as Force Sensors. *Phys. Rev. E* **93**, 062901 (2016).
350. Van Eerd, A. R. T., Ellenbroek, W. G., van Hecke, M., Snoeijer, J. H. & Vlugt, T. J. H. Tail of the Contact Force Distribution in Static Granular Materials. *Phys. Rev. E* **75**, 060302 (2007).
351. Vinutha, H. A. & Sastry, S. Disentangling the Role of Structure and Friction in Shear Jamming. *Nat. Phys.* **12**, 578–583 (2016).
352. Nyberg, K. D. *et al.* Quantitative Deformability Cytometry: Rapid, Calibrated Measurements of Cell Mechanical Properties. *Biophys. J.* **113**, 1574–1584 (2017).
353. Sussman, D. M. cellGPU: Massively Parallel Simulations of Dynamic Vertex Models. *Comput. Phys. Commun.* **219**, 400–406 (2017).
354. Schaller, G. & Meyer-Hermann, M. Multicellular Tumor Spheroid in an Off-Lattice Voronoi-Delaunay Cell Model. *Phys. Rev. E* **71**, 051910 (2005).
355. Liedekerke, P. V. *et al.* Quantifying the Mechanics and Growth of Cells and Tissues in 3D Using High Resolution Computational Models. *bioRxiv*, 470559 (2018).
356. Liedekerke, P. V., Palm, M. M., Jagiella, N. & Drasdo, D. Simulating Tissue Mechanics with Agent-Based Models: Concepts, Perspectives and Some Novel Results. *Computational Particle Mechanics* **2**, 401–444 (2015).
357. Swat, M. H. *et al.* in *Methods in Cell Biology* 325–366 (Elsevier, Cambridge, MA, 2012).
358. Izaguirre, J. A. *et al.* COMPUCELL, a Multi-Model Framework for Simulation of Morphogenesis. *Bioinformatics* **20**, 1129–1137 (2004).
359. Hoehme, S. & Drasdo, D. A Cell-Based Simulation Software for Multi-Cellular Systems. *Bioinformatics* **26**, 2641–2642 (2010).
360. Pyshnov, M. B. Topological Solution for Cell Proliferation in Intestinal Crypt. I. Elastic Growth without Cell Loss. *J. Theor. Biol.* **87**, 189–200 (1980).

361. Stillinger, F. H. & Rahman, A. Improved Simulation of Liquid Water by Molecular Dynamics. *J. Chem. Phys.* **60**, 1545–1557 (1974).
362. Rahman, A. & Stillinger, F. H. Molecular Dynamics Study of Liquid Water. *J. Chem. Phys.* **55**, 3336–3359 (1971).
363. Rodriguez-López, T., Khalak, Y. & Karttunen, M. Non-Conformal Coarse-Grained Potentials for Water. *J. Chem. Phys.* **147**, 134108 (2017).
364. Karplus, M. & McCammon, J. A. Molecular Dynamics Simulations of Biomolecules. *Nature Structural & Molecular Biology* **9**, 646–652 (2002).
365. Sugita, Y. & Okamoto, Y. Replica-Exchange Molecular Dynamics Method for Protein Folding. *Chem. Phys. Lett.* **314**, 141–151 (1999).
366. Darré, L. *et al.* SIRAH: A Structurally Unbiased Coarse-Grained Force Field for Proteins with Aqueous Solvation and Long-Range Electrostatics. *J. Chem. Theory Comput.* **11**, 723–739 (2015).
367. Hornak, V. *et al.* Comparison of Multiple AMBER Force Fields and Development of Improved Protein Backbone Parameters. *Proteins* **65**, 712–725 (2006).
368. Anderson, J. A., Lorenz, C. D. & Travesset, A. General Purpose Molecular Dynamics Simulations Fully Implemented on Graphics Processing Units. *J. Comput. Phys.* **227**, 5342–5359 (2008).
369. Lam, R. H. W., Weng, S., Lu, W. & Fu, J. Live-Cell Subcellular Measurement of Cell Stiffness Using a Microengineered Stretchable Micropost Array Membrane. *Integr. Biol.* **4**, 1289–1298 (2012).
370. Shen, Y. *et al.* Single Cell Stiffness Measurement at Various Humidity Conditions by Nanomanipulation of a Nano-Needle. *Nanotechnology* **24**, 145703 (2013).
371. Stone, J. E. *et al.* Accelerating Molecular Modeling Applications with Graphics Processors. *J. Comput. Chem.* **28**, 2618–2640 (2007).
372. Rodrigues, C. I., Hardy, D. J., Stone, J. E., Schulten, K. & Hwu, W.-M. W. *GPU Acceleration of Cutoff Pair Potentials for Molecular Modeling Applications in Proceedings of the 5th Conference on Computing Frontiers* Ischia, Italy (ACM, New York, NY, USA, 2008), 273–282.

373. Galluzzi, L. *et al.* Molecular Mechanisms of Cell Death: Recommendations of the Nomenclature Committee on Cell Death 2018. *Cell Death & Differentiation* **25**, 486 (2018).
374. Tait, S. W. G., Ichim, G. & Green, D. R. Die Another Way Non-Apoptotic Mechanisms of Cell Death. *J. Cell Sci.* **127**, 2135–2144 (2014).
375. Lecuit, T. & Lenne, P.-F. Cell Surface Mechanics and the Control of Cell Shape, Tissue Patterns and Morphogenesis. *Nat. Rev. Mol. Cell Biol.* **8**, 633–644 (2007).
376. Kunda, P. & Baum, B. The Actin Cytoskeleton in Spindle Assembly and Positioning. *Trends Cell Biol.* **19**, 174–179 (2009).
377. Carreno, S. *et al.* Moesin and Its Activating Kinase Slik Are Required for Cortical Stability and Microtubule Organization in Mitotic Cells. *J. Cell Biol.* **180**, 739–746 (2008).
378. Edelman, G. M. Cell Adhesion Molecules. *Science* **219**, 450–457 (1983).
379. Fabri, A., Giezeman, G.-J., Kettner, L., Schirra, S. & Schönher, S. On the Design of CGAL a Computational Geometry Algorithms Library. *Software: Practice and Experience* **30**, 1167–1202 (2000).
380. Francis, A. H. An Atlas of Fullerenes By P. W. Fowler (University of Exeter), D. E. Manolopoulos (University of Nottingham). Oxford: New York. 1995. Viii + 392 Pp. 98.00. ISBN 0-19-855787-6. *J. Am. Chem. Soc.* **118**, 5161–5161 (1996).
381. Frederick, N. & Tomanek, D. *Carbon Fullerenes* <http://www.nanotube.msu.edu/fullerene/fullerene-isomers.html> (2019).
382. Murtola, T., Bunker, A., Vattulainen, I., Deserno, M. & Karttunen, M. Multiscale Modeling of Emergent Materials: Biological and Soft Matter. *Phys. Chem. Chem. Phys.* **11**, 1869–1892 (2009).
383. Cadart, C., Zlotek-Zlotkiewicz, E., Le Berre, M., Piel, M. & Matthews, H. K. Exploring the Function of Cell Shape and Size during Mitosis. *Dev. Cell* **29**, 159–169 (2014).
384. Wadell, H. Volume, Shape, and Roundness of Quartz Particles. *The Journal of Geology* **43**, 250–280 (1935).

385. Marieb, E. N. *Laboratory Manual for Anatomy & Physiology (5th Edition) (Anatomy and Physiology)* (Pearson, 2013).
386. Jones, H. W. Record of the First Physician to See Henrietta Lacks at the Johns Hopkins Hospital: History of the Beginning of the HeLa Cell Line. *Am. J. Obstet. Gynecol.* **176**, s227–s228 (1997).
387. Hospital, T. J. H. Surgical Biopsy Number 92498 (1951).
388. Zhao, L. *et al.* Intracellular Water-Specific MR of Microbead-Adherent Cells: The HeLa Cell Intracellular Water Exchange Lifetime. *NMR Biomed.* **21**, 159–164 (2008).
389. Milo, R., Jorgensen, P., Moran, U., Weber, G. & Springer, M. BioNumbers—the Database of Key Numbers in Molecular and Cell Biology. *Nucleic Acids Res.* **38**, D750–D753 (2009).
390. Park, K. *et al.* 'Living Cantilever Arrays' for Characterization of Mass of Single Live Cells in Fluids. *Lab. Chip* **8**, 1034–1041 (2008).
391. Laurent, V. M., Planus, E., Fodil, R. & Isabey, D. Mechanical Assessment by Magnetocytometry of the Cytosolic and Cortical Cytoskeletal Compartments in Adherent Epithelial Cells. *Biorheology* **40**, 235–240 (1,2,3 2003).
392. Foe, V. E. & Alberts, B. M. Studies of Nuclear and Cytoplasmic Behaviour during the Five Mitotic Cycles That Precede Gastrulation in *Drosophila* Embryogenesis. *J. Cell. Sci.* **61**, 31–70 (1983).
393. Cameron, I. L. & Greulich, R. C. Evidence for an Essentially Constant Duration of DNA Synthesis in Renewing Epithelia of the Adult Mouse. *J. Cell Biol.* **18**, 31–40 (1963).
394. Hahn, A. T., Jones, J. T. & Meyer, T. Quantitative Analysis of Cell Cycle Phase Durations and PC12 Differentiation Using Fluorescent Biosensors. *Cell Cycle* **8**, 1044–1052 (2009).
395. GNU General Public License, Version 2.
396. *CUDA Toolkit Documentation* () .
397. Lepilleur, B. *Jsoncpp - a C++ Library for Interacting with JSON* <https://github.com/open-source-parsers/jsoncpp>.
398. Group, T. H. *Hierarchical Data Format, Version 5* <http://www.hdfgroup.org/HDF5/>.

399. Van der Walt, S., Colbert, S. C. & Varoquaux, G. The NumPy Array: A Structure for Efficient Numerical Computation. *Comput. Sci. Eng.* **13**, 22–30 (2011).
400. Jones, E., Oliphant, T. & Peterson, P. SciPy: Open Source Scientific Tools for Python (2001–///).
401. Hunter, J. D. Matplotlib: A 2D Graphics Environment. *Computing In Science & Engineering* **9**, 90–95 (2007).
402. Da Costa-Luis, C. et al. *Tqdm/Tqdm: Tqdm v4.19.5 Stable* (2017).
403. McKinney, W. *Data Structures for Statistical Computing in Python* in *Proceedings of the 9th Python in Science Conference* (eds van der Walt, S. & Millman, J.) (2010), 51–56.
404. Guertin, D. A. & Sabatini, D. M. in *The Molecular Basis of Cancer* (eds Mendelsohn, J., Gray, J. W., Howley, P. M., Israel, M. A. & Thompson, C. B.) 179–190.e1 (Garland Science, Philadelphia, 2015).
405. Stephenson, F. H. in *Calculations for Molecular Biology and Biotechnology (Third Edition)* (ed Stephenson, F. H.) 43–79 (Academic Press, Boston, 2016).
406. Ricker, W. E. *Computation and Interpretation of Biological Statistics of Fish Populations (Bulletin of the Fisheries Research Board of Canada)* (The Blackburn Press, 1979).
407. Muehlbauer, P. A. & Schuler, M. J. Measuring the Mitotic Index in Chemically-Treated Human Lymphocyte Cultures by Flow Cytometry. *Mutat. Res.* **537**, 117–130 (2003).
408. Chung, K.-T., Nilson, E. H., Case, M. J., Marr, A. G. & Hungate, R. E. Estimation of Growth Rate from the Mitotic Index. *Appl. Microbiol.* **25**, 778–780 (1973).
409. Chung, K.-T., Nilson, E. H., Case, M. J. & Hungate, R. E. Estimation of Growth Rate from the Mitotic Index. *Appl. Microbiol.* **27**, 296 (1974).
410. Winick, M. Nutrition and Cell Growth. *Nutr. Rev.* **26**, 195–197 (1968).
411. Zetterberg, A. Control of Mammalian Cell Proliferation. *Curr. Opin. Cell Biol.* **2**, 296–300 (1990).

412. Jorgensen, P. & Tyers, M. How Cells Coordinate Growth and Division. *Curr. Biol.* **14**, R1014–R1027 (2004).
413. Keller, R. & Danilchik, M. Regional Expression, Pattern and Timing of Convergence and Extension during Gastrulation of *Xenopus Laevis*. *Development* **103**, 193–209 (1988).
414. Chuai, M. *et al.* Cell Movement during Chick Primitive Streak Formation. *Dev. Biol.* **296**, 137–149 (2006).
415. Butler, L. C. *et al.* Cell Shape Changes Indicate a Role for Extrinsic Tensile Forces in *Drosophila* Germ-Band Extension. *Nat. Cell Biol.* **11**, 859–864 (2009).
416. Janmey, P. A. & McCulloch, C. A. Cell Mechanics: Integrating Cell Responses to Mechanical Stimuli. *Annu. Rev. Biomed. Eng.* **9**, 1–34 (2007).
417. Saunders, M. M. Mechanical Testing for the Biomechanics Engineer: A Practical Guide. *Synthesis Lectures on Biomedical Engineering* **9**, 1–276 (2015).
418. Alert, R., Casademunt, J., Brugués, J. & Sens, P. Model for Probing Membrane-Cortex Adhesion by Micropipette Aspiration and Fluctuation Spectroscopy. *Biophys. J.* **108**, 1878–1886 (2015).
419. DiMilla, P. A., Barbee, K. & Lauffenburger, D. A. Mathematical Model for the Effects of Adhesion and Mechanics on Cell Migration Speed. *Biophys. J.* **60**, 15–37 (1991).
420. Brodland, G. W. & Veldhuis, J. H. A Computer Model for Reshaping of Cells in Epithelia Due to In-Plane Deformation and Annealing. *Comput. Methods Biomed. Engin.* **6**, 89–98 (2003).
421. Ziebert, F. & Aranson, I. S. Computational Approaches to Substrate-Based Cell Motility. *npj Comput. Mater.* **2**, 16019 (2016).
422. Rolfe, M. D. *et al.* Lag Phase Is a Distinct Growth Phase That Prepares Bacteria for Exponential Growth and Involves Transient Metal Accumulation. *J. Bacteriol.* **194**, 686–701 (2012).
423. Van Diest, P. J., van der Wall, E. & Baak, J. P. A. Prognostic Value of Proliferation in Invasive Breast Cancer: A Review. *J. Clin. Pathol.* **57**, 675–681 (2004).

424. Baak, J. P. A. *et al.* Proliferation Is the Strongest Prognosticator in Node-Negative Breast Cancer: Significance, Error Sources, Alternatives and Comparison with Molecular Prognostic Markers. *Breast Cancer Res. Treat.* **115**, 241–254 (2009).
425. Rudolph, P., Peters, J., Lorenz, D., Schmidt, D. & Parwaresch, R. Correlation between Mitotic and Ki-67 Labeling Indices in Paraffin-Embedded Carcinoma Specimens. *Hum. Pathol.* **29**, 1216–1222 (1998).
426. Jin, L., Murakami, T. H., Janjua, N. A. & Hori, Y. The Effects of Zinc Oxide and Diethyldithiocarbamate on the Mitotic Index of Epidermal Basal Cells of Mouse Skin. *Acta Med. Okayama* **48**, 231–236 (1994).
427. Thor, A. D., Liu, S., Moore II, D. H. & Edgerton, S. M. Comparison of Mitotic Index, In Vitro Bromodeoxyuridine Labeling, and MIB-1 Assays to Quantitate Proliferation in Breast Cancer. *JCO* **17**, 470–470 (1999).
428. Hoffman, J. G. Theory of the Mitotic Index and Its Application to Tissue Growth Measurement. *Bull. Math. Biophys.* **11**, 139–144 (1949).
429. Romar, G. A., Kupper, T. S. & Divito, S. J. Research Techniques Made Simple: Techniques to Assess Cell Proliferation. *J. Invest. Dermatol.* **136**, e1–e7 (2016).
430. Nakano, T. & Oka, K. Differential Values of Ki-67 Index and Mitotic Index of Proliferating Cell Population. An Assessment of Cell Cycle and Prognosis in Radiation Therapy for Cervical Cancer. *Cancer* **72**, 2401–2408 (1993).
431. Rojas, E. *et al.* Mitotic Index and Cell Proliferation Kinetics for Identification of Antineoplastic Activity. *Anticancer. Drugs* **4**, 637–640 (1993).
432. Brú, A., Albertos, S., Luis Subiza, J., García-Asenjo, J. L. & Brú, I. The Universal Dynamics of Tumor Growth. *Biophys. J.* **85**, 2948–2961 (2003).
433. Ponti, D. *et al.* Isolation and In Vitro Propagation of Tumorigenic Breast Cancer Cells with Stem/Progenitor Cell Properties. *Cancer Res.* **65**, 5506–5511 (2005).

434. Stoker, M. G. P. & Rubin, H. Density Dependent Inhibition of Cell Growth in Culture. *Nature* **215**, 171–172 (1967).
435. Lieberman, M. A. & Glaser, L. Density-Dependent Regulation of Cell Growth: An Example of a Cell-Cell Recognition Phenomenon. *J. Membrane Biol.* **63**, 1–11 (1981).
436. Holley, R. W. Control of Growth of Mammalian Cells in Cell Culture. *Nature* **258**, 487–490 (1975).
437. Westermark, B. Density Dependent Proliferation of Human Glia Cells Stimulated by Epidermal Growth Factor. *Biochem. Biophys. Res. Commun.* **69**, 304–310 (1976).
438. Noonan, K. D. & Burger, M. M. in *Progress in Surface and Membrane Science* (eds Cadenhead, D. A., Danielli, J. F. & Rosenberg, M. D.) 245–284 (Elsevier, 1974).
439. Brodland, G. & Veldhuis, J. H. Computer Simulations of Mitosis and Interdependencies between Mitosis Orientation, Cell Shape and Epithelia Reshaping. *J. Biomech.* **35**, 673–681 (2002).
440. Galle, J., Hoffmann, M. & Aust, G. From Single Cells to Tissue Architecturea Bottom-up Approach to Modelling the Spatio-Temporal Organisation of Complex Multi-Cellular Systems. *J. Math. Biol.* **58**, 261–283 (2009).
441. Sandersius, S. A., Chuai, M., Weijer, C. J. & Newman, T. J. Correlating Cell Behavior with Tissue Topology in Embryonic Epithelia. *PLoS One* **6**, e18081 (2011).
442. Gavara, N. & Chadwick, R. S. Relationship between Cell Stiffness and Stress Fiber Amount, Assessed by Simultaneous Atomic Force Microscopy and Live-Cell Fluorescence Imaging. *Biomech. Model. Mechanobiol.* **15**, 511–523 (2016).
443. Nogales, E. Structural Insights into Microtubule Function. *Annu. Rev. Biophys. Biomol. Struct.* **30**, 397–420 (2001).
444. Dmitrieff, S., Alsina, A., Mathur, A. & Nédélec, F. J. Balance of Microtubule Stiffness and Cortical Tension Determines the Size of Blood Cells with Marginal Band across Species. *Proc. Natl. Acad. Sci. U.S.A.* **114**, 4418–4423 (2017).

445. Gittes, F., Mickey, B., Nettleton, J. & Howard, J. Flexural Rigidity of Microtubules and Actin Filaments Measured from Thermal Fluctuations in Shape. *The Journal of Cell Biology* **120**, 923–934 (1993).
446. Nakajima, Y.-i., Meyer, E. J., Kroesen, A., McKinney, S. A. & Gibson, M. C. Epithelial Junctions Maintain Tissue Architecture by Directing Planar Spindle Orientation. *Nature* **500**, 359–362 (2013).
447. Redner, S. Random Multiplicative Processes: An Elementary Tutorial. *Am. J. Phys* **58**, 267–273 (1990).
448. Clusel, M., Corwin, E. I., Siemens, A. O. N. & Bruji, J. A ‘Granocentric’ Model for Random Packing of Jammed Emulsions. *Nature* **460**, 611–615 (2009).
449. Corwin, E. I., Clusel, M., Siemens, A. O. N. & Bruji, J. Model for Random Packing of Polydisperse Frictionless Spheres. *Soft Matter* **6**, 2949–2959 (2010).
450. Rohatgi, A. *WebPlotDigitizer* version 4.1. 2018.
451. Edelman, G. M. & Crossin, K. L. Cell Adhesion Molecules: Implications for a Molecular Histology. *Annu. Rev. Biochem.* **60**, 155–190 (1991).
452. Drubin, D. G. & Nelson, W. J. Origins of Cell Polarity. *Cell* **84**, 335–344 (1996).
453. Butler, M. T. & Wallingford, J. B. Planar Cell Polarity in Development and Disease. *Nat. Rev. Mol. Cell Biol.* **18**, 375–388 (2017).
454. Campanale, J. P., Sun, T. Y. & Montell, D. J. Development and Dynamics of Cell Polarity at a Glance. *J. Cell Sci.* **130**, 1201–1207 (2017).
455. Huttenlocher, A. Cell Polarization Mechanisms during Directed Cell Migration. *Nat. Cell Biol.* **7**, 336–337 (2005).
456. Elkouby, Y. M. & Mullins, M. C. Coordination of Cellular Differentiation, Polarity, Mitosis and Meiosis - New Findings from Early Vertebrate Oogenesis. *Dev. Biol.* **430**, 275–287 (2017).
457. Jan, Y.-N. & Jan, L. Y. Polarity in Cell Division: What Frames Thy Fearful Asymmetry? *Cell* **100**, 599–602 (2000).

458. Matsushita, K. Cell-Alignment Patterns in the Collective Migration of Cells with Polarized Adhesion. *Phys. Rev. E* **95**, 032415 (2017).
459. Ridley, A. J. *et al.* Cell Migration: Integrating Signals from Front to Back. *Science* **302**, 1704–1709 (2003).
460. Yamaguchi, H., Wyckoff, J. & Condeelis, J. Cell Migration in Tumors. *Curr. Opin. Cell Biol.* **17**, 559–564 (2005).
461. Franz, C. M., Jones, G. E. & Ridley, A. J. Cell Migration in Development and Disease. *Dev. Cell* **2**, 153–158 (2002).
462. Jan, Y. N. & Jan, L. Y. Assymetric Cell Division. *Nature* **392**, 775–778 (1998).

Appendices

Appendix A

Example Input file to *CellSim3D*

All input parameters are passed into the simulator via a configuration file that is formatted in JSON format. The parameters are divided into a number of categories:

- **"core"**

Defines the parameters given to *CellSim3D* simulator. The simulation cannot run without these values defined. They are given non-physical initial values. A sample is given in Listing 1.

- **"counting"**

Defines parameters related to counting the number of new cells born during a simulation. See the sample in Listing 2.

- **"divParams"**

Parameters for the plane perpendicular to which cells will divide. Used in most cases to set up epithelial simulations. See the sample in Listing 3.

- **"boxParams"**

Defines the box size. See sample in Listing 4

```
1 "core": {  
2     "MaxNoofC180s": 100000,  
3     "particle_mass": 0.04,  
4     "repulsion_range": 0.2,  
5     "attraction_range": 0.3,  
6     "repulsion_strength": 100.0,  
7     "attraction_strength": 0.5,  
8     "Youngs_mod": 1000,  
9     "viscotic_damping": 1,  
10    "internal_damping": 100.0,  
11    "gamma_visc": 1.0,  
12    "division_Vol": 2.0,  
13    "div_time_steps": 50000,  
14    "time_interval": 0.0001,  
15    "trajWriteInt": 1000,  
16    "non_div_time_steps": 50000,  
17    "trajFileName": "cellsim.cdv",  
18    "binaryOutput": 1,  
19    "maxPressure": 65.0,  
20    "minPressure": 50.0,  
21    "growth_rate": 0.002,  
22    "checkSphericity": 1,  
23    "constrainAngles": 1,  
24 }
```

Listing 1: The core parameters used in the simulation. These variables must be defined for simulations to run. They correspond to the constants in the CellSim3D force field.

```

1   "counting": {
2     "countCells": 0,
3     "mit-index_file_name": "inp.dat",
4     "count_only_internal_cells?": 0,
5     "radius_cutoff": 0.6,
6     "overwrite_mit_ind_file?": 0,
7     "cell_count_int": 1000
8   },

```

Listing 2: Counting parameters in CellSim3D. This file is only used for analysis.

```

1   "divParams": {
2     "useDivPlaneBasis": 0,
3     "divPlaneBasisX": 0,
4     "divPlaneBasisY": 0,
5     "divPlaneBasisZ": 1
6   },

```

Listing 3: Parameters setting the division plane of new cells. When "`divPlaneBasis`" is set to 1, the cells divide in the plane defined by the "`divPlaneBasisX`", "`divPlaneBasisY`", and "`divPlaneBasisZ`" values with are the components of the normal to the epithelial plane **E**; it is always normalized in the code.

```
1 "boxParams":{  
2     "useRigidSimulationBox": 1,  
3     "box_len_x": 500.0,  
4     "box_len_y": 500.0,  
5     "box_len_z": 500.0,  
6     "flatbox": 0,  
7     "dom_len": 1.5,  
8     "rand_pos": 0  
9 },
```

***Listing 4:** Properties of the simulation box CellSim3D simulations. All of the simulations conducted with this configuration of the simulation box.*

Summary

Molecular Dynamics Modelling of the Mechanics of Cells

All of life as we know it owes its success to the ability of cells to survive and thrive, in diverse and often intense circumstances. Biological functions in plants and animals are mediated by cells by growing, cooperating or competing with one another to keep the process of evolution alive. The key to unraveling the mysteries of life, finding cures for diseases, and discovering new life forms lies in investigating the behaviour of individual and collections of cells. We owe a significant debt to the work of the numerous biologists in the past few centuries who discovered and studied these remarkable organisms. For example, one of the most important developments arising from the study of cells is the field of modern medicine.

There are, however, important *aspects* of cell biology that we must not ignore. Namely, the physical nature of cells and how it may influence cell biology. Cells are physical objects with mass, density, and viscosity that passively interact with their surroundings (which could consist of other cells). Cells also actively interact with their surroundings by altering their physical properties and even exerting forces on their surroundings. Muscle cells are a simple example of this in action. A biological signal to muscle cells is translated into a physical signal (contraction). The converse can also occur. Physical forces acting on a cell can change its biological state as well, as was shown in stem cell differentiation. The interplay between the biological and the mechanical characteristics of cell behaviour is named mechanotransduction. This thesis focuses on exploring one part

of mechanotransduction: the connection between the physical properties of cells, their growth, and division.

Biologists have developed many powerful experimental tools to study cells, and they have used them with great success to teach us about microorganisms (the microscopic living entities that are cells). While quite powerful, experimental tools do have some shortcomings that can limit the amount of knowledge that can be gained from them. For example, while one can measure the forces generated in cell membranes of single cells, it is impossible to measure the forces between cells within tissues. Computational methods (simulators), such as the ones discussed in this thesis, are powerful tools to probe phenomena that are otherwise unreachable experimentally. Simulators also allow us to study *why* cells behave a certain way, and not just *how* they behave. Computational methods lie somewhere between experimental measurements and mathematical models of the underlying biophysics. Researchers can simulate cells in ways that obey the underlying biophysical laws known from theory, either known to be true or hypotheses, while producing systems *in silico* that can generate predictions that can be tested experimentally. This thesis is about the use of a such simulation methods to study cell growth and how it depends on tissue composition.

The methods that were used in this thesis are based on Molecular Dynamics (MD), a particle based modeling method typically used to study systems of interacting molecules. The basics of MD was described in Chapter 2. With some modifications MD can be “coarse-grained” to study much larger objects, such as cells. Before we do that, we explain the basic structure of cells in Chapter 3 named the *mechanical cell*. Properties of real cells, approximated by the mechanical cell, can then be translated into parameters to be used in different computational methods.

The Cellular Discrete Element Model (CeDEM), a two dimensional model that is based on cell structure and mechanical properties, was then used to study the formation of one dimensional tissues reminiscent of cyanobacteria and the growth of softer cells surrounded by stiff cells in Chapter 4. The research there led to two conclusions. Firstly, we can simulate the growth of tissues of various structures by simply selecting the orientation of cell division planes¹. Secondly, softer cells quickly over-

¹Cell division planes were explained in Section 3.3.1

whelm stiffer cells during growth in 2D systems such as epithelia². Since some types of cancer cells are softer than healthy cells, this result leads us to believe that their lower stiffness may be the reason for the faster growth of cancer cells. We also learned that the overwhelming of stiff (healthy) cells by soft (unhealthy) cells can be mitigated significantly by increasing the friction coefficient between the cell membranes. CeDEM is, however, a 2D model so it can only be used to study two dimensional systems such as epithelia.

The *CellSim3D* model, an extension of CeDeM into 3D, was introduced in Chapter 5. *CellSim3D* is a more general model that can be used to study epithelia and 3D tissues. A 3D model such as *CellSim3D* allows researchers to study a greater variety of cellular systems with more flexibility. The *CellSim3D* model is implemented into a high performance open source software package available GitHub at <https://github.com/SoftSimu/Cell-Sim3D>. The performance and simple usage instructions of the simulator were also discussed in Chapter 5. Hopefully the simulator will be a useful tool for computational biologists interested in studying tissue growth.

Finally, we studied the connection between cell growth and the local cellular environment with *CellSim3D* in Chapter 6. Biologists have long known that the growth rate of cells eventually slows down due a decreasing concentration of nutrients and the increased competition of cells for the nutrients that remain. We showed that this slowing of growth rate is inevitable, even in systems of cells given identical level of nutrients due to the evolving physical environment of each cell in growing tissues. Crowding and density play a crucial role how tissues grow. Some possible extensions to *CellSim3D* where proposed in Chapter 7, where we discussed how to model cell migration and differentiation.

²See Section 5.3.1

Acknowledgements

First of all, my most sincere gratitude to Dr. Mikko Karttunen, my promoter, without whom this work would not be possible. The *CellSim3D* project is the culmination of over a decade of research overseen by Mikko. Moving to the Netherlands with Mikko was one of the best decisions of my life. Mikko has also been incredibly helpful with his many comments and corrections when writing this thesis. Thank you Mikko for all your support.

I thank Dr. Björn Baumeier for his endless support throughout my PhD as my daily supervisor. No matter how busy he had been with his other students, Björn has always found the time to support me. Your keen eye for everything from topics of scientific inquiry, to multi-scale modelling, to aesthetic design, to proper language structure, to programming techniques, has been incredibly helpful for this thesis. Björn helped me a great deal in the writing of this thesis with his reviews and suggestions. Over the past four years we have developed a productive professional relationship and a good friendship as well. I am sure that I will be looking back at my time in Björn's group with great fondness and appreciate for what it has done for my career and education—in fact, I already do!

I thank Dr. Jan Westerholm (Åbo Akademi) for creating the original version of the *CellSim3D* simulator and from whose code I learned everything about GPU programming. The simulator that we published together (<https://github.com/SoftSimu/CellSim3D>) owes its existence to Jan's initial contribution. I also thank Jan for being on my committee. His time is greatly appreciated.

Thank you to Dr. Jan Åström (CSC — IT Center for Science) for his insights on simulations and analyses, and helping me to get up to speed

on the topic of simulating cells with molecular dynamics.

I would like to sincerely thank all the members of my committee for taking the time to review my thesis. I thank Dr. Siewart-Jan Marrink (Rijksuniversiteit Groningen), Dr. Gianluca Lattanzi (Università di Trento), and Dr. Jaap M.J den Toonder (TU/e) for their reading of my thesis and interest in my work.

Thank you to Dr. Giovanni Pavan (La Scuola universitaria professionale della Svizzera italiana) for opening my eyes to other forms of Coarse-Grained MD simulations and teaching me all I know about the simulations of supramolecular polymers and metadynamics. I also thank Dr. Davide Bochicchio, who has also been a great source of support guidance in my work. I will never forget the few months that I spent in the company Giovanni and Davide in Lugano. We did a lot of beautiful work in the beautiful city of Lugano.

This PhD would not have been possible without the support of Dr. Mark Peletier and Dr. Egbert Meijer. My sincerest thanks to them both for giving me the time to finish my work. I am especially grateful since the extra time allowed me to branch out and learn more about molecular dynamics. It also gave me the time to see to the publication of the *CellSim3D* simulator.

I would also like to express my gratitude for my group and office mates Jens, Onur, Gianluca, and Yuriy. They have taught me a great deal about physics and mathematics. They also helped with many helpful comments and suggestions when I was writing this thesis. I hope this group will continue to grow as it has with the addition of Wouter and Vivek, who have both been great company.

My time in the Netherlands has been made extremely enjoyable thanks to the huge number of friends that I have made during my time here. Although these friends did not directly contribute to this thesis, I must still acknowledge that spending time with them helped me decompress and rejuvenate. I really enjoyed travelling with my friends Koondi, Vishnu, Stephen, and Valliapan. We additionally had a great deal of parties with my friends Giovanni, Monica, Bart, Sai, Tarun, Mr. Bogers, Auke, Nikhil, Deepesh, Abhineet, Rien, Arthur, and many others whom I must have forgotten to name (my apologies!). I hope we all remain lifelong friends.

My four years at CASA have been stimulating, I thank all the members

of CASA for having me in their group. All of our work in CASA would come to a grinding halt were it not for the hard work and vigilance of our amazing secretaries Enna, Diane, Jolijn, and Marese. We would be lost without your deep understanding of the murky waters of university bureaucracy.

I learned a great deal about creativity and being more social from my Dungeons and Dragons group. I hope Martin, Mizar, Tilia, Lantesh, and our amazing dungeon master (you all know your actual names) continue their heroic adventures forevermore.

A great debt of gratitude is owed to Anwesha Bose, who came into my life and improved it every way. She has supported me with kindness, understanding, and love for a significant part of my PhD. Thank you, my love.

My family has always been an eternal source of wisdom and support. My parents, Dr. Prabhakar Madhikar and Rukmini Madhikar, are the giants one whose shoulders I stand. I owe everything I have become to their perseverance and sacrifice. My brother Prateek Madhikar is a great a source of wisdom and guidance, in spite of being younger. He has always used his astonishing intelligence and acute observational skills to be a good brother to me.

Pranav Madhikar
Eindhoven, May 2019

Curriculum Vitae

Pranav Madhikar was born in 1991 in the city of Hyderabad in India. One year later, his family moved to Cairo, Egypt. Pranav remained in Egypt for the next 16 years, and complete the I.G.C.S.E high school program. After that, Pranav went to the University of Waterloo in Ontario, Canada for his bachelor's degree in Nanotechnology Engineering which he completed in 2013. He obtained his master's degree in Chemistry at the same university in 2015. The next step in his adventure was to the Eindhoven University of Technology in the Netherlands in 2015, where he completed the work presented in this thesis.

List of Publications

- **Madhikar, P.**, Åström, J., Westerholm, J., Karttunen, M., CellSim3D: GPU Accelerated Software for Simulations of Cellular Growth and Division in Three Dimensions. *Comput. Phys. Commun.* **232**, 206–213 (2018).
- **Madhikar, P.**, Åström, J., Baumeier, B., Karttunen, M., Morphology of Proliferating Cellular Matter in One and Two Dimensions. *In preparation*.
- **Madhikar, P.**, Åström, J., Westerholm, J., Baumeier, B., Karttunen M., Influence of Density, Medium Viscosity, and Intermembrane Friction on Cell Growth and Nearest Neighbour Distribution. *In preparation*.
- Lafleur, R. P. M., Schoenmakers, S. M. C., **Madhikar, P.**, Bochicchio, D., Baumeier, B., Palmans, A. R. A, Pavan, G. M., Meijer, E. W., Insights into the Kinetics of Supramolecular Comonomer Incorporation in Water. *Macromolecules*. **52**, 3049–3055 (2019)
- Wehner, J., Brombacher, L., Brown, J., Junghans, C., Çaylak, O., Khalak, Y., **Madhikar, P.**, Tirimbò, G., Baumeier, B., Electronic Excitations in Complex Molecular Environments: Many-Body Greens Functions Theory in VOTCA-XTP. *J. Chem. Theory Comput.* **14**, 6253–6268 (2018).